Spatially Resolved Analysis of Flame Dynamics for the Prediction of Thermoacoustic Combustion Instabilities

Joseph A. Ranalli

Dissertation submitted to the faculty of the Virginia Polytechnic Institute and State University in partial fulfillment of the requirements for the degree of

Doctor of Philosophy
In
Mechanical Engineering

Uri Vandsburger
Walter F. O'Brien
Robert West
Christoph Hassa
Ken Smith
Joseph Schetz

April 28, 2009
Blacksburg, VA

Keywords: Combustion Instability, Thermoacoustics, Flame Transfer Functions, Chemiluminescence, Hotwire Anemometry,

Spatially Resolved Analysis of Flame Dynamics for the Prediction of Thermoacoustic Combustion Instabilities

Joseph A. Ranalli

Abstract

Increasingly stringent emissions regulations have led combustion system designers to look for more environmentally combustion strategies. For gas turbine combustion, one promising technology is lean premixed combustion, which results in lower flame temperatures and therefore the possibility of significantly reduced nitric oxide emissions. While lean premixed combustion offers reduced environmental impacts, it has been observed to experience increased possibility of the occurrence of combustion instabilities, which may damage hardware and reduce efficiency. Thermoacoustic combustion instabilities occur when oscillations in the combustor acoustics and oscillations in the flame heat release rate form a closed feedback loop, through one of two possible mechanisms. The first is direct coupling which occurs due to the mean mass flow oscillations induced by the acoustic velocity. Secondly, the acoustics may couple with the flame due to acoustic interactions with fuel/air mixing, resulting in an oscillating equivalence ratio. Only velocity coupling was considered in this study.

The methodology used in this study is analysis of instabilities through linear systems theory, requiring knowledge of the individual transfer functions making up the closed-loop system. Methods already exist by which combustor acoustics may be found. However, significant gaps still remain in knowledge of the nature of flame dynamics. Prior knowledge in literature about the flame transfer function suggests that the flame behaves as a low-pass filter, with cutoff frequency on the order of hundreds of hertz. Nondimensionalization of the frequency by flame length scales has been observed to result in a convenient scaling for the flame transfer function, suggesting that the flame dynamics may be dominated by spatial effects.

This work was proposed in two parts to extend and apply the body of knowledge on flame dynamics. The phase one goal of this study was to further understand this relationship between the flame heat release rate dynamics and the dynamics of the reaction zone size. The second goal of this work was to apply this flame transfer function knowledge to predictions of instability, validated against measurements in an unstable combustor. Both of these goals meet an existing practical need, providing a design tool for prediction of potential thermoacoustic instabilities in a combustor at the design stage.

Measurements of the flame transfer function were made in a swirl-stabilized, lean-premixed combustor. The novel portion of these measurements was the inclusion of spatial resolution of the heat release rate dynamics. By using a speaker, a sine dwell excitation to the velocity was introduced over the range of 10-400Hz. Measurements were then made of the input (inlet velocity) and output (heat release rate, or flame size) resulting in the flame transfer function. The spatial dynamics measurement was approached through several measures of the flame size: the volume and offset distance to the center of the heat release. Each was obtained from deconvoluted, phase averaged images of the flame, referenced to the speaker excitation signal. The results of these measurements showed that the spatial dynamics for each of these three measures were virtually identical to the heat release rate dynamics. This suggests a quite important result, namely that the flame heat release rate dynamics are completely determined by the dynamics of the flame structure. Therefore, prediction of flow structure interaction with the flame distribution is crucial to predict the dynamics of the flame.

These spatially resolved transfer function measurements were used in conjunction with the linear closed-loop model to make predictions of instability. These predictions were made by applying the Bode stability criterion to the open-loop system transfer function. This criterion states that instabilities may occur at frequencies where the heat release rate and acoustic oscillations occur in phase and the system gain has a value greater than unity. Performing this analysis on the combined system transfer function yielded results that agreed quite well with actual instability measurements made in the combustor. Closed-loop predictions identified two possible modes for instability, both of which were observed experimentally. One mode resulted from an acoustic peak around 160 Hz, and

occurred at lean equivalence ratios. A second mode occurred at lower frequencies (100-150 Hz) and was associated with the increase in flame transfer function gain at increasing equivalence ratios. These are some of the first successful predictions of combustion instability based on linear systems theory.

When multiple modes were predicted, it was assumed that if non-linear effects were to be considered, the lower frequency mode would become the dominant mode at these operating conditions due to its higher gain margin. Also of note is that in the practical system, high frequency oscillations are observed, but not predicted, associated with harmonics of the low frequency mode due to the linear nature of the predictions. While these non-linear effects are not captured, the linear predictive capability is thought to be most important, as from a practical perspective, instabilities should be avoided altogether.

The primary findings of this study have significant applications to modeling and prediction of combustion dynamics. The classic heat release rate flame transfer function was observed to coincide almost exactly with the flame size transfer functions. The time scales observed in these transfer functions correspond to convective length scales in the combustor, suggesting a fluid mechanical basis of the heat release rate response. Additionally, linear systems theory predictions of instability based on the measured flame transfer functions were proved capable of capturing the stability of the actual combustor with a reasonable degree of accuracy. These predictions should have considerable application to design level avoidance of combustion instability in practical systems.

Acknowledgements

I would like to acknowledge a variety of individuals with whom I have interacted throughout my graduate studies, and without whom the completion of my degree after all these years would never have been possible.

I would like to thank the Department of Defense for their financial support through the National Defense Science and Engineering Graduate Fellowship program.

I would like to thank the departmental staff in the Virginia Tech Department of Mechanical Engineering for their assistance with many questions and difficulties I encountered over the course of my academic career here at Virginia Tech.

I would like to thank all my professors and teachers through the years, for providing the guidance and support that I've needed to continue, even when the path was unclear. In all, twenty two years of formal education have brought me to this point and it's impossible to truly express my thanks to each of the individuals responsible for helping me along that journey.

I would like to thank by name Dr. William Baumann, Dr. Robert West, and Dr. Uri Vandsburger, the members past and present of the VACCG, who have worked hardest in assisting me through my graduate research. I was always treated as an equal and allowed to pursue my own ideas and my own methods as a part of this research group, and I am very thankful for that unique opportunity.

I would like to thank Steve LePera for his patience with my many questions in the lab. Steve's assistance and advice have made a huge contribution to completing my work, and his willingness to share his experience saved me many hours of frustration.

I would likewise like to thank the other graduate students who were a part of the VACCG during my time here. Their willingness to struggle with the difficulties of laboratory research alongside me helped me maintain my determination even against the most obstinate problems. In particular, I would like to thank Chris Martin for years of fruitful collaboration, and whose expertise was an invaluable complement to my own.

I would like to thank the several undergraduate research assistants who worked on my project through the years. They were a constant reminder to me what hard work looks like, and I have nothing but appreciation for their contributions to my research.

I would like to thank my parents, brother, family and friends for their constant support through the entirety of my education. I can't begin to explain the contribution made by their continued belief in my ability to make it through this.

Finally, I would like to thank my wife, Melissa, for her love, patience and understanding. My completion of this degree is a testament to her dedication, perseverance and support of me, even through the most difficult struggles I faced. Her motivation and encouragement kept me moving along this long road, and having reached its end, I am immeasurably thankful for it.

I will never be able to thank you all enough for your contributions to this work.

Joseph A. Ranalli

April 15, 2009

For Melissa

Table of Contents

List of Figures

Nomenclature

Symbol	Description	Units
Φ'	Fluctuating Equivalence Ratio	[-]
u’	Fluctuating Axial Velocity	[m/s]
q’	Fluctuating Flame Heat Release Rate	[kW]
R	Rayleigh Index	[-]
T	Period of Oscillation	[s]
p’	Fluctuating Pressure	[kPa]
t	Time	[s]
St	Strouhal Number	[-]
f	Frequency	[Hz]
x_o	Offset to Center of Heat Release Rate	[m]
$\bar{u}$	Mean Axial Velocity	[m/s]
τ_{res}	Reactor Residence Time	[s]
ρ	Density	[kg/m^3]
V	Reaction Region Volume	[m^3]
$\dot{m}$	Mass Flow Rate	[kg/s]
G	Flame Surface Field Variable	[-]
S_u	Laminar Flame Speed	[m/s]
S	Swirl Number	[-]

d_h	Hub Diameter of Swirler	[m]
d_o	Outer Diameter of Swirler	[m]
θ	Swirler Vane Angle	[rad]
p_{atm}	Atmospheric Pressure	[Pa]
u_m'	Fluctuating velocity at the hotwire measurement location	[m/s]
u_f'	Fluctuating velocity at the flame	[m/s]
$\left(A/F\right)_{s,m}$	Stoichiometric Air to Fuel Ratio by Mass	[kg-a/kg-f]
LHV	Lower Heating Value of the fuel	[kW]
P	Apparent, or projected, intensity in line-of-sight image	[-]
F	Actual cross-sectional intensity	[-]
r	Radial position relative to the centerline of the object	[m]
$\Im$	Flame Transfer Function	[-]
α	Acoustic Transfer Function	[-]
A	Combustor Cross Sectional Area	[m^2]
t_d	Time Delay	[s]
φ	Transfer Function Phase	[rad]

Chapter 1 - Introduction & Background

In recent years, increasing attention has been paid to the environmental impacts of various man-made systems. This attention has had significant impact on combustion driven devices. Awareness of environmental issues along with the desire to maintain efficiency and reliability has resulted in increased use of gas turbine based systems for power generation. As regulation on pollutants such as NO_x and carbon monoxide has become more stringent, interest has grown in operating gas turbines in a lean-premixed (LP) mode. This combustion design strategy allows more complete combustion to occur and features reduced flame temperatures. Both of these features result in an environmentally favorable impact on the overall turbine system.

Unfortunately, the advantages of LP combustion are not without a cost. Lean-premixed combustion has been observed to exhibit an increased susceptibility to thermoacoustic combustion instabilities. Thermoacoustic instabilities are the result of coupling between acoustic fluctuations and flame heat release rate fluctuations. These were first described by Rayleigh [41]. When oscillations in heat release rate are in phase with acoustic velocity fluctuations, these fluctuations are amplified. These velocity fluctuations can then cause oscillations in the upstream mass flow (u') and equivalence ratio (Φ'), through interactions with the mixing and delivery system. These induced oscillations then cause fluctuations in the flame heat release rate, closing the feedback loop. A system diagram of this phenomenon is shown schematically in Figure 1.1.

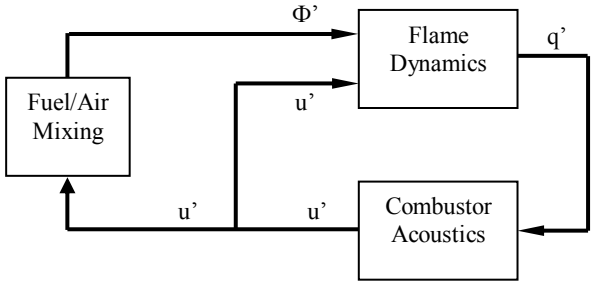

Figure 1.1 - Closed-loop system model of thermoacoustic instability.

The high amplitude acoustic oscillations can be detrimental to the combustion process in many ways. The high amplitude vibrations they induce can result in reduced efficiency

and damaged components. As such, much interest has been focused on characterizing, predicting and controlling these thermoacoustic instabilities. Through the research fueled by this interest, progress can me made toward overcoming thermoacoustic instabilities, allowing gas turbine engines to operate reliably in the most efficient and environmentally friendly ways possible.

Literature Review

To approach a problem with as much research background as that of thermoacoustic instability, it becomes necessary to have a good understanding of what work has already been done. This section will attempt to provide an overview of this extant knowledge. It will provide a clearer explanation of the thermoacoustic coupling mechanisms and then address the existing body of research.

1.1 Coupling Mechanisms

Thermoacoustic instabilities are the result of closed-loop coupling between the flame heat release rate and the system acoustics. The condition for amplification of this interaction was first stated by Rayleigh [5, 41] and forms the basis for the mathematical criterion which bears his name. Rayleigh's criterion is commonly used in the characterization of thermoacoustic instabilities and, simply put, states that when heat-release rate fluctuations are in phase with fluctuations in acoustic pressure, reinforcement of the oscillations occurs. This may be expressed mathematically as in Equation 1.

$$R = \int_0^T p'(t)q'(t)dt \tag{1}$$

When this quantity, termed the Rayleigh Index, is positive, amplification is indicated. When R has a negative value, damping of oscillations occurs.

While Rayleigh's criterion provides a metric for determining the stability of a system, eliminating instability requires a deeper knowledge of the underlying mechanisms. For this, we look further into the system diagram in Figure 1.1. This diagram shows two loops of feedback. First is the velocity loop which results in mass flow rate perturbations

to the flame. This loop is the result of coupling only with the acoustics and is present in all combustors. It has been observed through some introductory work by the author and collaborators that instabilities may be caused as a result of this coupling only [33]. The second loop involves interaction between acoustics and fuel/air mixing. In a practical combustion system, air and fuel flow rates can be drastically different (by a factor of 20:1 or more for the leanest cases). As such, fuel injection holes are typically much smaller than the air injection ports, and may commonly be choked. Thus the fuel and air injection ports may have significantly different acoustic characteristics and will respond differently when faced with perturbations in acoustic velocity [50]. This results in temporal variations in the air-to-fuel ratio introduced into the flow. These perturbations are convected downstream along with the bulk flow and may reach the flame depending on the physical characteristics of the flow train and mixing hardware. Placing the mixing apparatus sufficiently upstream of the flame can result in a system free of these equivalence ratio perturbations as they disperse before ever reaching the flame [15]. Though this can be useful for laboratory combustion experiments, it may not be achievable in practical systems due to hardware constraints. Both equivalence ratio and mass flow perturbations may be observed in actual instabilities [44]. Further, both have been reported to play an important role in instabilities in practice and in theory [27, 33].

1.2 Historical Development

Thermoacoustic flame interactions were first observed by Higgins in 1777 [49] and first described by Rayleigh in 1877 [5, 41]. Rayleigh notes that thermoacoustics were observed in Rijke's Tube, Chladni's Tube, Trevelyan's Rocker and the Glassblower's Tube; four phenomena that had been observed prior to that time. These relatively simple cases form the background for the more complex devices in which thermoacoustic coupling phenomena were later encountered. The field of thermoacoustic instabilities research really took off when it began to interfere with practical combustion devices. More specifically, during the development of liquid fueled chemical rockets in the 1950's, thermoacoustic instabilities were encountered due to the high energy release rates and confined combustion chambers present in such devices. These instabilities were the result of coupling of longitudinal acoustic modes with the flame, resulting in a low-

frequency oscillation referred to commonly as “POGO instability” or “chugging” [19, 47]. Instabilities in rockets were largely overcome through a “cut-and-try,” design-based approach resulting in a base of empirical design experience, which still guides the field of rocket development today.

Research on thermoacoustic instabilities again came to the forefront in gas turbine engines, particularly as increased emission restriction led to the use of lean-premixed combustion designs. The knowledge in this field in recent years can best be summarized by breaking it up into 3 categories of research.

- Experimental Characterization of the instabilities, aimed at providing insight into the coupling mechanisms and identifying the conditions under which instabilities are encountered.

- Theoretical Modeling aimed at mathematically describing the instabilities accurately to enhance understanding and predictive capabilities.

- Active and Passive Control of Instabilities aimed at eliminating instabilities from a combustion device in which they are present.

Each of these general topics will be addressed in further detail below.

1.3 Experimental Characterization

In general, one type of combustion instability research has the goal of experimentally determining behavior or characteristics of real instabilities. This broad goal may be broken down further into three subcategories, Coupling Mechanism Identification, Flame Frequency Response Function (FRF) Measurement and Stability Mapping. Seldom do actual studies fall into only a single area, but rather, these three goals underlie the areas of research pursued and form a framework within which to discuss the prior research. Each of these three goals has received significant research attention.

1.3.1 Diagnostics

In order to discuss work toward these experimental goals, a mention of some commonly encountered experimental parameters and measurement techniques is due. Measurements of flame heat-release rate, equivalence ratio, dynamic velocity and acoustic pressure are employed in many experimental studies of thermoacoustic instabilities [7]. These are all parameters closely related to the mechanisms which are thought to cause the coupling between the flame and the acoustics.

The fluctuating flame heat release rate, *q'* in Figure 1.1, is the response of the flame, which also serves as the acoustic source term. It is typically measured using chemiluminescence of the OH* radical or CH* radical [7, 22, 24, 26, 32], intermediate flame species which have been shown to be good indicators of the heat-release rate [17]. Chemiluminescence measurements of this type are based on light emission by this excited specie (at 308 nm for OH*, or 430nm for CH*), and generally speaking, employ some type of optical detector with an optical bandpass filter to isolate this wavelength. Measurements of heat-release rate may be made globally using an integrated measurement technique, or may attempt spatial resolution of the heat release rate. For example a filtered photomultiplier tube (PMT) may be used to measure the emitted intensity by the entire flame at 308 nm, resulting in a global measurement of the OH* chemiluminescence. Spatially resolved measurements of heat-release rate may be made using a multi-dimensional imaging technique, such as a filtered ICCD camera used to take two-dimensional images of the flame.

Fluctuating equivalence ratio, *Φ'*, appears in the outer loop of the closed-loop model in Figure 1.1. This quantity is only important when mixing oscillations are possible. Measurements of equivalence-ratio oscillations are typically made using light absorption [7, 26, 34]. In this technique, a laser beam aligned to an absorption line of the fuel specie is passed through the flow and the transmitted intensity is measured. This provides the concentration of that species in the flow, according to Beer's Law. For some hydrocarbon fuels, this can be done using a Helium-Neon laser at 3.39 μm. Other fuels, such as hydrogen, do not have a suitable absorption band for this type of measurements. In these cases, a tracer with a known concentration may be introduced into the fuel

stream. Spatial resolution of equivalence ratio is also possible with use of a planar laser induced fluorescence (PLIF) technique, generally using an acetone tracer. In this technique a laser sheet is passed through the flow train. This laser sheet is absorbed and reemitted by the target specie, allowing filtered, two-dimensional images of the reemitted radiation to be captured using a camera.

Acoustic velocity also appears in the closed-loop model as *u'* (see Figure 1.1). Velocity fluctuations are sometimes referred to interchangeably with mass flow fluctuations, due to the fact that when dealing with an incompressible fluid, they are analogous. Many techniques exist for making this measurement and include Laser Doppler Velocimetry (LDV), Particle Imaged Velocimetry (PIV) and hotwire anemometry [32, 44, 50], to name a few. LDV is a technique in which velocity is determined by measuring the time between reflections of a laser fringe pattern, generated by seeding particles passing through an interference pattern formed by two crossing laser beams. PIV describes a technique in which two images are taken in rapid succession and the movement of seed particles is tracked from image to image. LDV and PIV are advantageous in that they are optical measurements, not requiring intrusion on the flow. PIV has the added advantage of providing spatial resolution of the flow field. However, these techniques both require flow seeding which introduces additional design complication, and may lead to the optical surfaces becoming obstructed by the seed particles over time. A hotwire anemometer is a device in which a very fine, heated wire is inserted into the flow and velocity is obtained through measurement of the cooling caused by the flow over the hotwire. Hotwire anemometry, though requiring physical access to the flow, does not require seeding, so measurements can be made indefinitely.

Acoustic pressure, *p'*, does not appear directly in the closed-loop system model for combustion instability. This is because fluctuations in acoustic pressure have been shown not to result in a significant flame response relative to that due to velocity or equivalence ratio perturbations [33, 54]. It is still an important experimental quantity in that it is one of the most easily measured indicators of the magnitude of instability. This quantity is typically measured using pressure transducers (microphones). Depending on

the desired measurement location, microphones must be cooled to survive the high temperatures encountered in a combustion chamber.

1.3.2 Stability Mapping

The first important experimental goal mentioned above is to provide knowledge of the behavior of stability with respect to operating parameters. The author terms this "stability mapping." This is very useful to both modeling efforts and design in that it provides benchmarks to modelers and operating limits for practical systems to system designers. These types of measurements are usually limited to a fixed geometry, due to the geometry dependent nature of acoustics which play a major role in the dynamic stability of a system. However, the trends observed (i.e. increased incidence of instabilities with increased equivalence ratio) should be generally applicable, as acoustics are not strongly dependent on the operating condition.

Many different operating parameters have been tested with respect to stability limits by various groups of investigators. It has been widely observed that instabilities tend to tie in to the longitudinal acoustic modes in the combustor [4, 15, 45]. Instability frequencies showed some variation around these longitudinal mode frequencies, which has been attributed to the non-linear effects associated with limit cycling. In addition to this fundamental peak at a longitudinal acoustic mode, harmonics are also frequently observed.

Instabilities were observed by some investigators as blowoff was approached [4, 35], while other investigators observed instability under lean conditions away from blowoff [15, 33, 45]. No explanation has been found as to why this apparent discrepancy occurs. It has been observed that increasing equivalence ratio [33, 45] and flow rate [33, 53] result in an increased propensity for instability. Though these trends in stable operating conditions reveal relatively contiguous stable and unstable regions, the dominant frequency mode of the instability may change [45].

The effects of other operating conditions on unstable operation have also been investigated. Increasing inlet velocity, increasing swirl number and increasing the degree of unmixedness were all observed to promote instability [53]. Additionally, it was shown

that when dealing with changes in atmospheric condition in the air, parameters that affect reaction rate, in this case temperature and humidity, were the most significant, with increasing reaction rate leading to a higher incidence of instabilities [21].

1.3.3 Measurements of Flame Transfer Functions

Obtaining measurements of the flame dynamics is a goal closely related to that of stability mapping. Measurements of the flame dynamics are usually made by introducing a known input to a non-self-excited flame in the form of velocity or equivalence ratio fluctuations and measuring the heat-release rate response. This results in a measurement of the flame frequency response function (FRF). The aim of these studies is twofold. Firstly, they aim to provide knowledge to modeling studies as a basis for comparison. The second goal is to enable predictions of stability from the FRF characteristics. This is the category into which most of the prior experimental work related to combustion instabilities at Virginia Tech falls.

Published studies have yielded a strongly supported observation that the flame FRF has a low-pass filter-like character with linear phase [22, 24, 32]. When dealing with low-pass filters, the low-frequency magnitude (gain), the cutoff frequency (bandwidth) and the phase behavior are the most important parameters. For a fixed combustor geometry, increases in gain and bandwidth should, according to systems theory, result in an increased propensity for instability. Increased gain has the effect of adding amplification in the closed-loop system. Extended bandwidth may allow higher frequency acoustic peaks to become unstable.

Since the gain, bandwidth and phase are the most important characteristics in determining the stability of the closed-loop system with respect to operating conditions, identifying the trends in these characteristics is an important goal. It has been reported that FRF low-frequency gain is determined by the mean energy content of the fuel/air mixture [22]. Work by Martin shows that the gain of the flame response may be predicted by a sensitivity analysis of well-stirred reactor models [33]. Martin's work showed that gain should increase significantly with increasing equivalence ratio and increase to a lesser extent with decreasing mass flow. Increasing gain with increased equivalence ratio

agrees with the stability mapping results, which suggest that a richer mixture can lead to instability. The observation that higher flow rate promotes instability must have a different root cause than increases in the overall gain.

In all observed cases, the cutoff frequency of the flame FRF was found to be on the order of hundreds of hertz [22, 24]. This fact is of primary importance in guiding flame dynamics modeling efforts, as it highlights the timescales of the dominant physics. The bandwidth has been observed to increase with increasing equivalence ratio [22] and swirl [24]. It has further been observed by Lohrmann and Buchner that bandwidth is constant with respect to the Strouhal number [32]. Strouhal number is a form of frequency which is nondimensionalized by a length scale and the mean velocity, as shown in Equation 2.

$$St = \frac{fx_o}{\bar{u}} \tag{2}$$

The length scale for the Strouhal number used by Lohrmann and Buchner is the distance from the stabilizer to the point of greatest heat release rate. This quantity was linearly related to the flame length by the same authors [32]. They went on to state that the position of the cutoff frequency is related to the formation of vortical structures, which interact with the flame. As with gain, the trend of increasing bandwidth with increased equivalence ratio agrees with stability map observations.

1.3.4 Instability Mechanisms

The third type of experimental study focuses on experimentally identifying the coupling mechanisms that result in closed-loop feedback. These types of studies commonly use some sort of phase-locked imaging to observe any coherent flame structures which may develop over a pressure cycle during instability. A variety of mechanisms have been observed including equivalence ratio oscillations [9, 25, 26, 28, 34, 50], flame-vortex interactions [10, 13, 15], flame-boundary interactions [9], and periodic local quenching-reignition or detachment-attachment of the flame [15, 53]. More than one mechanism may be at work in some cases.

Equivalence ratio oscillations and flame interaction with vortical structures are the two most commonly discussed instability mechanisms. The coupling mechanism responsible for equivalence ratio oscillations involves coupling between the acoustics and the fuel air mixing, as mentioned in Section 1.1. It is common in fuel injection designs for the supply systems to have different port sizes for the fuel and air injection, due to their significantly different flow rates.

Given such a configuration, a velocity perturbation due to acoustics will result in a different effect on the flow from the fuel and air ports [50]. This may result in a local fluctuation in the equivalence ratio, which may be convected downstream toward the flame. If the mixture oscillation has not diffused out due to the turbulence or mixing, the change in equivalence ratio alters the heat release rate of the flame, which in turn drives fluctuations in the combustor acoustics, closing the loop. The convective time has been observed to be the most important parameter in characterizing this coupling [27, 33]. As mentioned previously, careful experimental design can prevent these perturbations from reaching the flame [15], but in practical systems, design limitations make elimination of equivalence ratio oscillations difficult.

Flame-vortex interactions have been observed in many studies. They couple to the acoustics in the following manner. Fluctuations in velocity result in the shedding of a vortex at the dump plane [15]. This vortex interacts with the flame as it breaks down, resulting in a variation in the flame surface area and thus, fluctuations in the heat-release rate [10, 43]. These heat-release rate fluctuations close the loop by continuing to drive further oscillations in the acoustic velocity. The convection and breakdown of these vortices can be modeled using the time lag from the formation to the breakdown of a vortex [15]. These vortices have the most significant impact on the flame in the absence of swirl [53]. Since the vortices are a coherent flow structure, interfering with the formation of that structure may be a possible method for passive control. One study using this approach was able to extend stability limits by shortening the flame, by introducing a partial mixture of hydrogen, so that it did not reach the vortex breakdown zone [14].

1.4 Theoretical Models

While the goal of experimental work discussed previously is to characterize the instabilities observed in a real combustor, the goal of modeling studies is to apply experimental knowledge to develop predictive capability. The ability to predict the occurrence of instabilities is advantageous in that it allows a more rigorous design process to be applied. There are basically three types of modeling studies encountered with combustion instabilities. Numerical models use complete descriptions of the physics and chemistry to try and simulate the combustion process. Reduced-order models attempt to reduce the physics involved to a smaller set of equations that are still able to capture the significant behavior of the actual flame. Finally, system level models make use of other model types (typically reduced-order models) to make predictions of stable operating conditions using systems theory. These models rely on a closed-loop feedback model of the instability as shown above in Figure 1.1.

Numerical models will not be expounded upon here. The computational effort required to produce a numerical solution for the reacting flow in a combustor makes use of CFD-based models too bulky for predictions of stability using closed-loop models. Additionally, these models do not allow insight into physical mechanisms, but rather, just focus on creating results. Industry is in need of tools that can be used by design engineers without a major computational effort. As such, reduced-order models are preferable.

1.4.1 Reduced-Order Models

Many different types of reduced-order models have been used in trying to predict flame dynamics. These different models each have their own advantages and disadvantages. The appropriateness of a given model depends largely on the operating condition and system geometry [28]. Care must be taken to ensure that the physics reflected by the model are in fact the dominant physics of the actual combustion system.

Zero-Dimensional Turbulent Combustor - The Well-Stirred Reactor

A well-stirred reactor (WSR) is a type of reduced-order combustion model in which mixing is assumed to happen very fast relative to the chemistry. This results in a model

in which mixing in the reaction region is so quick that the flame region can be assumed to be completely uniform in all variables. This type of model results in a jump condition for the flame, that is, it is a zero-dimensional model in space. These models have long been used for steady prediction of blowoff and have been through to represent the physics of a strong recirculation zone, typical of dump combustors [33, 36, 37, 51]. Some recent work has suggested that the limitation of well-stirred reactors in which the volume is a parameter of the model, rather than a result, may prevent their widespread accuracy [28, 33].

Well-stirred reactors, like experimental data, have been observed to display low-pass filter behavior in flame transfer functions [27, 33, 36, 37]. These results, however, did not agree with the bandwidth observed in experiments. Rather bandwidth was observed to be caused by the chemical kinetics and occurred in the thousands of hertz. It was shown by Martin [33] that the underlying physics associated with WSR models reveal timescales corresponding to the bandwidth range observed in experiments. These timescales were observed to correspond to the steady residence time, a recurring parameter of well-stirred reactor models. This parameter is represented as the ratio of the mass of the flame to the inlet mass flow rate, as shown in Equation 3.

$$\tau_{res} = \frac{\rho V}{\dot{m}} \tag{3}$$

In order to analyze the time varying behavior of this parameter, it must be differentiated. Assuming incompressibility, this results in Equation 4.

$$\frac{\partial \tau_{res}}{\partial t} = \frac{\rho}{\dot{m}} \frac{\partial V}{\partial t} + \rho V \frac{\partial}{\partial t}\left(\frac{1}{\dot{m}}\right) \tag{4}$$

The derivative of mass flow rate is the input of the flame transfer function. The time derivative of volume remains unknown. It was shown by Martin [33] that the constraint applied to this residence time (i.e. V=constant, etc.) has a drastic effect on the placement of the dynamic zeroes of the system, altering the character of the FRF significantly. Thus, well-stirred reactor models, lacking a physical prediction of the time-resolved

volume, are unable to predict one of the crucial physical constraints governing the dynamics [28, 33]. Though WSR models do not appear to accurately predict the dynamics of the flame, it has been shown by Martin [33] that they may be analyzed in such a way as to provide predictions of the flame transfer function low frequency gain. Though careful analysis of WSR models may provide some insight into flame dynamics, the fundamental lack of spatial resolution has led to a desire to use models with a higher spatial dimension, allowing the crucial flame size parameter to be modeled.

Flame Sheet Models

While the dynamic well-stirred reactor has zero spatial dimensions, a flame sheet model is a one-dimensional model that may provide insight into the flame dynamics. A flame sheet model, as the name implies, treats the flame as a thin sheet with uniform-thickness. This sheet is free to wrinkle and flutter in response to flow oscillations [8, 11, 39, 40, 54]. Variations in heat release can then be related to the flame surface area. The equation for a flame sheet is derived by balancing the local flame propagation with the convective velocity, as shown in Equation 5 [39].

$$\frac{\partial G}{\partial t} = S_u \left|\nabla G\right| - \vec{u} \bullet \nabla G \tag{5}$$

Here S_u is the flame speed, u the velocity vector and G the variable defining the surface of the flame. Because of the dependence on flow field and velocity, solving this equation is a relatively simple proposition for laminar flow, but becomes significantly more complex with turbulence. Attempts to predict flame dynamics using these models have resulted in predictions that the bandwidth for both types of oscillation is constant with respect to Strouhal number [39, 54], using flame length as the characteristic size. This agrees with the experimental result mentioned above reported by Lohrmann and Buchner [32], and lends further support to the importance of flame size as a dominant characteristic of the flame dynamics, as discussed previously.

1.4.2 Use of Systems Models for Instability Prediction

In addition to predicting the behavior of the flame, the ability to predict when instability will occur with respect to operating conditions is important. This can be done using the

system level stability models discussed previously. There is some variation in the literature about the form of such a model, but a simple example is shown in Figure 1.1. The real challenge in using this type of model successfully lies in accurately predicting the individual blocks that make up the closed loop.

Techniques for obtaining the acoustic transfer function through experimental measurement and linear finite element models have been thoroughly detailed by Black [3] and Paschereit et. al. [38]. A stochastic mixing model, which was observed to produce good dynamic results, is discussed by Martin [33]. The flame transfer function has previously been obtained using reduced-order modeling techniques as discussed previously. Experimental measurements of the flame transfer function exist but have not been applied to system model predictions of instabilities. Predictions of unstable operating conditions made using these and other techniques for obtaining the transfer functions have exhibited good agreement with experimental stability measurements [12, 20, 33, 37].

1.5 Control of Thermoacoustic Instabilities

Once combustion instability has been characterized and predicted, resolving it becomes the area of interest. This is termed control of combustion instabilities. This can be attempted either through active or passive means. Active control refers to the use of actuation, usually through acoustics or fuel injection, to eliminate instabilities. This type of control has been shown to be effective, but has been somewhat pushed aside in favor of passive control to avoid the additional hardware and design issues necessary to implement active control in practical systems. Passive control, in contrast, uses design stage modifications to avoid instabilities. Passive techniques may function by avoiding instability by changing acoustic or mixing dynamics to move desired operating conditions into a safe region of the stability map. Alternatively, they may attempt to directly interrupt the coupling mechanism between the flame and acoustics, such as by breaking up the large-scale vortex structure formation.

For the purposes of this study, control is most interesting in the way that it provides insight into the coupling and stability of a combustion system. Passive control studies

have revealed a wide variation in technique. Some studies have shown that modification of the acoustic characteristics using orifice plates or geometry modifications may allow instabilities to be avoided [23, 45]. Other studies relying on modification of the stabilization region (e.g. changing the shape of the centerbody or rapid expansion) have shown good results, by preventing the formation of vortex structures, eliminating the flame-acoustic coupling mechanism [16, 43].

Chapter 2 - Experimental Configuration

2.1 Identification of Need

Though combustion dynamics has been the arena of many years of experimental, theoretical and computational research, questions still remain. Flames have been observed to behave in a manner similar to a low-pass filter. However, the specific physical mechanisms which cause this behavior are not well established. Additionally, predictions of combustor stability from a systems theory paradigm have been made in the past, but not through explicit use of experimentally measured transfer functions. It is hypothesized, based on literature and previous work, that moving beyond global measurements of the flame heat release rate into spatially based measurements of flame dynamics is necessary in order to resolve the link between the proposed coupling mechanisms and the flame dynamics. Resolution of this unknown is also tied to use of system theory based stability predictions, as will be described in more detail below.

The observation that spatially based measures are necessary for characterization of flame dynamics has significant ramifications for stability prediction. According to systems theory, determination of stability relies on evaluation of the magnitude (gain) of the open-loop transfer function at critical points. Since the dominant changes in transfer function with respect to operating conditions come from the flame, the flame transfer function must be consulted to discern how changes in operating condition or fuel composition affect stability. Since the flame has been observed to have a simple low-pass filter characteristic, the gain and cutoff frequency are the most important parameters in characterizing the flame transfer function, with increases in bandwidth or response magnitude expected to result in a higher incidence of instability. The gain appeared, in agreement between experiment and models, to be related to the heat-release rate of the reactants. Following the discovery that the bandwidth of the flame is related to the flame size, published literature was reviewed with critical attention paid to interpreting the behavior observed by other investigators relative to this parameter.

Looking at published stability trends cited previously and flame FRF behavior, evidence supporting the dominance of flame size was observed. Small increases in mean

equivalence ratio from lean operating conditions would be expected to result in a shorter residence time as a result of increase in flame speed. As such, the residence-time-based approach would suggest that increasing equivalence ratio would result in increased bandwidth of the flame FRF and instability would be promoted. This predicted trend matches published observations and past work by Virginia Active Combustion Control Group (VACCG) researchers [22, 33, 45]. As with varying equivalence ratio, changes in atmospheric condition which impact reaction rate, such as temperature and humidity, would be expected to be the dominant atmospheric characteristics in terms of effect on stability behavior, a fact confirmed by Janus et. al. [21]. Finally, as mentioned previously, work by Lohrmann et. al. [32] showed that the bandwidth of the flame FRF can be observed to have a constant value with respect to Strouhal number. The characteristic length in the Strouhal number used by Lohrmann et. al. is the axial position of the maximum heat release, which was found by the same investigators to be linearly related to the length of the flame. As such, the Strouhal number that resulted in a constant bandwidth for the flame can be rewritten to relate to the residence time used by Martin in well-stirred reactor based flame models [33], as shown in Equation 6.

$$St = f\frac{x_o}{\bar{u}} = f\tau_{res} \tag{6}$$

Though the majority of existing data deals with dynamics of hydrocarbon fuels, recent interest in fuels high in hydrogen content has begun to result in data for stability of these high-hydrogen fuels, including those generated from coal gasification processes (syngas). In general, increasing the amount of hydrogen found in a fuel results in an earlier transition to instability [46], behavior still predicted by the residence time due to the high flame speed of hydrogen [30, 52]. Higher frequencies of pressure oscillations have also been observed when dealing with high-hydrogen content fuels [48], a fact which further supports the explanation of increased flame FRF bandwidth due to a smaller flame.

All of the results detailed above provide evidence for the flame size dependence of the transfer function bandwidth. Well-stirred modeling efforts conducted by Martin [33] showed that while a well-stirred reactor relies on a predetermined flame volume constraint, application of certain volumetric constraints could result in a dynamic

response similar to that observed in experiment. It remains, therefore, to make measurements directly of how the flame spatial characteristics behave in a dynamic manner to provide the necessary experimental backing for future modeling efforts with respect to this new spatial methodology. The goal of this study, therefore, is to make measurements of flame dynamics including the dynamic response of the flame spatial characteristics (volume and offset) for the case of velocity perturbations. The dynamic spatial characteristics of the flame will be measured and compared with the average transfer function between the velocity excitation and the flame heat release rate. These will be used to further the understanding of flame dynamics, and will be applied in an attempt to make closed-loop stability predictions, to test the application of this extended flame transfer function insight in a way that can be applied for combustion system design.

2.2 The Proposed Work

In order to make measurement of the spatial dynamics of turbulent premixed flames, a study was proposed and executed in two parts.

- First, Phase One, dynamic measurements were made of the spatial distribution of the flame. These measurements were used to obtain the dynamic response of the flame volume and the position of the center of flame heat release rate in response to velocity perturbations. These dynamics were compared with those of the flame heat release rate transfer function. These measurements were used to develop a predictive capability for the characteristics of the flame heat release rate transfer function, used in closed-loop stability predictions.

- Phase Two of the proposed study applied measurements of the flame transfer function and acoustic transfer function in the closed-loop system model to make predictions of the occurrence of instabilities. These predictions were intended to validate use of the experimentally obtained flame transfer functions for prediction of instabilities in the self-excited combustor.

Details about these two phases is provided below.

2.3 Experimental Methodology

2.3.1 Phase 1

The overall goal of Phase 1 of the study was to determine the relationship between the dynamics of the spatial characteristics of the flame and the previously measured dynamics of the flame heat release rate. This is motivated by the observed behaviors of the heat release rate dynamics bandwidth with respect to operating condition and the correlation with the bandwidth behavior that would be expected due to variations in the flame size. An overall outline of the methodology used for Phase 1 follows.

As with previous studies of the flame dynamics by the VACCG, open loop measurements of flame dynamics were chosen. This is preferable to closed-loop, or self-excited, measurements in that they allow the flame dynamics to be looked at individually and the pertinent characteristics and behaviors to be ascertained. To make this type of measurement, the excitation is introduced to the system externally. Both the excitation and the response are then measured, providing a measurement of both the input and output which lead to a transfer function.

For this study, only velocity coupling was considered. This decision was made in the interest of focusing on developing a new flame dynamics measurement methodology, with extension of the technique to other cases left for future work. Elimination of potential equivalence ratio fluctuations was accomplished through rig design and is detailed further in Section 2.4.

Obtaining some measure of the spatial nature of the flame was necessary for comparison with the heat release rate. For the purposes of this study, several different possible spatial characteristics were considered. Details of how these characteristics were measured are provided in Section 2.6. The primary characteristics which were considered were the volume of the reaction region and the streamwise distance from the fixed dump plane to the center of the flame heat release. The interrelationships between these quantities as well as their relationship with flame heat release rate were considered.

2.3.2 Phase 2

Phase 2 of the study was conducted with the intention of applying the measurements using a closed-loop model for the prediction of stable operating conditions. The closed-loop model used is that shown in Figure 1.1. For the purposes of this study, the combustor was modified using a long combustion section added on to the end of the rig. This section was sufficiently long as to result in acoustic self excitation of the combustor. The instabilities of this self excitation were mapped with operating condition for the purposes of comparison with predictions.

Predictions of the unstable behavior were made from direct measurements of the flame transfer function from Part 1, and a direct measurement of the acoustic transfer function of the extended combustor made as Phase 2 of the study. These two transfer functions may be combined to form the "open loop transfer function" of the combustor, which may be used to predict unstable operating condition. The specifics of how the predictions of stability limits were made are expounded upon in more detail in Section 2.11.

2.4 Experimental Configuration

The experimental apparatus used in this study is the VACCG Lean Premixed Turbulent Combustion Rig. The rig is vertically aligned with flow entering at the bottom and combustion occurring at the top, with the products exhausted by a duct located above the apparatus. The rig has had some modifications since its previous use by Khanna [22] and Hendricks [18]. The rig remains made of carbon steel painted to resist corrosion. The overall structure of the rig however, has been modified through shortening in order to reduce any potential influence of the acoustic modes on the transfer function measurements. Additionally, a different set of diagnostics were used, most significantly in the velocity measurement.

2.4.1 Fuel and Air Delivery System

The lead up to the inlet to the rig is made up of the fuel and air storage, measurement and delivery systems. Air is compressed and delivered to the test cell by an Ingersoll Rand compressor located outside the lab. Air is delivered continuously at 1034.2 kPa (150 psi) and regulated down to 275.8 kPa (40 psi) before reaching the flow meter. Two separate

air flow trains are available for use depending on the flow rates of air desired. In this case, the smaller of the two air flow meters was used corresponding to the relatively low flow rates considered. Flow was measured using an Elridge Products model 8710NH-SSS-000-DC24-AIR hot-film mass flow meter. This flow meter was calibrated using the VACCG orifice flow meter calibration rig, according to the operating procedures described in the internally developed documentation for that apparatus. Air flows for this study were able to be reliably varied within the calibration from 5.43 to 16.3 g/s (10 to 30 SCFM). Flow rate was controlled by manual operation of a needle valve.

Fuel delivery was more complicated due to the consideration of multiple fuels. Natural gas was compressed from the local pipeline into an outdoor high pressure storage tank, from which it was delivered into the test cell. The flow rates required for test conditions considered in this study did not result in any practical limitations on the experimental capability due to this blowdown mode of operation. Other fuels were stored in gas cylinders within the test cell and delivered through piping to the flow meters. All fuels were regulated to 275.8 kPa (40 psi) prior to flow metering to correspond to the calibration pressure of the device. Likewise with air, two separate flow trains were available for fuel delivery, though both were fed by the same source. For this study the higher flow rate fuel line was chosen. The fuel flows were measured using Hastings model HFM-201 hot-film mass flow meters, with the calibration checked against a bellows flow meter timed with a stopwatch. Similarly to the air, fuel flow rate was controlled by a manual needle valve.

Mixing of fuel and air occurred in a specially constructed mixing section. This section consisted of a blanked off length of tube with a ring of small holes drilled around the circumference. This tube was inserted into the straight arm of a standard pipe tee, as seen in Figure 2.1, such that the holes were located at the intersection with the perpendicular arm of the tee. The blanked tube was fed by fuel, with air entering from the perpendicular arm resulting in a highly turbulent air stream at the fuel injection point. This mixed charge was then split into four separate streams which were delivered to the rig through at least 0.91 meters (3 feet) of plastic tubing. Injection of the premixed flow into the rig occurred in the upstream-most section of the rig through four tubes inserted

into the rig with holes drilled on opposite sides, radially, along their length. The holes in each of these injection pegs were aligned perpendicular to the flow path in the rig. This injection scheme was designed to ensure that acoustic interactions with the fuel injection could not result in oscillations in the flow equivalence ratio which could be convected to the flame and result in the potential for undesired heat release rate oscillations.

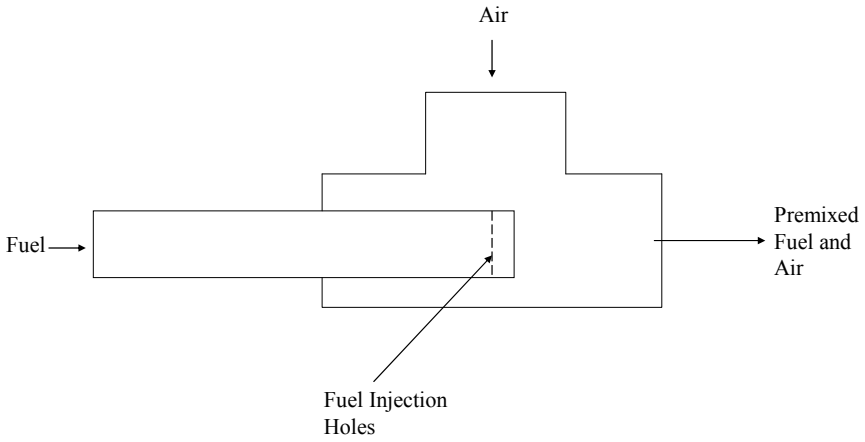

Figure 2.1 – Sketch of fuel/air premixer.

When combustion tests were performed, the rig was allowed to run lit to reach a steady state temperature. The required warm up time of 30 minutes was determined by making measurements of the heat release rate and the velocity power spectra as the rig was heated.

2.4.2 Description of Experimental Apparatus

The rig itself consisted of several sections, numbered from the bottom up. As mentioned these sections were aligned vertically in a stack, with flow in an upward direction and combustion occurring at the top of the rig. The rig differs from that originally designed for use by the VACCG in that the acoustic profile was altered so as not to potentially interfere with the open-loop dynamic measurements. The rig exhausted into the experimental ventilation ducting in the lab located above the combustion section. All of the sections were connected via flanges with O-Ring face seals. The rig itself was supported from below by a frame constructed to hold the rig in position. Figure 2.2 shows a picture of the rig in its standard operating configuration, used in Phase 1 of the

study. Accompanying this image is Figure 2.3, which depicts the standard operating configuration in cross section, and provides dimensions. Additionally, the rig could be configured for self excited operation by installation of an extended combustion section, as pictured in Figure 2.4. This configuration was used for the unstable measurements made in Phase 2.

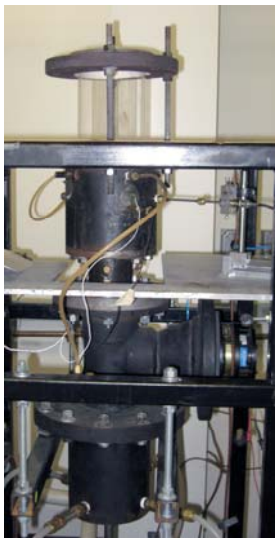

Figure 2.2 - Experimental apparatus in standard operating configuration. Acoustic driver and hotwire anemometer are visible in their installed locations.

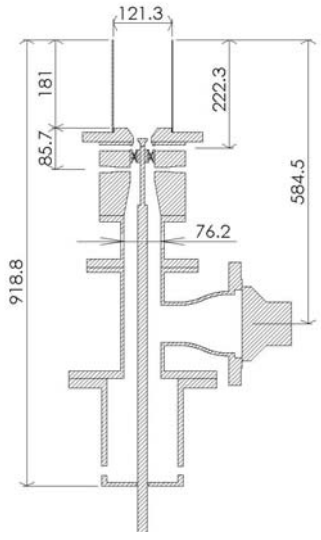

Figure 2.3 - Dimensioned drawing of the rig in standard operating configuration. Dimensions are in millimeters.

Figure 2.4 - Rig configured for self-excited operation.

The several sections of the rig as assembled are shown and labeled in Figure 2.5. Section 1 of the combustor contained a large cavity into which the aforementioned premixed charge injection occurred. This section was capped with a honeycomb and a perforated plate for flow straightening. Further, a water cooled lance containing the centerbody and the flow channels for secondary fuel injection (unused in this study) was inserted at the base of this section, which will be described in more detail later. The second section of the combustor consisted of a large pipe tee section with an expanding branch on the arm of the tee perpendicular to the flow. This expanding branch was capped with the speaker for exciting the velocity, or a plain blanking plate for Phase 1 (open-loop operation) and Phase 2 (self-excited operation) of the study respectively. Topping section 2 was section 3, a section of straight pipe with various measurement ports available for separate acoustic characterization studies. Section 4 of the rig was a section designed for diagnostic access immediately upstream of the combustion region. This section consisted of a converging passage followed by a straight passage. Various diagnostic ports, including access for the hotwire probe and laser diagnostic ports existed in this section.

Additionally, near the top of this section, the swirler was mounted via set screws inserted through the outer shell. A specially designed collar filled the gap between the swirler and the centerbody support, and ensured that the centerbody remained in the center of the flow passage. A circular water cooling channel was cut into the top of the fourth section. This was fed by a continuously flowing water line to cool the rig. As with the flow passages, this water cooling section was sealed using an O-Ring face seal with the section above it. The fifth section of the rig was a short expanding duct followed by the rapid expansion or "dump." The combustion section was placed directly atop this.

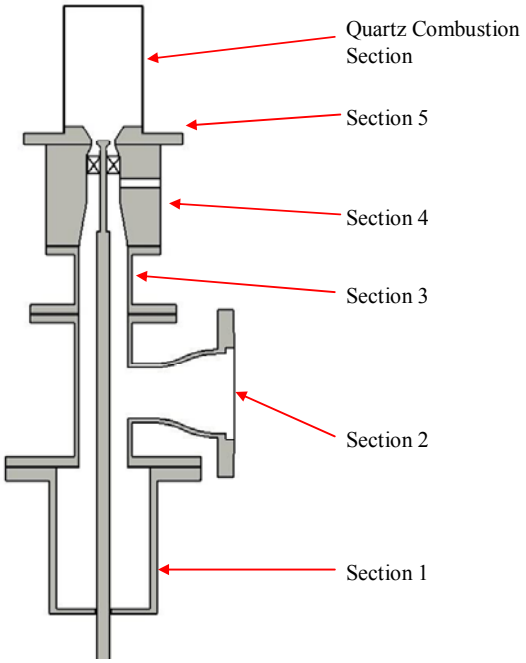

Figure 2.5 - Sketch labeling the sections of the rig as described in the text. Note that not all features of the rig are shown.

For Part 1 of the study, the combustion section consisted of a 121 mm (4.75 inch) diameter, 191 mm (7.5 inch) long round quartz tube, open to the atmosphere. This tube was held in place using FiberFrax insulation and was encircled by a holder at the top to ensure that it did not topple. A cross sectional diagram of the complete rig including the quartz tube combustion section is in Figure 2.3, along with a picture of the rig assembled in this manner in Figure 2.2. For Phase 2 of the study, sections 1 through 5 of the rig remained the same. Above section 5 however a longer 0.85 m (33.25 inch) steel section

containing rectangular quartz windows was mounted in place of the quartz tube. Three window mounting locations were available. This section contained a single 6.4 mm (¼ inch) access port at the same axial location as the windows. A picture of the rig assembled for these self-excited measurements is in Figure 2.4.

The centerbody consisted of a 19.1 mm (¾ inch) diameter circular obstruction to the flow held in place by a lance inserted through the bottom of the rig. The centerbody was internally cooled by water fed through the center of the lance. A photograph of the centerbody as installed in the rig may be found in Figure 2.6. The centerbody was positioned such that its top surface was 2.5 mm (0.1 inch) below the beginning of the expanding duct in section 5 of the rig. The relative position of the centerbody as installed may be seen in Figure 2.7. The narrowest flow passage of the rig is found coincident with the centerbody mounted in this location, resulting in a flow area of 854 mm^2. As mentioned previously, the centerbody was aligned in the center of the flow by a collar held in place within the swirler. As the swirler was mounted, it was positioned such that the centerbody and the swirler remained centered in the flow channel. The lance which held the centerbody also held an additional axially-positionable jacket with a set of injection ports, which were not used in this study.

Figure 2.6 - Image of the centerbody as installed in the rig.

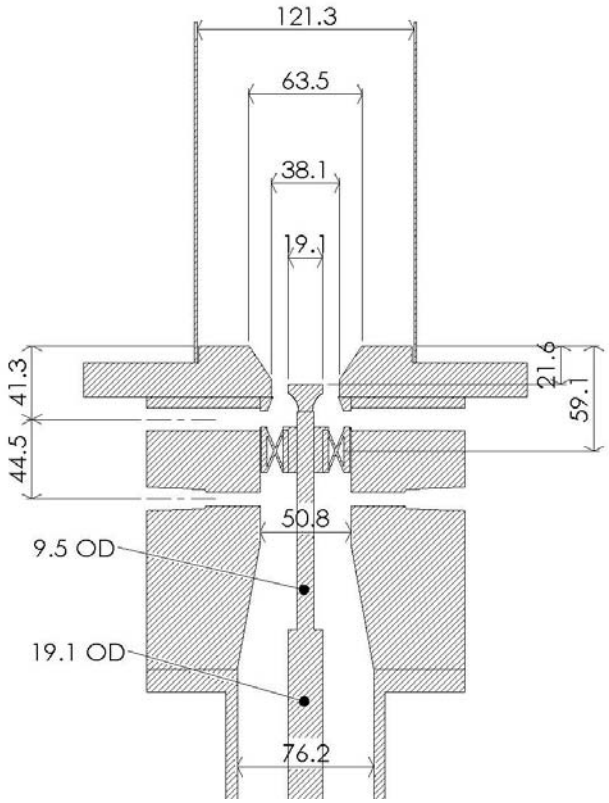

Figure 2.7 - Enlargement of a drawing of the final sections of the combustor in its standard configuration, showing the positioning of the centerbody and swirler relative to the rapid expansion, as well as the flow passage dimensions. Dimensions are in millimeters.

The swirler used for this study was a brass, straight-vane swirler with a vane angle of 30 degrees from the axial direction. The swirler had an outer diameter of 42.9 mm (1-11/16 inches) and a center hub diameter of 12.7 mm (1 inch). This allowed the geometric swirl number to be approximated according to the equation [31]:

$$S = \frac{2}{3}\left[\frac{1-\left(d_h/d_o\right)^3}{1-\left(d_h/d_o\right)^2}\right]\tan(\theta) \tag{7}$$

For this 30 degree vane angle swirler, this resulted in a swirl number of 1.23. A drawing of the swirler is presented here in Figure 2.8. As mentioned previously, the swirler was

mounted within section 4 of the rig (see Figure 2.7) and was held in place by a pair of set screws. The mounting of the swirler was responsible for the alignment of the centerbody, via an alignment sleeve which fit inside the swirler and held the centerbody in place. A picture from the top of the quartz combustion section, in which both the centerbody and swirler are visible is shown in Figure 2.9.

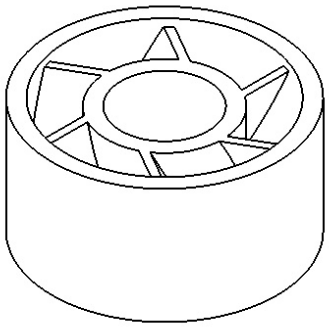

Figure 2.8 - Drawing of the fixed-vane swirler used in this study.

Figure 2.9 - Photograph of the quarl from the top of the quartz combustion section in which the centerbody and swirler are visible as installed for use.

2.5 Diagnostics

A variety of diagnostics were used for measurements made in this rig. A simple sketch in Figure 2.10 shows the locations of these diagnostics in the flow train. A more detailed description of each of these diagnostics follows.

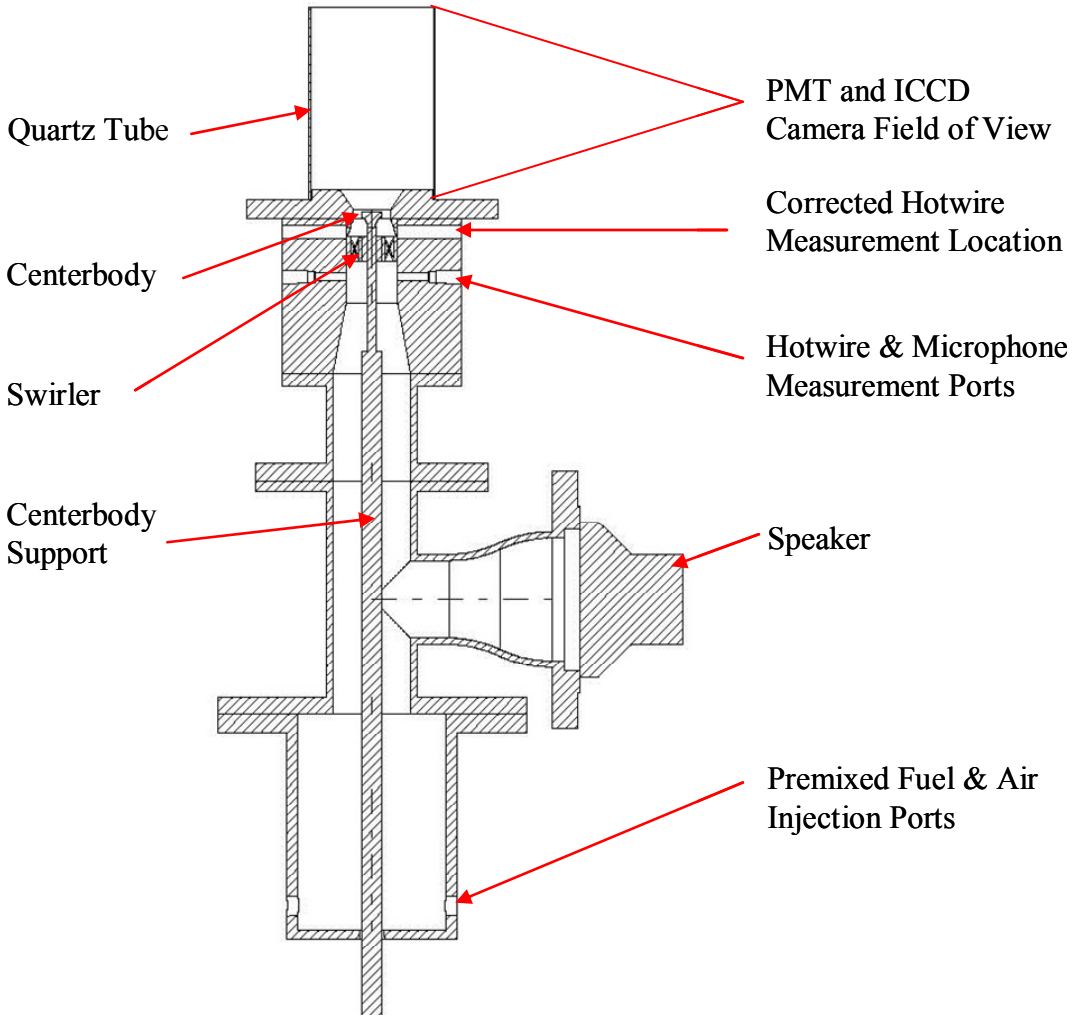

Figure 2.10 - Labeled drawing of the combustor in cross section.

2.5.1 Hotwire anemometer

Hotwire anemometry is a velocity measurement technique that works on the principle of proportionality between convective heat transfer and flow velocity. A single, small diameter wire on a probe was inserted into the flow, with the wire arranged in a

circumferential direction to the flow cavity. This allowed for measurement of both the axial and radial flow components, though the radial component of flow velocity was assumed to be negligible. The hotwire in the current study was operated in constant temperature mode. In such a mode of operation, the resistance of the wire is controlled to a constant level. As flow passes over the wire, it is cooled through convective heat transfer, resulting in a change in the temperature of the wire. The anemometer circuitry senses the decrease in resistance associated with this temperature drop and compensates by increasing the current flowing through the wire, returning the resistance, and therefore the wire temperature, to its set point. This current is converted to a voltage for measurement, yielding an output measurement with theoretical proportionality to flow velocity.

The hotwire probe must be calibrated to measure a velocity, as the natural output of the device is a simple voltage signal. The range and offset of the hotwire output are first properly set for the flow velocity with the probe in the rig. This is generally set over a range of +/- 3.5V for the mean flow. This utilizes as much as possible of the DAQ system's +/- 5V range while still allowing for the dynamic response. The hotwire calibration was then performed on a separate air tunnel, using a pitot probe as a velocity reference. The pitot tube stagnation pressure was measured relative to the atmospheric air using an electronic pressure transducer with a range of 0 to 0.1 inches of water. Stagnation pressure may be related to velocity for a pitot tube using the following relationship.

$$u = \sqrt{2\frac{p - p_{atm}}{\rho}} \tag{8}$$

The calibration jet is open to atmosphere and is driven by the same compressor supplying air to the rig. The total flow was varied over the hotwire operating range to generate a calibration curve for conversion between volts and velocity. A sample calibration is shown in Figure 2.11, with the data appearing as points, and a quadratic best fit as a dashed line.

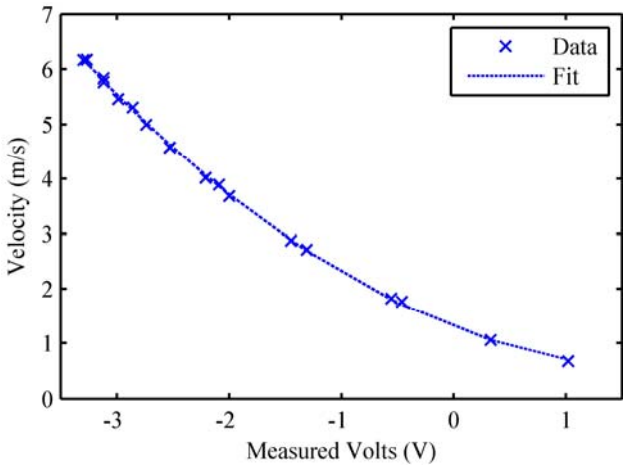

Figure 2.11 - Sample hotwire calibration measurement with quadratic best fit.

In addition to the need for calibration of the hotwire signal, the hotwire measurement needed to be corrected to account for its position. As seen in Figure 2.10, during flame tests, the hotwire was positioned directly upstream of the swirler. This was necessary to protect the hotwire from the harsh environment present in the combustion region. The dynamics associated with this position were accounted for with cold flow measurements. A transfer function was first measured between the hotwire in its usual location upstream of the swirler and a reference microphone inserted into the flow. This measurement was performed using the same manner of sine dwell excitation used for the flame transfer function measurements. More details on this excitation technique may be found in Section 2.7. A second hotwire transfer function was measured with the hotwire placed downstream of the swirler, immediately upstream of the rapid expansion where flameholding occurs. These transfer functions were multiplied such that the effects of the reference microphone cancelled out, leaving only a transfer function between the hotwire in the two locations, as shown in Equation 9.

$$\frac{u_m'}{u_f'} = \frac{u_m'}{p'} \cdot \frac{p'}{u_f'} \tag{9}$$

When considering the flame dynamics, this cold flow hotwire transfer function enabled correction for the hotwire measurement location as seen in Equation 10.

$$\frac{q'}{u'_f} = \frac{q'}{u'_m} \cdot \frac{u'_m}{u'_f} \tag{10}$$

The actual transfer function (u'_m/u'_f) measured for the hotwire is shown in Figure 2.12. Both the magnitude and phase have an additive effect on the flame dynamic transfer function due to magnitude reported in logarithmic units. Thus the maximum impact on the flame transfer function over the range of interest for flame transfer function measurements (0-400 Hz) is approximately -13 dB around 340 Hz. The maximum deviation of the phase is +50 degrees at the same frequency as the peak magnitude deviation.

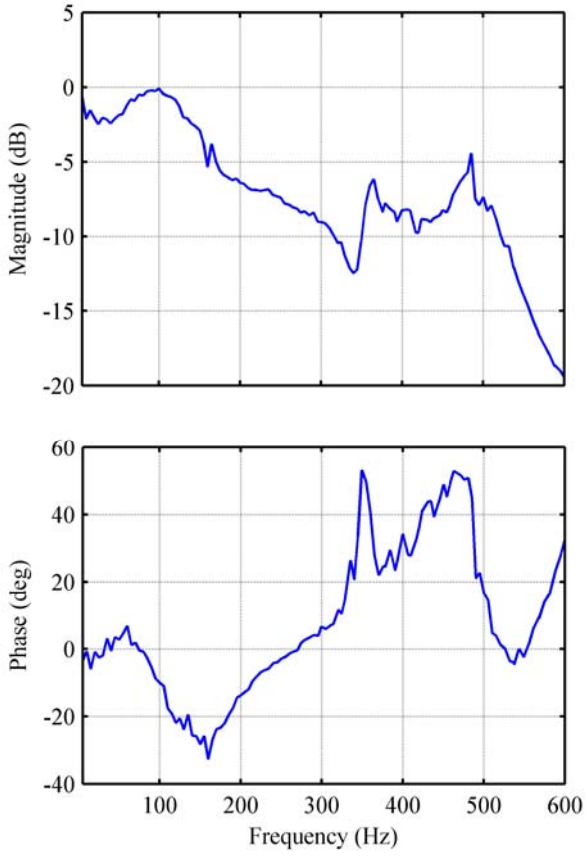

Figure 2.12 - Transfer function for hotwire correction between measurement location and flame.

The before and after effects of the hotwire transfer function correction on a sample flame transfer function may be seen in Figure 2.13. While it appears through inspection that this correction has only a small effect on the overall character of the flame dynamics, when making system theory based predictions of stability, relatively small changes in gain, magnitude and phase may still have an impact, particularly on the location of phase crossings. This correction was applied to all measurements made in this study that used the hotwire as a transfer function input or output.

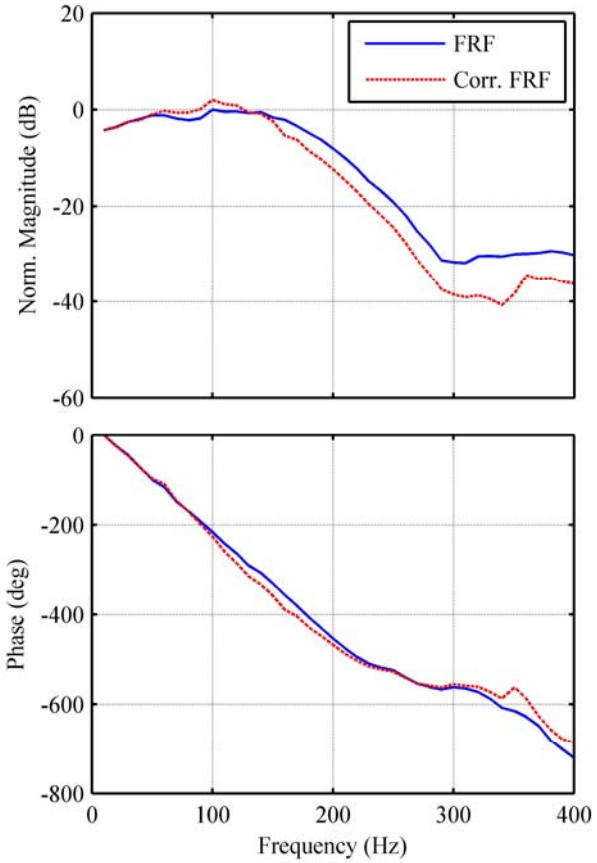

Figure 2.13 - Sample flame transfer function showing the effects of the hotwire measurement position correction.

2.5.2 Microphone for Dynamic Pressure Measurement

A Kulite brand high temperature microphone, model MIC-152 HT, was used as a measurement of the combustor sound pressure level during the self-excited operation.

The microphone was inserted into the flow at the same axial location as the hotwire measurement port, and was held in place and sealed using modeling clay. The microphone was calibrated to provide measurements in Sound Pressure Level using a GenRad 1562-A microphone calibrator. This calibration provided a known 114dBSPL sound source at several frequencies, and was used to calculate the correct gain for the microphone. This gain was found to be around 58dB (a factor of about 800), in addition to a fifty-times amplification applied by the data acquisition system.

2.5.3 Flame Heat Release Rate Measurement Using OH* Chemiluminescence

The flame heat release rate was observed using a measurement of the OH* chemiluminescence. OH* chemiluminescence has been found by several other investigators to be an accurate indicator of flame heat release, and as has been mentioned, is a common indicator in use for this purpose [17, 26]. In the current study, measurement was made using a photomultiplier tube (PMT) filtered at the ultraviolet OH* emission band of 308nm. The filter used had a FWHM bandwidth of 10nm. Photomultiplier tubes produce a low magnitude DC current signal proportional to incident intensity, so additional signal conditioning is necessary make voltage measurements. A current-to-voltage amplifier, shown in Figure 2.14, was used for this purpose. The circuit had an adjustable gain by means of a potentiometer. This was used to adjust the gain such that at the maximum measured intensity, including dynamic excitation, the reading would be within the acceptable range of the data acquisition hardware.

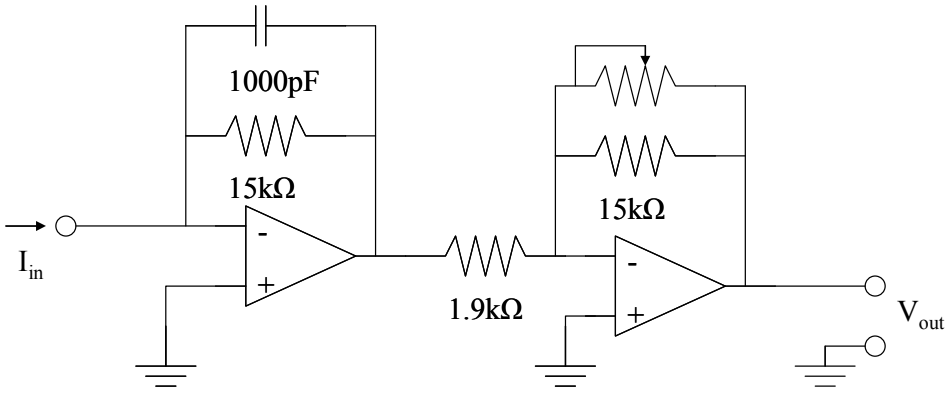

Figure 2.14 - Diagram of current-to-voltage amplifier used for the PMT

The PMT was placed 0.83 m from the centerline of the combustor. A 25.4 mm focal length lens was used in order to provide suitable magnification to image the entire flame on the PMT detector. For the purpose of aligning the instrument, the PMT was oriented such that the measured intensity from the flame was maximized. The dynamic response of the PMT was tested using a steady light source and a beam chopper operated at varying frequency. The response magnitude was found to be very steady over the entire range of the dynamic measurements to be made (0-400 Hz), ensuring the validity of the PMT response over this range. Additionally, the PMT was tested for linearity using the same steady light source and a set of neutral density filters. The results of this linearity test are found in Figure 2.15. Note that the linearity extends well beyond the range available for the data acquisition hardware (-5V as specified in Section 2.10).

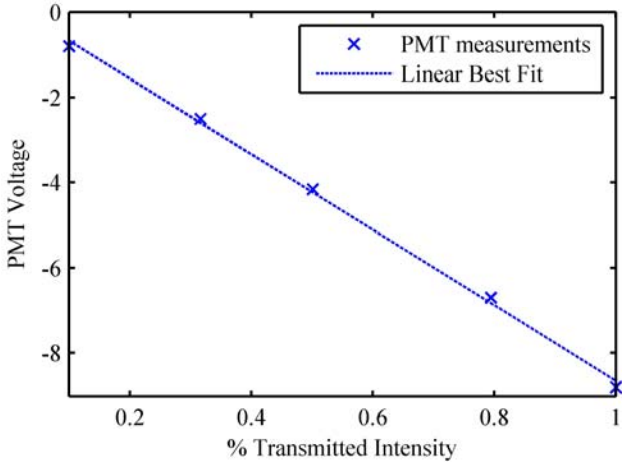

Figure 2.15 - Results of the PMT linearity test.

The PMT was calibrated for measurement of heat release rates in kilowatts using a complete combustion model based on the heating value of the fuel, given by Equation 11.

$$q = \frac{\dot{m}}{\left(A/F\right)_{s,m} \cdot \Phi^{-1} + 1} LHV \tag{11}$$

The calibration was performed by measuring the mean intensity of the PMT signal as a function of both total flow rate and equivalence ratio, matched to the predicted results from this calculation. A linear fit was used at each individual flow rate, with the slope of

the line varied as a function of mean flow rate. Since the measurements in question concerned dynamics, the steady absolute values of the heat release rate were unimportant and thus, only the slope of the linear fit was considered. The data used for the PMT calibration data is presented in Figure 2.16.

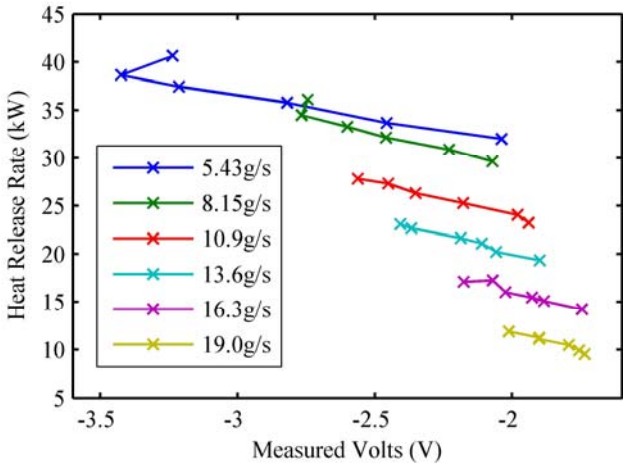

Figure 2.16 - PMT calibration results for a variety of flow rates.

It was observed by Lee et. al. [26] that when using OH* chemiluminescence as an indicator of flame heat release rate, it is important to correct for variations in underlying CO_2* chemiluminescence. The CO_2* chemiluminescence has a dependence on heat release rate which may otherwise introduce a false gain in the heat release rate measurement. This was observed by Lee et. al. to have a significant effect, particularly with equivalence ratios approaching stoichiometric. To correct for this potential error, measurements of the heat release rate as a function of equivalence ratio were made to verify the linearity of the OH* chemiluminescence response as an indicator of heat release rate for the flow conditions in this study. The results of this measurement are in Figure 2.17. While it is true that the intensity of the OH* chemiluminescence does not result in a linear relationship with respect to equivalence ratio, it's deviation from a linear trend over the primary range of equivalence ratios considered in this study (0.58-0.7) was considered to be negligible.

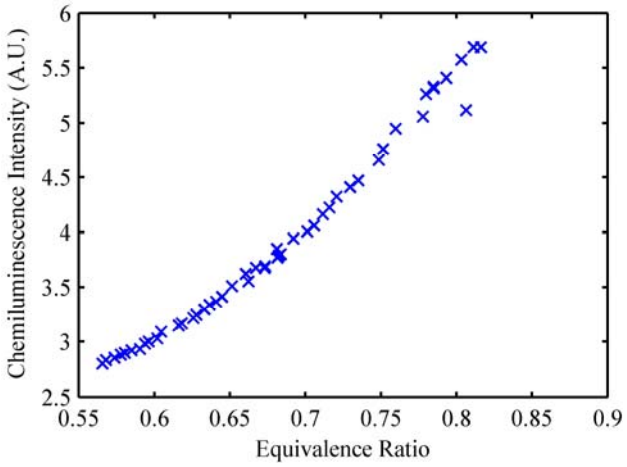

Figure 2.17 - OH* chemiluminescence intensity normalized by fuel flow rate as a function of equivalence ratio.

2.6 Image Acquisition and Processing

Image acquisition was performed using a Stanford Optics model 4 Quick 05 ICCD camera. This camera had a resolution of 640 by 480 pixels. The camera was equipped with a 51 mm (2 inch) diameter standard camera focusing lens with a 51 mm (2 inch) diameter optical filter at 430 nm to visualize the CH* chemiluminescence. The aperture of the lens was fully open to allow the highest possible level of intensity to be detected. The camera was positioned with the lens 1.02 m (40 inches) from the flame centerline. Image capture was achieved using National Instruments IMAQ hardware and software. A sample image of the camera field of view, including a ruler for size calibration is shown in Figure 2.18.

2.6.1 Details of Camera Operation

When imaging the flame, intensifier gain and exposure time were adjusted to ensure sufficient measured intensity. The baseline exposure time was 0.5ms, and this was only changed when necessary to provide additional illumination. In general, variation from this exposure time was only necessary for the leanest test cases, due to their lower levels of overall heat release rate. A total of 500 images were phase averaged pixel-by-pixel to obtain and store one final average image of the flame at a given excitation. Images were saved in uncompressed 8-bit grayscale bitmap format.

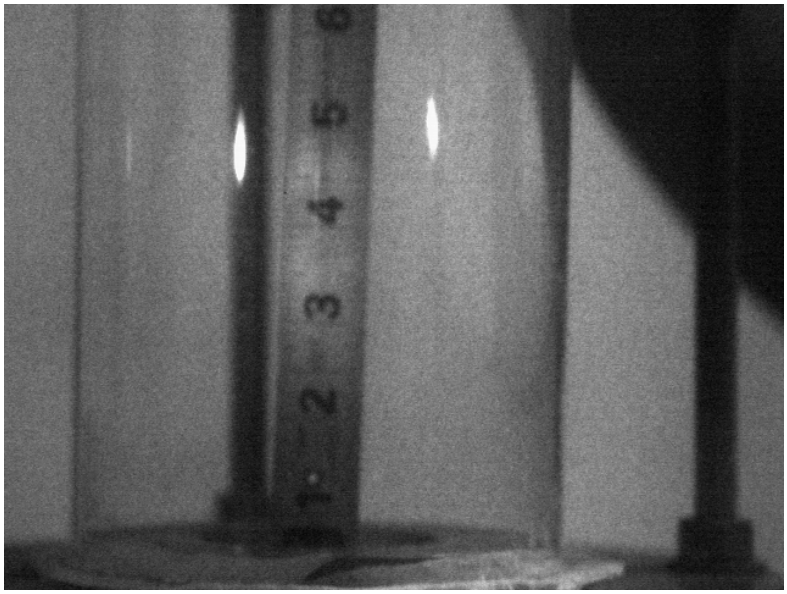

Figure 2.18 - Sample image showing the field of view of the camera, including a ruler for conversion to physical units.

For all tests, the camera was triggered using an external source. A square wave with amplitude of 5 Volts was generated using National Instruments LabView. This signal was generated simultaneously with the speaker excitation signal, to ensure that they remained properly relative in phase. This signal was converted into a TTL pulse suitable for triggering the camera by a custom circuit. Dynamic measurements of the flame size were made by shifting the phase of the trigger signal relative to the speaker excitation signal. Images of the flame at ten separate phases were obtained in this manner, at evenly spaced (36 degree) phase angle increments.

2.6.2 Image Processing

All image processing was performed using software written in Matlab. Processing required several steps to extricate the necessary information. Normalization was performed to allow a uniform intensity for later processing. This was necessary due to the fact that the camera gain was varied due to varying overall flame intensity at different operating conditions. Since these images are by nature line-of-sight, deconvolution was performed to obtain a true cross-section. As part of the flame volume calculations, thresholding was performed on the deconvoluted image, with subsequent pixel rejection

processing to obtain a binary image of the flame. Flame volume was then calculated by integrating this image. More details on each of these steps follow.

Scaling

Images were scaled to fit the range of an 8-bit bitmap. The global minimum value (i.e. the background) was subtracted to provide a background level of zero. The global maximum was scaled such that the resulting maximum was 255. This normalization was found to be necessary due to slight variations in the camera gain and the flame intensity. This enabled a global threshold level to be established, which otherwise would have needed to be varied for each test condition. No information is lost through the normalization process since, as mentioned, the camera gain is necessarily arbitrary.

Deconvolution Theory

While more complicated techniques such as PLIF may offer true cross-sectional measurements of the flame, side view pictures of the flame, such as the ones taken here, are intrinsically line-of sight. What this results in is an apparent weighting of the intensity toward the center of the image due to portions the flame present in the fore- and background of the centerline plane. By making assumptions about the nature of the flame structure, the behavior of this effect can be mathematically described, allowing the apparent intensity to be reversed through deconvolution. An assumption of axisymmetry allows an inversion technique known as an Abel inversion to be used, as shown by Dasch [6]. The analysis used by Dasch is reproduced here to correct for a slight error found in one of the intermediate equations reported in that analysis.

The line-of-sight projection of intensity at a single vertical location in the flame can be described by the following integral [6]:

$$P(r) = 2\int_{r}^{\infty} \frac{r'F(r')}{\sqrt{r'^2 - r^2}} dr' \tag{12}$$

Here, F is the axisymmetric "real" intensity which describes the local intensity of the flame, while P is the projected apparent intensity resulting from the line-of-sight imaging. Obeying intuition, the intensity at position r is affected by all values of intensity at larger

radius (i.e. outside position *r*) but no values at smaller radius. Remembering that *F(r)* is the desired quantity, but *P(r)* is what the camera measures, this equation may be analytically inverted to give the Abel transform:

$$F(r) = -\frac{1}{\pi}\int_{r}^{\infty} \frac{P'(r')}{\sqrt{r'^2 - r^2}} dr' \tag{13}$$

in which $P'(r') = dP/dr$. Following the procedure outlined by Dasch, we may break this integral into a sum of integrations over smaller sections expanded about points r_j, where $r_j = j\,\Delta r$ and $r_i = i\,\Delta r$. We do so by introducing a variable δ_0 representing small changes about r_j.

$$F(r_i) = -\frac{1}{\pi}\sum_{j=i}^{\infty}\int_{-\Delta r/2}^{\Delta r/2} \frac{P'(r_j + \delta_0)}{\sqrt{(r_j + \delta_0)^2 - r_i^2}} d\delta_0 \tag{14}$$

Since the slope of this parabola will not depend on the absolute position, r_j, we may take it to be zero. Remembering that r_{j+1} is equal to $r_j + \Delta r$, we plug in the values for the three points:

$$\begin{aligned} P(r_{j-1}) &= a_0 - a_1\Delta r + a_2\Delta r^2 \\ P(r_j) &= a_0 \\ P(r_{j+1}) &= a_0 + a_1\Delta r + a_2\Delta r^2 \end{aligned} \tag{15}$$

Solving for the coefficients and plugging in for the slope yields the necessary approximation:

$$P'(r_j + \delta_0) = \frac{P(r_{j+1}) - P(r_{j-1})}{2\Delta r} + \delta_0 \frac{P(r_{j-1}) + P(r_{j-1}) - 2P(r_j)}{(\Delta r)^2} \tag{16}$$

Grouping like terms of *P* yields:

$$P'(r_j + \delta_0) = \frac{1}{\Delta r}\left[P(r_{j-1})\left(\frac{\delta_0}{\Delta r} - \frac{1}{2}\right) + P(r_{j+1})\left(\frac{\delta_0}{\Delta r} + \frac{1}{2}\right) - P(r_j)\frac{2\delta_0}{\Delta r} \right] \tag{17}$$

It becomes convenient to redefine a new δ as follows:

$$\delta = \frac{2\delta_0}{\Delta r} \tag{18}$$

Plugging this substitution in yields:

$$P'(r_j + \delta) = \frac{1}{2\Delta r}\left[P(r_{j-1})(\delta - 1) + P(r_{j+1})(\delta + 1) - 2P(r_j)\delta\right] \tag{19}$$

With the new definition of δ a convenient shorthand for the integrals may be written. Applying the definition of r_j and r_i leads to the appearance of integers j and i respectively. Making these substitutions and remembering that the limits must be redefined due to the new definition for δ yields:

$$I_{ij}(n) = \frac{1}{2\pi}\int_{-1}^{1} \frac{\delta^n}{\sqrt{(2j+\delta) - 4i^2}}\, d\delta \tag{20}$$

Substituting this definition along with the slope into the original expression yields:

$$F(r_i) = -\frac{1}{\Delta r}\sum_{j=i}^{\infty}\left[I_{ij}(1) - I_{ij}(0)\right]P(r_{j-1}) + \left[I_{ij}(1) + I_{ij}(0)\right]P(r_{j+1}) - 2I_{ij}(1)P(r_j) \tag{21}$$

Up to this point, the analysis matches that of Dasch [6] exactly, however it was discovered that a sign error is present in his reported evaluation of the *Iij(1)* integrals (though apparently it did not affect the results). The correct equations are presented here.

$$I_{ij}(0) = \begin{cases} 0 & j = i = 0 \text{ or } j < i \\ \dfrac{1}{2\pi}\ln\left(\dfrac{2j+1+\sqrt{(2j+1)^2 - 4i^2}}{2j}\right) & j = i \\ \dfrac{1}{2\pi}\ln\left(\dfrac{2j+1+\sqrt{(2j+1)^2 - 4i^2}}{2j-1+\sqrt{(2j-1)^2 - 4i^2}}\right) & j > i \end{cases} \tag{22}$$

$$I_{ij}(1)=\begin{cases}0 & j<i\\ \frac{1}{2\pi}\left(\sqrt{(2j+1)^2-4i^2}\right)-2jI_{ij}(0) & j=i\\ \frac{1}{2\pi}\left(\sqrt{(2j+1)^2-4i^2}-\sqrt{(2j-1)^2-4i^2}\right)-2jI_{ij}(0) & j>i\end{cases} \tag{23}$$

Returning to the analysis of Dasch, we may represent the deconvolution with a linear operator introduced here:

$$F(r_i)=\frac{1}{\Delta r}\sum_{j=0}^{\infty}D_{ij}P(r_j) \tag{24}$$

Rearranging Equation 21 into this form yields the following for D_{ij}:

$$D_{ij}=\begin{cases}0 & j<i-1\\ I_{ij+1}(0)-I_{ij+1}(1)+2I_{ij}(1)-2I_{ij-1}(1) & i=0,j=1\\ I_{ij+1}(0)-I_{ij+1}(1) & j=i-1\\ I_{ij+1}(0)-I_{ij+1}(1)+2I_{ij}(1) & j=i\\ I_{ij+1}(0)-I_{ij+1}(1)+2I_{ij}(1)-I_{ij-1}(0)-I_{ij-1}(1) & j\geq i+1\end{cases} \tag{25}$$

Note that the special case at *i=0, j=1* arises due to the symmetry about the centerline leading to the property $P(r_{-j})=P(r_j)$.

2.6.3 Implementation of the Deconvolution Technique

For the two dimensional images taken as part of this study, this deconvolution method must be performed on each row of the image, as each axial position in the flame is independent relative to the line-of-sight measurement. In order to prepare the image for deconvolution, the centerline of the flame was found. The centerline was calculated as the mean of the left-most and right-most pixels visible after thresholding the scaled image. That is, the centerline was the geometric center of the flame as measured from its horizontal maxima and minima. The thresholding technique used as part of this calculation is described in more detail below.

Prior to deconvolution, the image was split into two along this centerline. The Abel transform described above was implemented through a Matlab code and was applied separately to each half of the image, one row at a time. The two halves were then recombined resulting in a single image of the flame. Additional scaling of the deconvoluted images was required to obtain meaningful data. The scaling method implemented was based on the intensities of the deconvoluted image. All values less than the mean intensity were limited to zero, while all values five standard deviations or more greater than the mean were capped at the five standard deviation value. The suitable values for these limiting levels were found empirically. The resultant image intensities were then scaled to fill the span of an 8-bit image.

To test this image processing routine, a set of images with a known result were generated. A line-of-sight projection of a transparent hollow cylinder with uniform intensity was simulated. The top view of this image is shown in Figure 2.19. The corresponding side view for this object, with projection effects due to the depth of the image is shown in Figure 2.20.

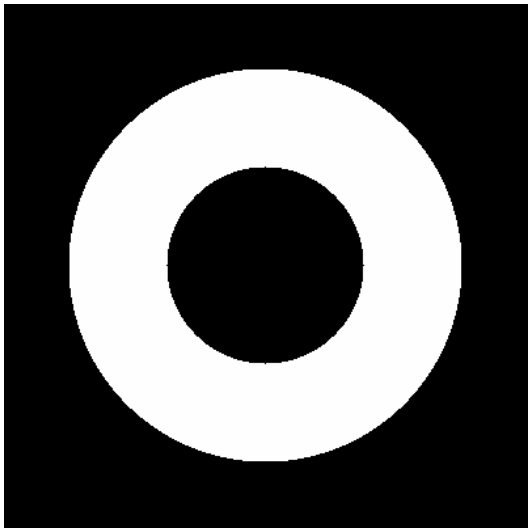

Figure 2.19 - Top view of the sample "object" used to test the implementation and accuracy of the Abel deconvolution scheme.

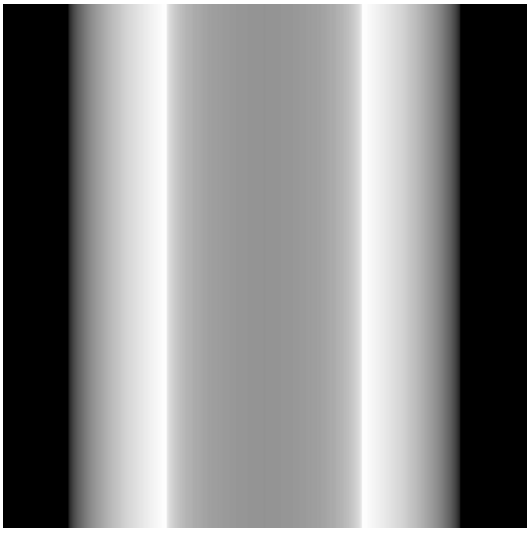

Figure 2.20 - Side view including the simulated line-of-sight effects of the sample "object" used to test the implementation and accuracy of the Abel deconvolution scheme.

The Abel transform deconvolution technique was applied to this side view image, resulting in Figure 2.21. This compares favorably with the expected result (the cross section of the hollow cylinder) shown in Figure 2.22. It is apparent from this comparison however, that a certain degree of noise is inherent to the deconvolution technique.

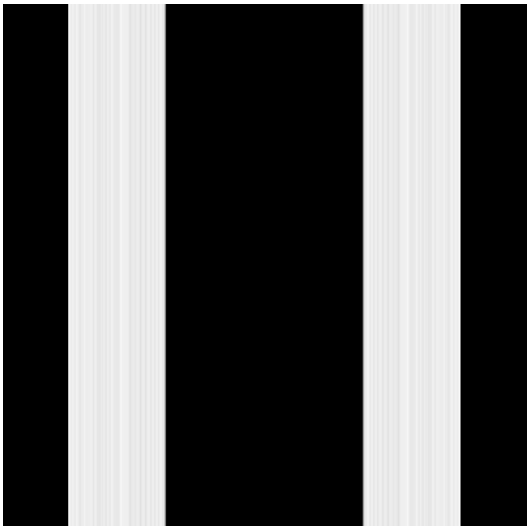

Figure 2.21 - Results of application of the Abel deconvolution technique to the simulated image of the sample object.

Figure 2.22 - Expected result for the test of the Abel deconvolution technique.

A sample line-of-sight flame image, along with its deconvoluted counterpart is shown in Figure 2.23 and Figure 2.24 respectively. Some processing noise is visible, especially along the centerline. This did not have an effect on the volume or offset calculations, as it was removed by subsequent processing.

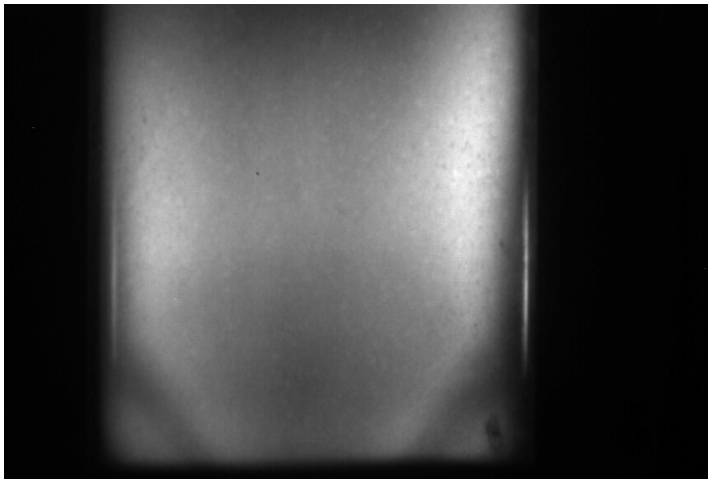

Figure 2.23 - Sample flame image to serve as a test for the Abel deconvolution.

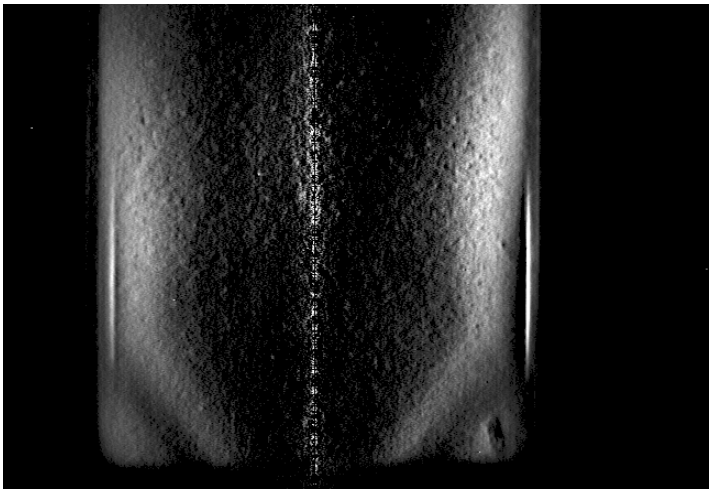

Figure 2.24 - Results of application of the deconvolution processing to the preceding figure.

2.6.4 Thresholding Process

The volume calculation required that a boundary for the flame be established. This was done by setting an intensity threshold for the flame, and reducing the flame to a binary image based on this threshold. The technique used to perform this thresholding was similar to that reported by Sanders [42]. The intensity value at each pixel was averaged with the eight neighboring pixels and this average intensity was compared with the threshold level. The threshold level used was 153 and represented 60% of the maximum of the 8-bit image intensity. This level was determined empirically. A sketch of this process is shown in Figure 2.25. Thresholding the average intensity rather than individual pixels helped as a first step in reducing noise by eliminating outlier pixels.

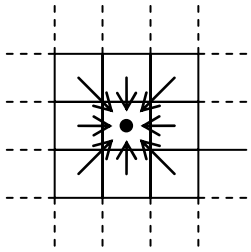

Figure 2.25 - Sketch of the averaging technique used to reduce noise in the image thresholding process.

Further processing of the thresholded image was necessary to provide a suitable image to use as a basis for calculations. It was observed through practice that despite the efforts of the average based thresholding scheme to reduce the level of noise in the image, outliers were still present, notably along the centerline of the deconvoluted image, where processing noise was high. Therefore, built in Matlab image processing functions were used to identify contiguous regions within the images and discard those regions with smaller total sizes than 500 connected pixels. This was found to provide suitable images of the flame boundary at the exclusion of artificial noise.

2.6.5 Calculation of Resultant Image Measures

After the requisite image conditioning has been completed, the desired measurements can be obtained. A sample set of images showing the steps in this process may be found in Figure 2.26. One quantity considered was the offset between the hotwire measurement location and the center of mass of the flame, as labeled in Figure 2.26c. This provided some measure of convective distance for fluid being transported from the hotwire location to the flame. This quantity was believed to be linked to the time delay observed in transfer function phase. The center of the flame however, is a somewhat non-specific term. To be more specific about it, this measure, termed the center of heat release rate, was found by finding the distance from the transformed hotwire measurement location to the intensity weighted center of the flame. This calculation is similar to the finding of a center of mass of an object, however with the weighting being that of local intensity rather than density. The other important flame characteristic obtained from images was the volume of the flame. This metric was obtained by finding the thresholded flame (as seen in Figure 2.26d) and revolving it about its centerline, assuming axial symmetry for each half of the flame. This calculation was performed by applying a shell integration method to the thresholded image, resulting in the resultant volume of the revolved shape, averaged between the two halves of the flame found in each image. In addition, the length and width of the flame were also found. These calculations were made by using Matlab's built-in image processing functions to approximate each half of the flame as an ellipse, with the flame length as its major axis, and the width as its minor.

Since these calculations resulted in units of pixels and pixels cubed for offset (and length) and flame volume respectively, conversion was necessary for measurement in physical units. This conversion was performed using a pixels-to-meters conversion obtained from the visible spectrum calibration image shown above in Figure 2.18. The value for this conversion was found to be 3.2017×10^{-4} meters per pixel. It was assumed that the optical filters had no effect on magnification.

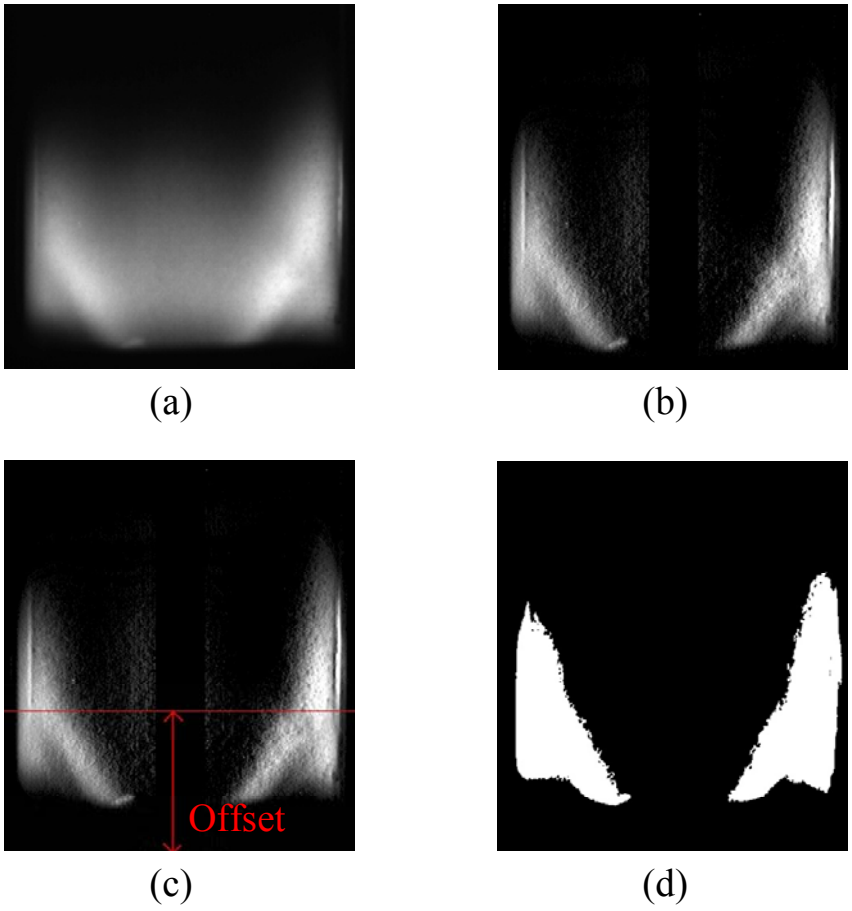

Figure 2.26 - Sample images showing the steps in the image processing technique. a) Normalized intensity image of the flame. b) Deconvolution technique applied. c) Axial center of heat release rate labeled with offset distance marked. d) Thresholded image used for volume calculation.

2.7 Measurement of the Flame Transfer Function

Measurements of the flame transfer function were made according to a general method used by several investigators including those of the VACCG [18, 22, 24, 32]. In this type

of measurement, self-excited oscillations are prevented by limiting the acoustic gain in the combustor. The transfer function was then measured by introducing a perturbation to the flow, and comparing the measurement of this induced velocity oscillation to the response of the flame to this perturbation. In the absence of coupling, this represents the open-loop flame transfer function. The desired dynamics are those between the velocity at the flame, and the flame heat release rate; or in the case of the spatial measurements, between the same velocity, and the volume of the flame or the offset from the measurement to center of heat release rate. As discussed above in Section 2.5.1, this transfer function was corrected for the hotwire measurement location, due to the fact that the hotwire could not survive the high temperature flame region. This correction follows in Equation 26 (same as Equation 10), where the heat release rate fluctuations (q') may be replaced with the spatial fluctuations as applicable.

$$\frac{q'}{u'_f} = \frac{q'}{u'_m} \cdot \frac{u'_m}{u'_f} \tag{26}$$

The methods by which the input and outputs of this transfer function were measured are discussed in further detail in the preceding sections. The excitation however bears some further scrutiny.

The excitation was introduced using a DynaVox 140W speaker mounted on a side-branch in the rig, as discussed previously. In order to achieve coherence of the transfer function over a wide variety of excitation frequencies, it was necessary to vary the amplitude of this excitation. Provided that the excitation remains "small," the approximation of a linear perturbation should require that the response will remain proportional to the input. The definition of small, however, is unclear in this case. Balachandaran et. al. [1] and Bellows et. al. [2] found that for velocity excitation amplitudes below of about 15% of the mean flow, the response remained linear. Using this as a baseline, measurements were made to ensure that the transfer function magnitude was not significantly impacted by these amplitude variations. A set of sample plots of this measurement may be found in Figure 2.27. In order to generate this plot, the amplitude of the LabView sine wave output was varied from 0.25 V to 1.5 V (a factor of 6). Since 1.5 V was the maximum

excitation used for any frequency during the actual tests, this spanned the full range used in measurements. The transfer function was then measured between the velocity and heat release rate. While the response decreases in overall magnitude, no significant non-linearity was observed within the excitation amplitudes used in this study.

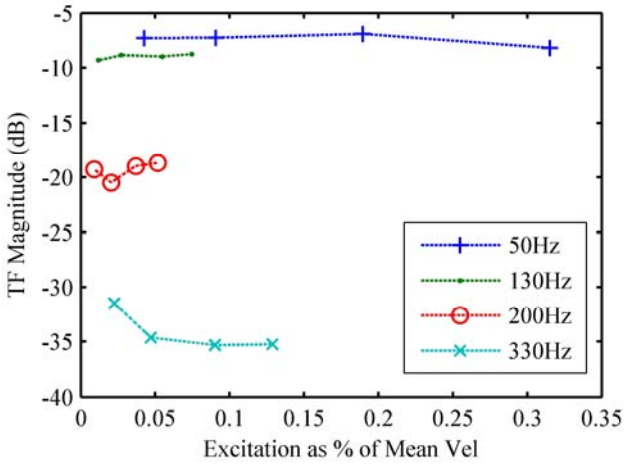

Figure 2.27 - Flame transfer function magnitude as a function of velocity excitation amplitude for several frequencies of excitation.

The amplitudes employed for the speaker excitation as a function of frequency are shown in Figure 2.28. As can be seen, the maximum excitation was around 13% of the mean flow, below the 15% threshold identified by Balachandaran, and within the linear range tested in preparation of this study. Thus, the variation in excitation had no effect on the flame transfer function results measured here.

Thirty seconds of data were acquired at each frequency at a sampling rate of 7500 Hz. Prior to acquisition of the data, the excitation was introduced, and 10 seconds were allowed to elapse to allow any transients to settle out. Since they required separate acquisition, the dynamics images at each frequency were acquired immediately following the main data acquisition.

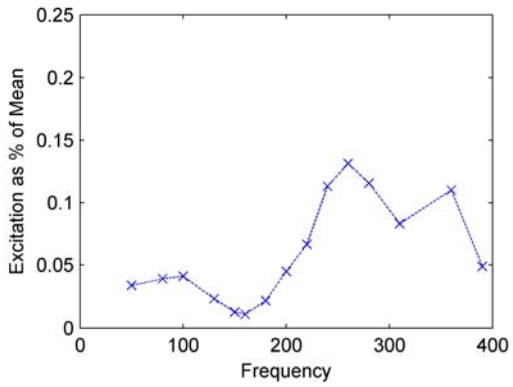

Figure 2.28 – Normalized level of velocity excitation amplitude used in the flame transfer function measurements.

2.8 Acoustic Transfer Function Measurements

For the purposes of making instability predictions, measurement of the acoustic transfer function of the unstable rig was necessary. The rig was first modified to result in potentially self-excited operation by replacing the quartz tube with an optically accessible steel chimney. A picture of the top section of the rig configured in this manner has been shown in Figure 2.29. This configuration allowed sufficient acoustic gain for the rig to become self-excited under appropriate operating conditions.

Figure 2.29 - Close up of the combustion section of the rig configured for self-excited operation.

The actual measurement of the acoustic transfer function was made according to a method described by Black [3]. In this method, nearly identical measurements to the flame transfer function are made, with the important difference that no speaker source is used. The acoustic transfer function is still measured as an open-loop response, but with reversed input and output. Thus the heat release rate is the input of the acoustic transfer function and the velocity the output. Rather than using a speaker to introduce a disturbance into the flow, the source used for these measurements is the flame itself. By using the flame as the source in the measurement, it can be ensured that the acoustic transfer function, rather than the flame transfer function is being measured. During these measurements, operating conditions were chosen such that the flame was operating at as high a power level as possible without actually exciting any instabilities. This was necessary to ensure the highest coherence possible, without encountering any nonlinearities associated with unstable operation that could interfere with the measurement.

To make the measurement, the hotwire anemometer was inserted into the flow in the same location as for the flame transfer function measurements, and the PMT was angled to detect the entire flame. As with the flame transfer function measurements, the hotwire measurement needs to be corrected to the flame position. Since the acoustic transfer function has inverse input and output from the flame transfer function, this correction is performed according to the following relationship:

$$\frac{u'_f}{q'} = \frac{u'_m}{q'} \cdot \frac{1}{u'_m \big/ u'_f} \tag{27}$$

Unlike the sine dwell technique used for flame transfer function measurements, the acoustic transfer function is measured at all frequencies at once, using the flame as a broad band noise source. Thirty seconds of data were recorded to make this measurement. This broad band excitation did result in more difficulty in measuring a coherent transfer function, however, coherence was highest at frequencies with significant acoustic gain. These proved to be the frequencies at which instability

occurred in the combustor, and thus the measurement resulted in an adequate acoustic transfer function for use in the closed-loop system model.

2.9 Mapping of Instabilities in the Self-excited Combustor

It was necessary to obtain a characterization of self-excited combustor behavior with respect to operating condition in order to provide a map of instability occurrence with which to compare the predictions. For this purpose, measurements of the combustor operation in a self-excited mode were made using the extended combustion section, as described in Section 2.4.2. These measurements were made using a time sweep of the equivalence ratio, which was manually varied over the measurable operating range as smoothly as possible using a fuel metering valve. This test methodology was preferable to stationary operating condition measurements, as the combustor operation during attempted stationary mapping was found to be highly variable, and would shuffle back and forth between stable and unstable modes with no deliberate change in the operating condition. Thus, to ensure accuracy in the characterization, the equivalence ratio sweep measurements were made, assuming quasi-steady variation due to the slow adjustments to fuel flow. Operating conditions tested were limited by approaching blowout on the low end, and instability amplitude on the high end. Performance of data acquisition hardware under the high amplitude vibrations introduced into the room due to the instability proved to be the rich limit for operating condition.

The measurements of instability used the microphone pressure measurement (Section 2.5.2) as an indicator of the instability frequency and amplitude. The calibration of this device was detailed in its previous detailed section. The sweep measurements required that time-frequency analysis be performed on the data to obtain a power spectrum. The data was processed in 7500 sample (1 second) chunks with the bounds of this window moving along the total duration of the signal. The equivalence ratio was assumed to be constant for each chunk. Using the relationship between time and equivalence ratio, the results were then rescaled, giving the variation in the calibrated power spectrum as a function of equivalence ratio. Performing this same measurement at a variety of mean flow rate resulted in a complete mapping of the entire combustor operation, for comparison with the instability predictions.

2.10 Data Acquisition and Analysis

All measurements were made using National Instruments LabView software on a Windows based computer platform. The data acquisition card used was a National Instruments PCI-MIO-16XE-10 card with 8 channels of differential input. Prior to this, all signals were passed through a National Instruments model SCXI-1141 Elliptic Filter for anti-aliasing. This filter was set to a cutoff frequency of 2500 Hz to provide sufficient anti-aliasing without interfering with the phase of the signals. Additionally, due to the dynamic nature of the data, a National Instruments model SCXI-1140 Sample and Hold Amplifier was used to simultaneously acquire data from all channels such that the relative phase of the signals was maintained. The hardware had a limiting range of +/- 5 Volts, into which all instruments were configured to read. All data acquisition was performed at a rate of 7500 Hz, a factor of three above the anti-aliasing filter cutoff frequency as required for this hardware to achieve sufficient anti-aliasing. Acquisition was performed using custom LabView routines written for this application. All data processing, including image processing, was performed using Matlab software.

Image acquisition was performed using a National Instruments PCI-1405 image acquisition card. For automation, all acquisition was performed using the same computer, and LabView software. Acquisition was sequential, beginning with signal generation, followed by a pause for transients to settle out. Then data acquisition, and finally image acquisition were performed, before advancing to the next frequency in the sine dwell measurement. Camera gain and shutter duration configuration were performed using Windows based HyperTerminal software, which communicated with the camera through the computer COM port.

Signal generation was required for both excitation of the speaker signal and the camera triggering. Output of these signals was performed using the analog output feature of the DAQ card, allowing the signals to be generated in software. The velocity excitation signal was further amplified prior to reaching the speaker. The speaker excitation signal was a simple sine wave, with a fixed frequency and an amplitude determined as a function of frequency as described in Section 2.7. The camera triggering signal was a square wave with a 50% duty cycle, operated from 0-5V, and held at a phase relative to

the speaker sine wave. This phase was varied to result in the different phase images as described in Section 2.6.1. A sketch of the data acquisition system including signal generation is found in Figure 2.30.

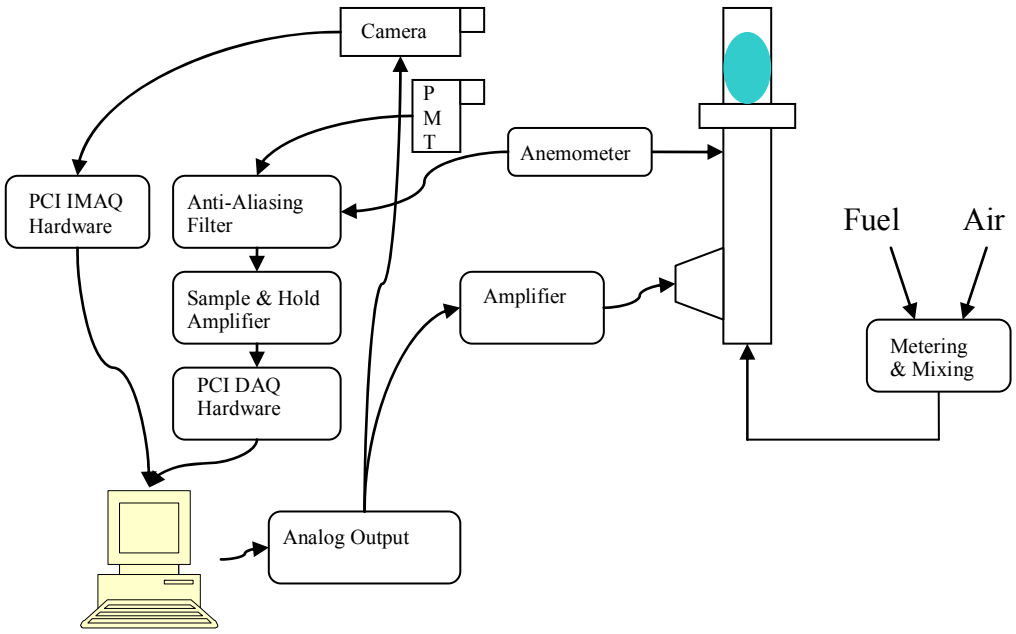

Figure 2.30 - Sketch of the data acquisition setup used in this study.

2.11 Dynamic System Theory and Prediction of Instabilities

For the purposes of making stability predictions using a linear closed-loop model similar to those detailed in Section 1.4.2, it is necessary to choose a stability criterion. Martin [33] gives a detailed description of the various limitations of Laplace domain analysis, the Nyquist stability criterion and the Bode (Barkhausen) stability criterion. As Martin notes, complications of actually identifying the Laplace domain behavior of the transfer functions, particularly for experimental data, are significant. He further notes that use of the Nyquist criterion is hindered by difficulty of automated implementation and interpretation. Thus while the Bode criterion is inferior in that it only represents a necessary, but not sufficient, condition for instability, its ease of implementation makes it the preferable choice. Additionally, as Martin showed, the results obtained from this criterion were reasonably accurate when compared against experimental measurements.

To implement this criterion, it is first necessary to ascertain the open-loop transfer function for the closed-loop feedback model. If we consider a disturbance of velocity on the input, we may visualize this model as shown in Figure 2.31. Analysis of this model results in a total transfer function for the feedback system given in Equation 28.

$$\frac{q'}{u'} = \frac{\Im}{1 - \Im\alpha} \tag{28}$$

The term in the denominator $\Im\alpha$ (the product of flame and acoustic transfer functions) represents the open-loop transfer function of the model, and is what must be considered when applying the Bode criterion.

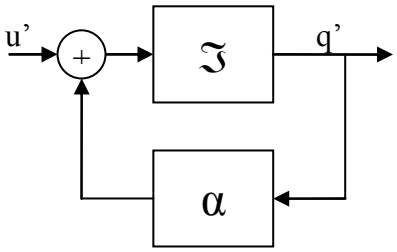

Figure 2.31 - Closed-loop model used for prediction of instabilities in this study.

As stated, application of the Bode criterion requires analysis of the open-loop transfer function (OLTF). For positive feedback, as we have here, frequencies where the OLTF is in phase must be identified (that is, multiples of 360°, both positive and negative, including 0°). At these frequencies, the magnitude of the OLTF is tested for values greater than unity, representing amplification of the response. Any frequency which meets both of these tests is a candidate for instability. This criterion, as is obvious from this description, exclusively relies on the phase for identification of instability frequencies, so measurement of the open-loop transfer function phase behavior is very important to accurate predictions. In applying this condition to the practically measured transfer function, phase crossings were identified as all points with a phase +/- 20° of the actual crossing to eliminate the possibility of scatter in the experimental transfer functions obscuring a potential unstable point.

It should be noted that this criterion is only a binary test for linear stability. Thus, once instability is actually encountered, nonlinearities may change the actual character of the system behavior. An example would be harmonics of the fundamental frequency appearing in an experimental measurement of instability, but which a linear instability prediction would never identify. Additionally, at points where multiple frequencies are identified as potential instabilities, a single frequency may dominate practically due to nonlinear effects. Further discussion of these effects and their impact on instability predictions is most sensible to include in further depth alongside presentation of the results, which may be found in Section 3.9.

Chapter 3 – Results and Discussion

The results of the measurements made are presented in order relative to their pertinence to Phase 1 or Phase 2 of the study. In the case of measurements with pertinence to both Phases, they are included with the data from Phase 1.

3.1 Steady Flame Size Measurements

Measurements of the spatial distribution of the flame heat release rate were made according to the techniques described in Section 2.6. These results were first measured in a steady sense so as to provide a basis for the subsequent dynamic measurements. Several different measures of the flame spatial distribution were used in this characterization: the length and width of the flame, the offset to the center of heat release rate and the volume of the reaction region. Further details of the nature of each of these measurements may be found in Section 2.6.5

In general, the flame was observed to become longer at leaner equivalence ratios. This is intuitive considering that for lean combustion, flame speed decreases with reduced equivalence ratio, indicative of a reduction in reaction rate. Thus, for leaner equivalence ratio, a longer time is required for reaction to reach completion, and given a fixed velocity, longer distances spanned by the reaction region during this time. Likewise, for a fixed equivalence ratio, increases in the overall flow rate were observed to increase the flame size. Again this behavior is expected given that for a constant reaction rate, increased flow velocities would result in a longer distance required for complete combustion to occur.

A plot showing the steady flame volume as a function of flow rate and equivalence ratio is given in Figure 3.1. These results reflect the qualitative description of the behavior described above. Note that the maximum volumes that could be measured were limited by extension of the flame beyond the top of the quartz tube, resulting in an obstructed view. This results in the low equivalence ratio deviation from the otherwise consistent curves shown in the figure for high flow rates.

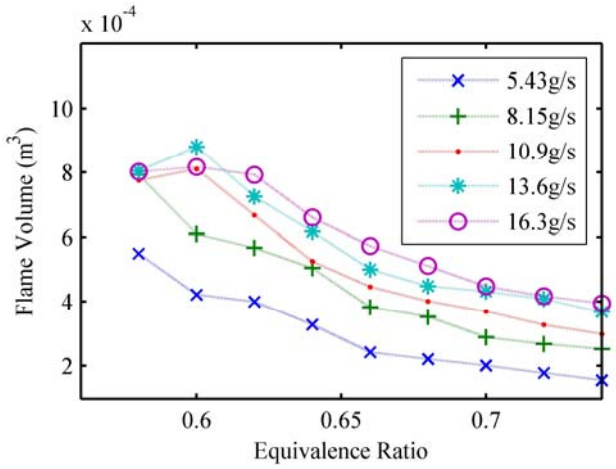

Figure 3.1 - Plot of measured flame volume vs. equivalence ratio, flow rates in g/s.

The flame length and offset exhibited similar trends, which is unsurprising given that length and offset were each observed to have a linear relationship with the flame volume as depicted in Figure 3.2 and Figure 3.3 respectively. As mentioned with regard to the flame volume, the flame extends beyond the physical combustor, and thus the view of the camera, at the leanest conditions resulting in deviation from the perfect linear relationship expected.

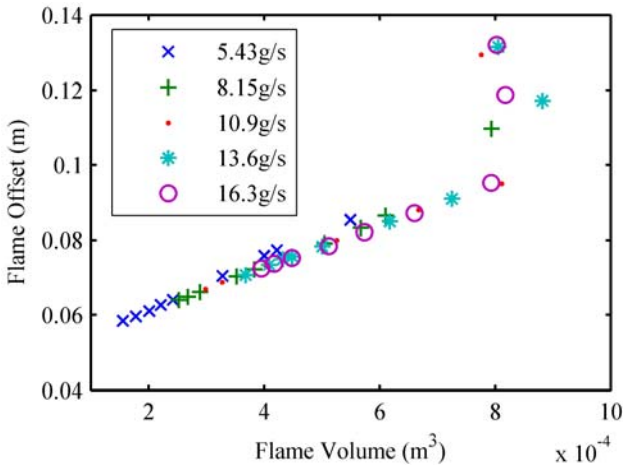

Figure 3.2 - Plot of the offset to the center of flame heat release rate as a function of the flame volume.

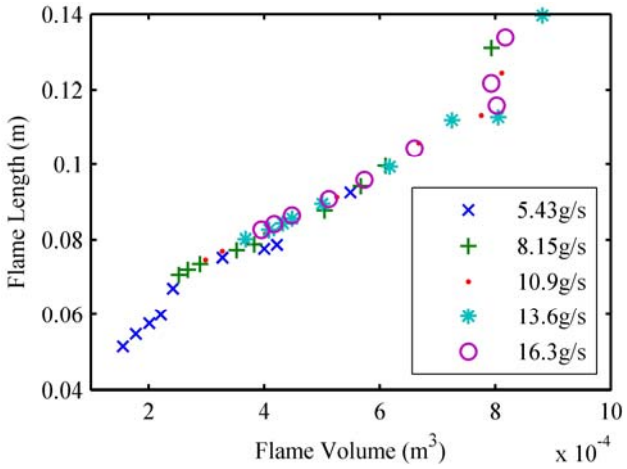

Figure 3.3 - Plot of the flame length as a function of the flame volume.

Considering the linear relationships between these quantities, it seems that analysis of the relationship between the flame length and width may be revealing. The flame length and width were compared with changes in the flame volume, and is shown in Figure 3.4. While the length varies substantially, the width varies very little across operating conditions. The steady flame volume thus depends primarily on the elongation and contraction in the axial direction with changes in operating condition

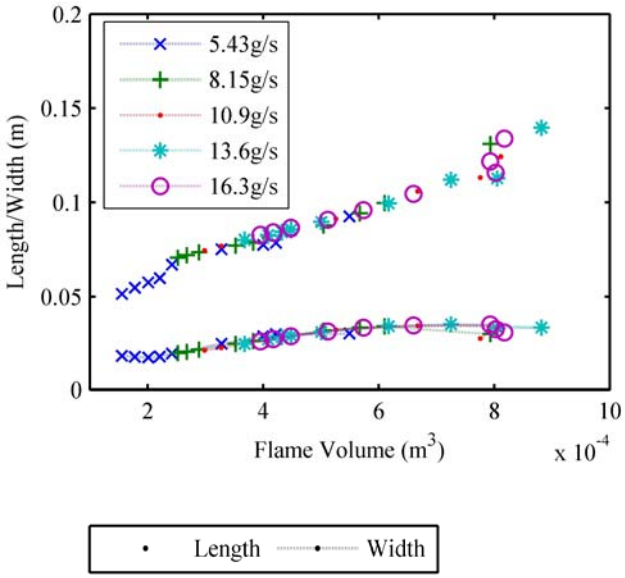

Figure 3.4 - Plot of the flame length and width as a function of the flame volume. The dashed line with markers represents the width, while the markers (upper results) represent the length.

3.2 Dynamic Flame Response to Velocity Perturbations

To continue the analysis from static to dynamic measurements, the response of the flame to velocity perturbations was measured, using both the spatial metrics and the heat release rate (HRR). As has been mentioned previously, the flame HRR response has been observed to behave similarly to a low-pass filter. Prior to any quantitative analysis of the transfer functions resulting from the processed images, we will begin with a qualitative description of the phase locked flame images. A series of images representing the flame CH* chemiluminescence is shown in Figure 3.5 for 4 separate frequencies of excitation. If the differences between phases prove too difficult to ascertain, readers are encouraged to create an animation by placing the individual frames in sequence.

As visible in Figure 3.5, for the case of the 100 Hz excitation, the flame is observed to exhibit significant axial oscillation. As the frequency is increased to 200 Hz, the oscillation at the flame tip is reduced, but the appearance of a translating region of high reaction rate is visible passing through the flame in a lengthwise direction. This is thought to be indicative of convective flow structure interaction with the flame, as described in literature. Advancing to 300 Hz, the lengthwise oscillation is barely visible, but the coherent flow structure interactions are still present, and occur in quicker succession. This is expected for structures experiencing convection along with the mean flow. Finally, for the case of 400 Hz excitation, very little coherent response is visible. Qualitatively this response mimics a low-pass filter, and reflects the idea suggested in the literature [10, 13, 15], that flame response is related to interactions between the flame surface and coherent flow structures.

In order to better visualize this phenomenon, a close-up view of the left half of the flame responding to 220 Hz excitations is shown in Figure 3.6. In this figure, additional coloration highlights the highest intensity regions in the deconvoluted images. With increasing phase, a pocket of high intensity is clearly visible moving along the length of the flame and merging with the high intensity region near the wall, as described above.

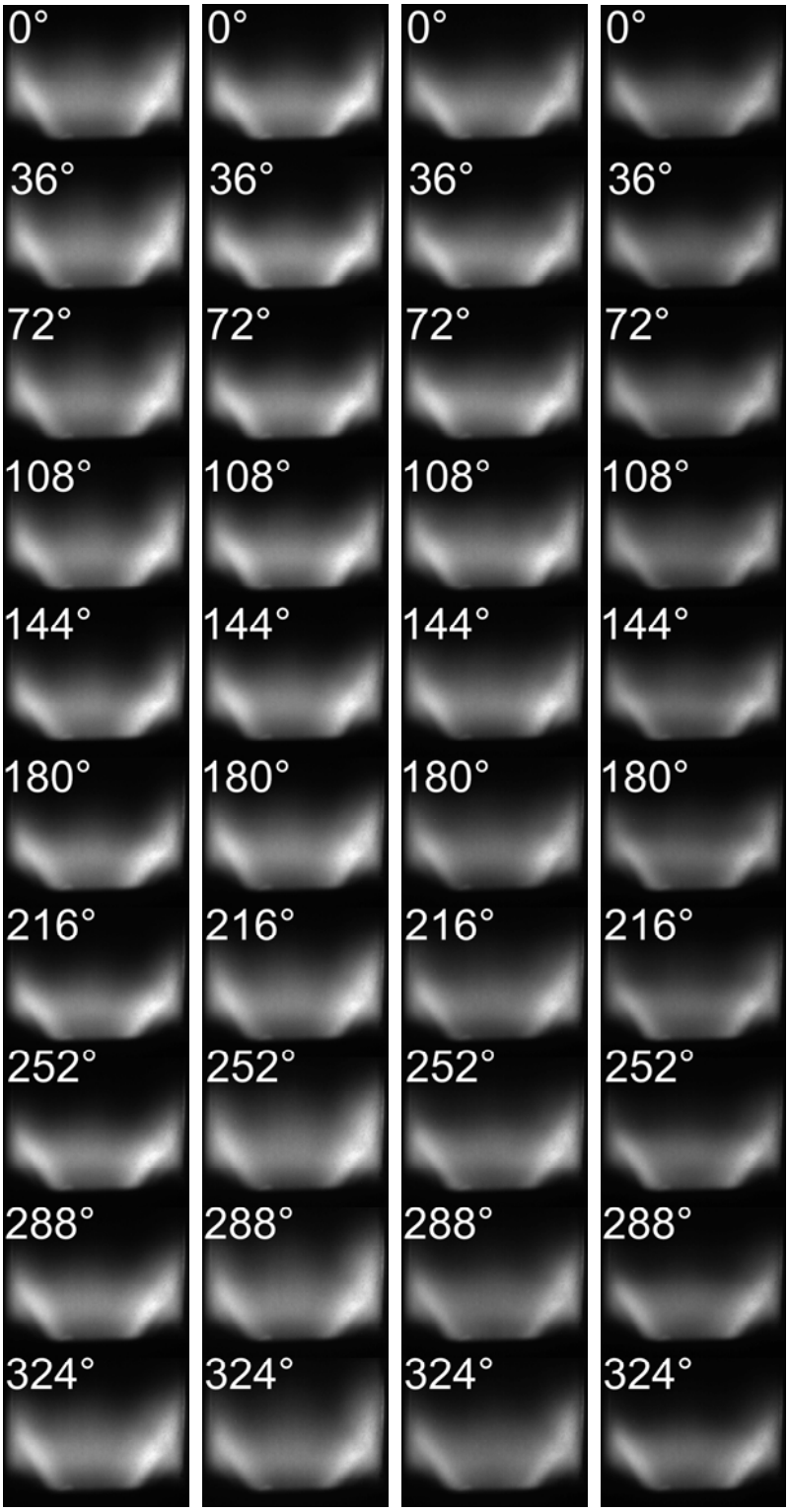

Figure 3.5 - Images of the flame as it responds to perturbations at frequencies of 100, 200, 300 and 400 Hz (L to R). These images have not had the deconvolution processing applied.

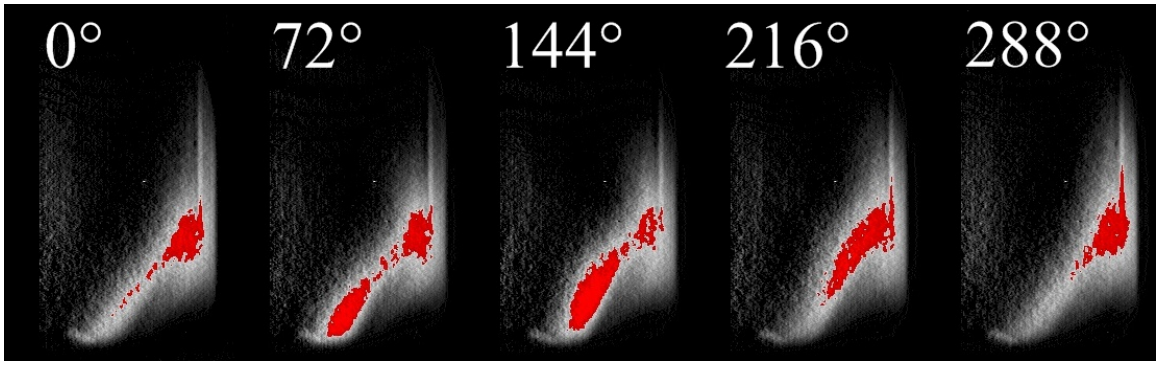

Figure 3.6 - Close-up on deconvoluted images left half of the flame excited at 220Hz showing the movement of a coherent structure through the flame. The colored threshold shows the region(s) of highest intensity.

The images of the flame were subsequently deconvoluted and thresholded, resulting in a cross section of the flame reaction region, which was then volumetrically integrated to result in the flame volume at each phase. The volume calculated from each image is plotted in Figure 3.7 along with the best fit sine wave, necessary for the frequency domain analysis inherent to calculation of the transfer function. Note that the magnitudes in this figure are not indicative of the actual transfer function magnitude, due to the lack of normalization by the velocity. Rather it is merely meant to illustrate the process used for quantification of the data.

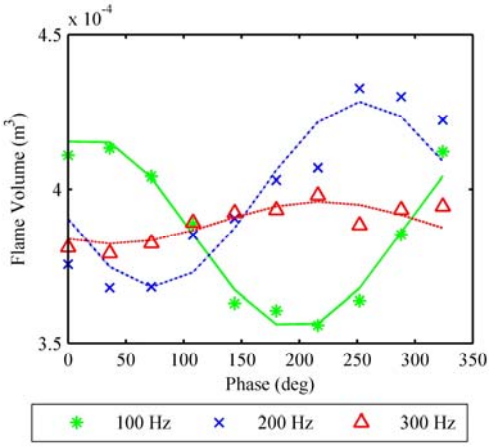

Figure 3.7 - Response of the flame volume over one cycle of excitation at several frequencies. The lines are the sine waves which are best fit to the data points.

Another set of example time series data showing the relative shapes and phases of the excitation and the response is in Figure 3.8 through Figure 3.11. As with Figure 3.7, the magnitudes of these signals are not meaningful as they have been normalized. Recall that the image measurements in these figures are averaged, and thus do not actually reflect the instantaneous behavior. Rather it reflects the phase averaged behavior relative to the excitation signal. It is evident from these figures that the spatial measures are, in general, in phase with the heat release rate signal. The phase of the PMT and hotwire signals relative to the speaker excitation however, varies significantly. Of further note is that it can be seen that the response of the instantaneous flame heat release rate to high frequency excitations is not visible in a time trace. The response of the spatial measures remains visible, as phase averaging has already been performed. To further ascertain the actual character of the response of each characteristic relative to the excitation magnitude, it becomes necessary to consider it through in the actual flame transfer function, as discussed below.

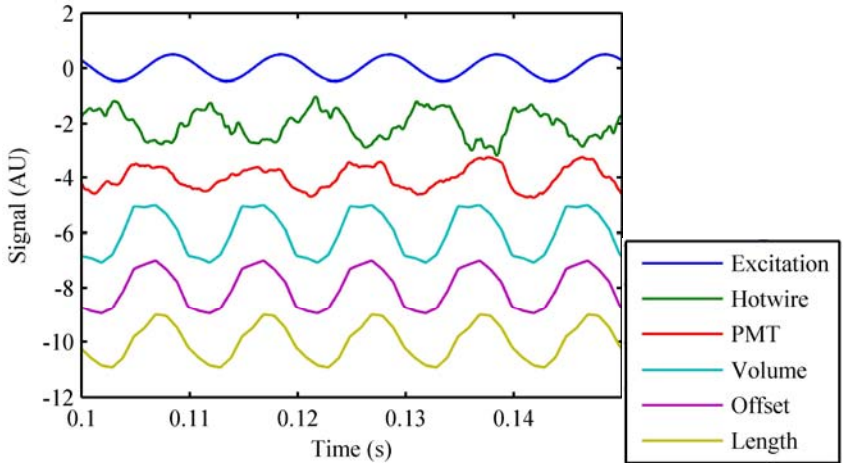

Figure 3.8 - Time trace of various measures of the flame response for a 100 Hz excitation. Signals are from top to bottom: the speaker excitation, hotwire, PMT, flame volume, offset, flame length.

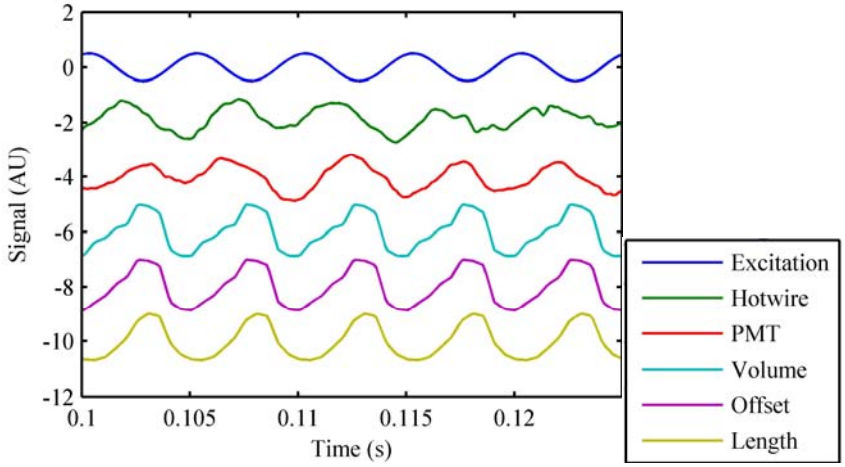

Figure 3.9 - **Time trace of various measures of the flame response for a 200 Hz excitation. Signals are from top to bottom: the speaker excitation, hotwire, PMT, flame volume, offset, flame length.**

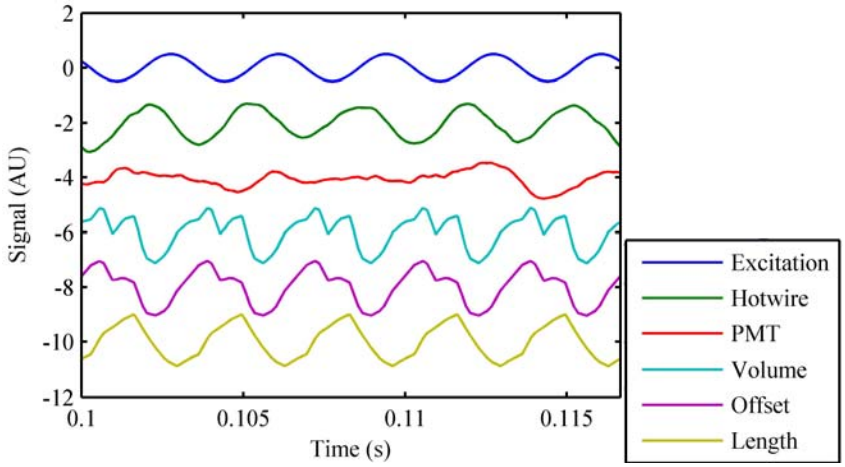

Figure 3.10 - **Time trace of various measures of the flame response for a 300 Hz excitation. Signals are from top to bottom: the speaker excitation, hotwire, PMT, flame volume, offset, flame length.**

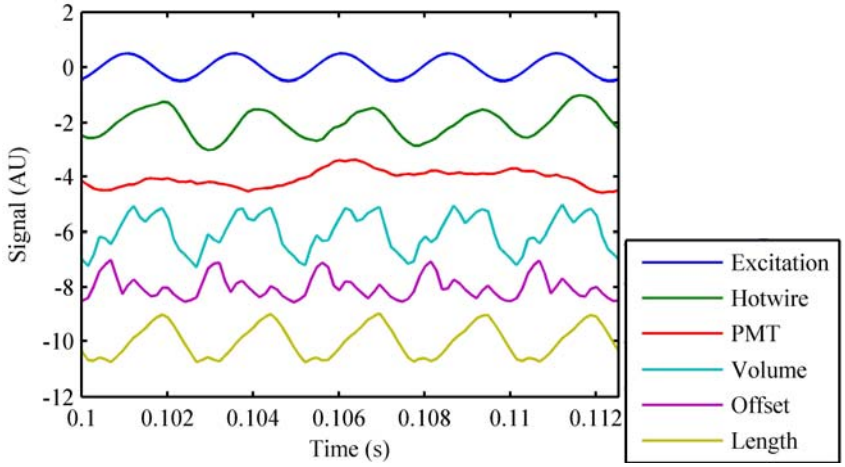

Figure 3.11 - Time trace of various measures of the flame response for a 400 Hz excitation. Signals are from top to bottom: the speaker excitation, hotwire, PMT, flame volume, offset, flame length.

The volume and offset were each applied as a measurement of the output of the flame transfer function, and compared these results to those of the flame heat release rate. Additionally, though the intensity measured from the images was an inappropriate measure of the mean heat release due to normalization and variation in the camera gain, global image intensity was applied as a dynamic measure to test the viability of using the images for the measurement of flame dynamics. Results for the flame transfer function with normalized magnitude for these outputs found that the dynamics are nearly identical regardless of the output chosen, and each match the classic global HRR transfer function, with flame length providing the least effective fit. Additionally, the intensity dynamics from the images matched the dynamics of the global HRR very well. A transfer function resulting from each of these measures as the output is plotted in Figure 3.12. Each transfer function retains the low-pass filter characteristic with a bandwidth relatively close to the original heat release rate transfer function.

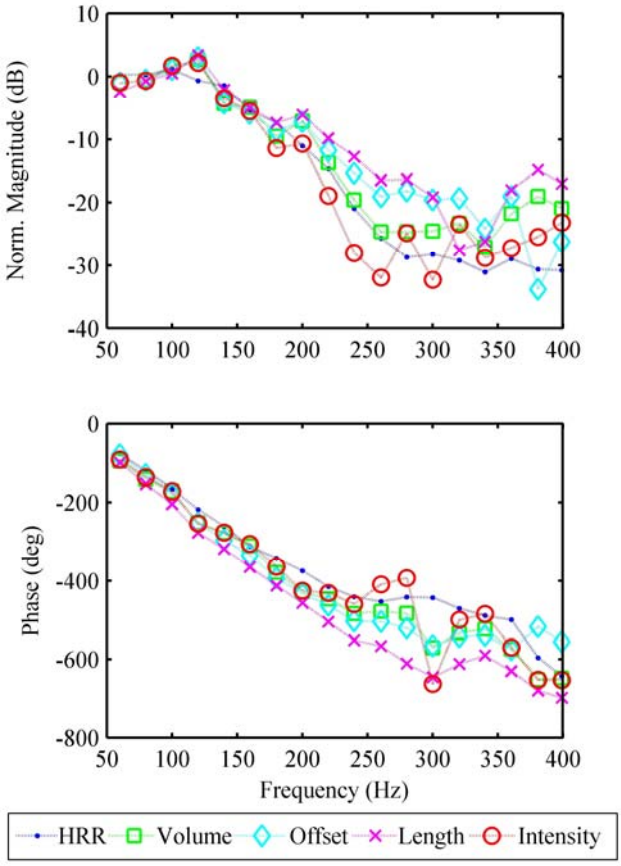

Figure 3.12 - Dynamics of the heat release rate compared against the dynamics of several measured quantities from the flame images. Test condition is natural gas at an equivalence ratio of Φ=0.68 with a flow rate of 13.6 g/s.

A second example of the comparison of these measures for a different operating condition is provided in Figure 3.13. Again, offset, volume and the image intensity all agree extremely well with the HRR dynamics. Flame length again presents the least accurate fit for this condition.

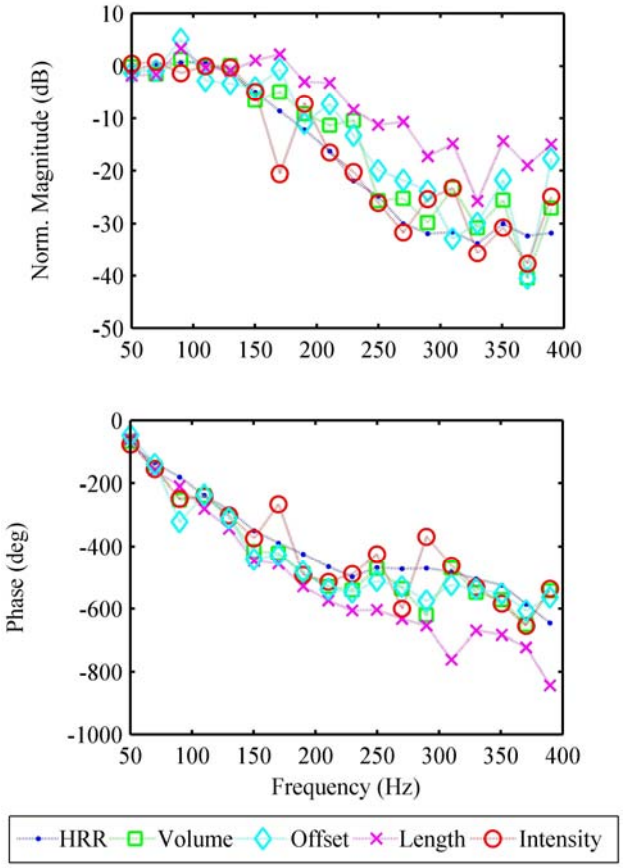

Figure 3.13 - Dynamics of the heat release rate compared against the dynamics of several measured quantities from the flame images. Test condition is natural gas at an equivalence ratio of Φ=0.65 with a flow rate of 13.6 g/s.

A test case was also conducted, using propane as the fuel for comparative purposes. The results of this case are presented in Figure 3.14, and continue to reflect the same trend already described.

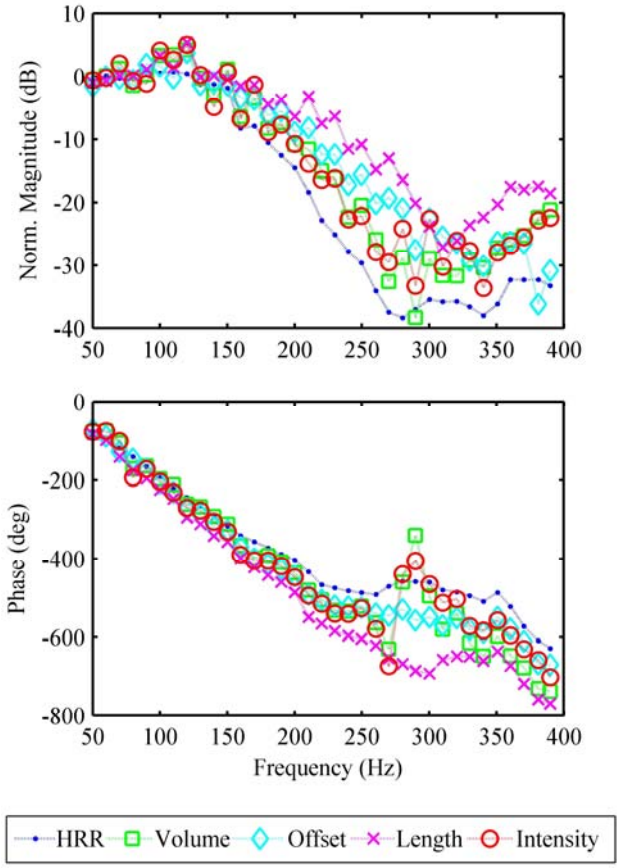

Figure 3.14 - Dynamics of the heat release rate compared against the dynamics of several measured quantities from the flame images. Test condition is propane at an equivalence ratio of Φ=0.63 with a flow rate of 13.6 g/s.

Though these figures provide samples of the flame dynamic measurements, it would be difficult to compare the volume and HRR transfer functions as a function of operating condition on a single plot of this type due to the abundance of data. To provide a cleaner picture of the data over a wider range of operating condition, the HRR transfer function result was subtracted from the volume transfer function. Thus, a perfect match would be represented by a horizontal line in magnitude at 0dB and, likewise, a horizontal line at zero degrees for phase. This description of the response is mathematically identical to calculation of the transfer function between the volume and the heat release rate, but is somewhat easier to conceptualize. The results of this calculation are presented for all natural gas operating conditions in Figure 3.15, as a function of frequency

nondimensionalized by the steady offset and velocity (Strouhal number). The use of Strouhal number for nondimensional frequency will be discussed further in Section 3.4. As is evident, these data indicate that overall the volume dynamics mimic the heat release rate dynamics quite closely. This generalizes the trend observed in the previous figures. In Figure 3.16, the same results are shown for the flame offset as the spatial measure. Again, the offset dynamics serve as an excellent predictor of the heat release rate dynamics. The vertical dotted lines in those figures is the Strouhal number at the bandwidth of the response, which is shown since the phase results in particular exhibit some significant deviation beyond that point, due to reductions in the coherence.

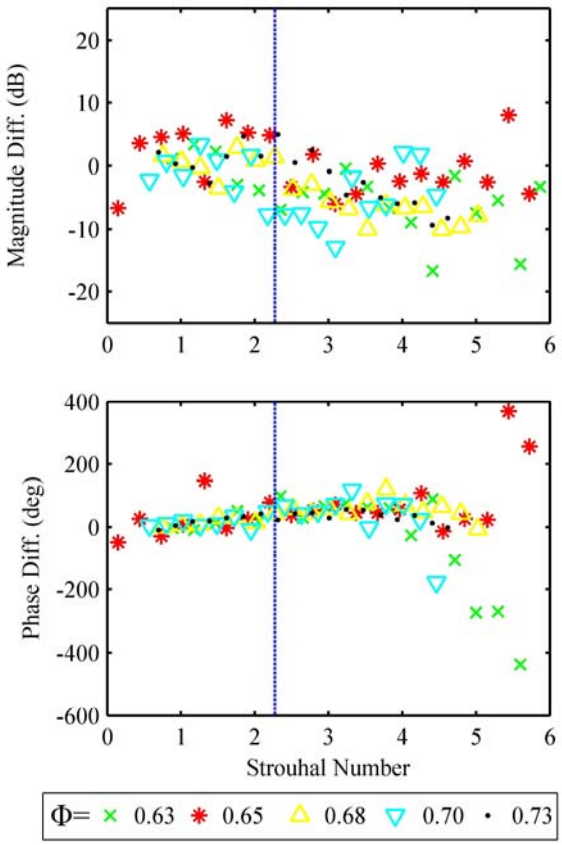

Figure 3.15 - Difference between volume dynamics and heat release dynamics for all test conditions for natural gas.

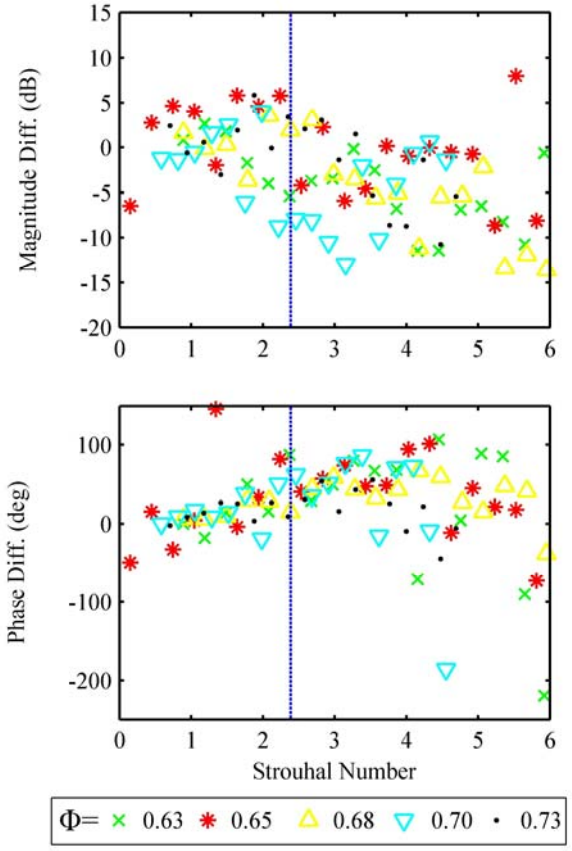

Figure 3.16 - Difference between offset dynamics and heat release dynamics at a variety of equivalence ratio conditions for natural gas.

3.3 Discussion of the Spatial Dynamics Results

The results of the flame volume response provide an analogy to the physical behavior highlighted when using flame sheet models, which were discussed in section 1.4.1. Flame sheet models are based on the idea that the flame may be treated as a thin sheet with a uniform heat release per unit surface area. This sheet experiences oscillations in the total heat release rate by interactions with coherent flow structures, which may be linked to an experimentally observed mechanism. These flame structures are observed to cause fluctuations in the surface area, and thus the flame sheet heat release rate [10, 29]. Similar to this, the behavior of the flame volume described in this study reflects a global growth of the flame reaction region coherent with the excitation. The near identical results for the heat release rate and volume transfer functions suggest a similar

proportionality between the volume of the flame and the heat release rate. The flow structures described qualitatively from the flame images may be thought of as being convected by the mean flow through the flame. These cause a local enlargement of the time averaged reaction region as they stretch the flame surface. The matching of the transfer functions indicates that a direct proportionality is present between these volume enlargements and the global heat release rate. Such a convection based explanation remains consistent with the observed linear phase trend, indicative of time delay, as a delay would be expected between the creation of a flow structure and its interaction with the flame. This description of the response of the flame to velocity perturbations lends a degree of validation to the use of flame sheet models in the prediction of flame dynamics.

Increasing frequency of excitation results in a reduction in the effect of the volume response to excitations (the low-pass filter characteristic previously described). To further analyze this effect, let us consider the dynamic response of the flame offset. The offset of the center of the reaction region, as with the volume, exhibits dynamics identical to those of the flame heat release rate. A dynamic response of the flame offset represents upstream and downstream shifts in the mean position of the reaction. Conceptually, this could be the result of two possible effects. First is a uniform elongation/contraction of the flame along the flow direction, which would result in a shift of the mean position of reaction. Second, even if the flame were to remain completely constant in length, the presence of local high intensity regions could create a shift in the mean. As indicated by the transfer function magnitude, the amplitude of this shift decreases with increasing frequency of excitation. Since we may consider time and position to be linked due to convection, an explanation for this becomes quickly apparent. If we assume the interaction mechanism found in literature, the convection of structures through the flame appears to be the source of coupling between the velocity and the flame. If we consider that the structures must decrease in size corresponding to the period of the excitation, it becomes clear that as frequency increases, the intensity of the response will decrease simply due to the reduced size of the coherent structures, resulting in a reduction in the magnitude of localized fluctuations. This corresponds to a reduction in the shift in the flame offset.

Additionally, the reductions in bandwidth with longer steady flame length may be explained by the reduction in heat release per unit length. For a fixed frequency of excitation (and thus a fixed size of the coherent structures), a longer flame with the same global heat release will have a reduced response, since the structures interact only locally. This explanation of the dynamics is compatible with both the bandwidth of both the offset and volume transfer functions. This provides a potential physical explanation for the observed behavior relative to operating condition. Finally, the recognition that the spatial characteristic transfer function, measured in a phase averaged sense, matches the heat release rate transfer function provides important physical justification for recent use of ensemble averaging in modeling efforts [54].

3.4 Analysis of Heat Release Rate Dynamics Through Nondimensionalization

Bearing in mind that the volume, offset and heat release dynamics are all identical, measurements of the flame heat release rate dynamics were made at a wider variety of operating conditions. Due to limitations in the data acquisition scheme for the spatially resolved size dynamics, it was convenient to consider only the heat release rate in these measurements for reliability and the duration of the test required. However, since these measurements have proven to be identical, this is not limiting. Steady spatial images of the flame were still acquired for these tests as part of the nondimensional analysis.

Recall, briefly, that the ultimate goal of flame transfer function measurements conducted in this study is to provide a useful application through closed-loop model stability predictions. As stated in Section 2.11, in a linear systems theory realization of the combustor, the product of the flame and acoustic transfer function (the open-loop transfer function) is tested for in phase conditions with amplifying gain. Changes in phase behavior will result in changes in instability frequency. Analysis of the combined magnitude reveals points at which instability is even a possibility. Since the acoustics are assumed to be constant with operating condition, we may consider changes in the behavior of the flame transfer function to provide insight into the instability behavior of the system.

Let us first consider the flame dynamics by looking at the overall flame transfer function. As has been noted, the flame behaves as a low-pass filter. Several investigators [29, 32] have previously observed that the flame dynamics may be nondimensionalized in frequency using a convective timescale based on the steady flame offset and the mean velocity at the measurement location, resulting in Strouhal number as shown in Equation 29.

$$St = \frac{f x_o}{\bar{u}} = f \tau_{conv} \tag{29}$$

By using an offset from the transformed hotwire measurement location, this nondimensionalization was successful for data measurement here over a variety of operating conditions. For flow rates ranging from 15 to 30 SCFM (8.15-16.3 g/s) and equivalence ratios Φ=0.6 to 0.7, replacement of frequency by Strouhal number results in a satisfying collapse of the magnitude normalized data. Effects of variation in the low-frequency gain will be considered later. The nondimensionalization of the data for the flame transfer functions measured is shown in Figure 3.17. The transformation is successful for all flow rates and equivalence ratios considered. The stated low-pass filter behavior and linear phase are quite evident in this data.

In order to apply the flame transfer function to a closed-loop model, it would be useful to have a nondimensional “prototype” flame transfer function that can be used for any operating condition that may be encountered in the combustor. Due to the low-pass behavior of the response, the most important characteristics to identify on a globally applicable basis are the bandwidth, the phase behavior and the low frequency gain. We will analyze the behavior of these characteristics individually.

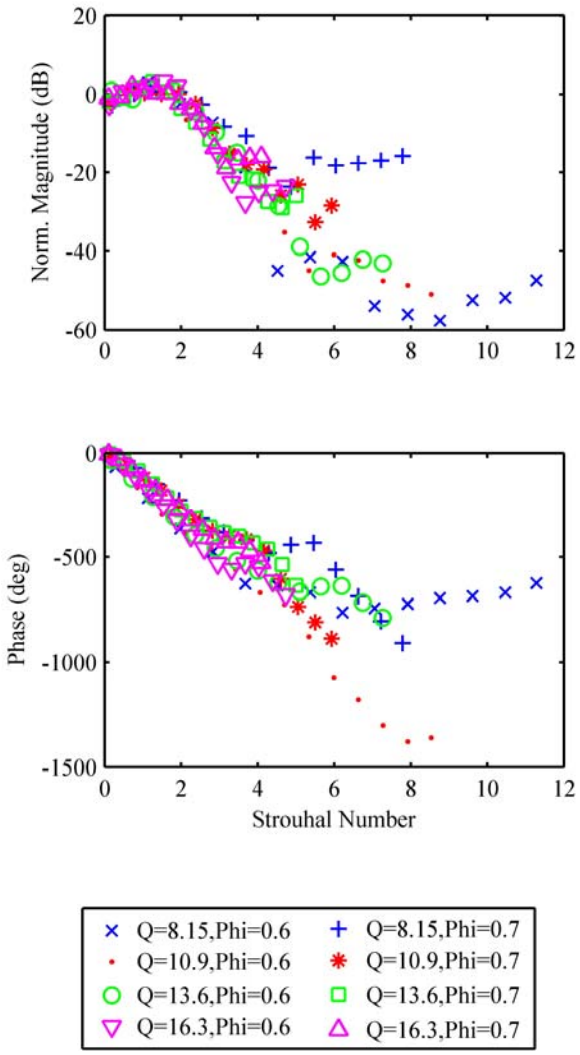

Figure 3.17 – Frequency nondimensionalization applied to the heat release rate transfer function using Strouhal number based on steady offset and mean velocity

3.4.1 Characterization of the Transfer Function Bandwidth

The cutoff frequency (bandwidth) of the heat release rate transfer function has been observed to decrease with increasing flame size. The bandwidth was quantified by measuring an 8dB drop from the low frequency mean (mean of the first 5 values) of the transfer function. Measuring bandwidth in this manner results in a linear relationship between bandwidth and both inverse flame offset and volume, as shown for a single flow rate in Figure 3.18. The cutoff frequency varied between 150 and 210 Hz. Cutoff

frequencies expected from chemical time scales for these operating conditions would be expected to occur at frequencies greater than 1000 Hz [33].

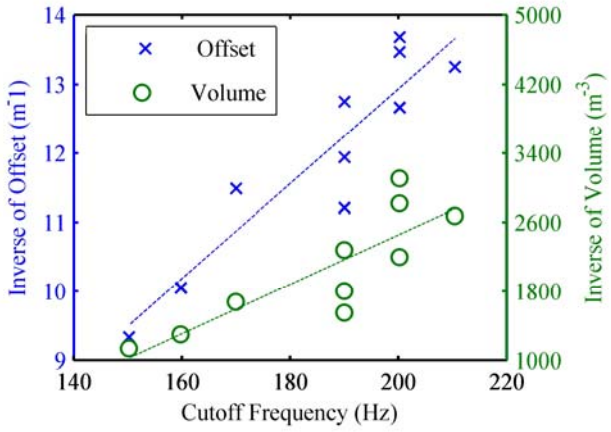

Figure 3.18 - Plot of transfer function cutoff frequency (based on 8 dB drop) as it relates to both flame volume and offset.

The time scales associated with the observed cutoff frequencies are on the order of milliseconds (6.67ms – 4.76ms). Shorter time scales are significant in that it suggests a slower phenomenon. The convective mechanism proposed in Section 3.3 agrees with this observation. Additionally, this linear relationship agrees with the noted link between the transfer function bandwidth and the Strouhal number. Since both frequency and offset appear in the numerator of the Strouhal number, for a constant Strouhal number and flow rate (velocity), frequency varies as inverse size, exactly as observed here.

For the case of cutoff frequency variation with respect to changes in flow rate, we must consider the idea that bandwidth is nominally constant with respect to Strouhal number, as seen in Equation 30.

$$St_c = \frac{f_c x_o}{\bar{u}} = C \tag{30}$$

Substituting for mass flow rate, a relationship for cutoff frequency is obtained as follows:

$$f_c = \frac{\bar{u} St_c}{x_o} = \frac{\dot{m} St_c}{\bar{\rho} \bar{A} x_o} \tag{31}$$

Both the numerator and denominator increase with increases in the mass flow rate (see offset behavior in Figure 3.2), so the relative change in the cutoff frequency depends on whether the growth rate of the denominator with respect to mass flow rate is greater or less than unity. That is, if the velocity increases at a higher rate than the offset with increasing mass flow rate, then one would expect the cutoff frequency to increase, and vice versa. The actual change of cutoff frequency relative to mass flow rate as measured from the data is presented in Figure 3.19, from which it is evident that the competing effect of changing offset and velocity will result in a net increase in cutoff frequency with increasing mass flow. Thus we may also infer that velocity increases at a greater rate than offset with respect to mass flow.

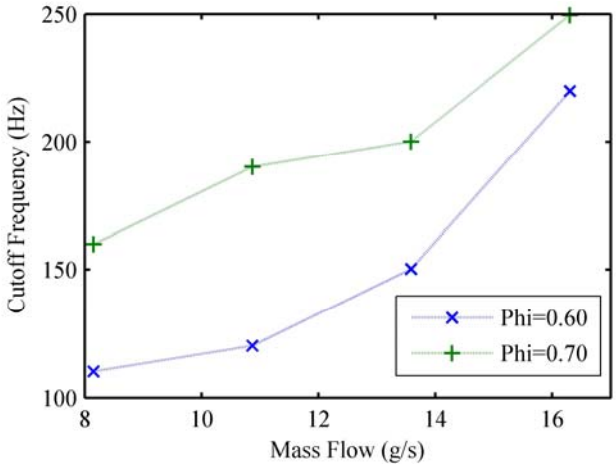

Figure 3.19 - Variation of cutoff frequency with respect to mean mass flow rate.

3.4.2 Characteristics of the Time Delay

Linear phase observed in the transfer function is almost always indicative of time delay. The phase observed for the flame transfer functions measured here has a predominantly linear character. Time delay may be conveniently calculated from the slope of this linear phase according to Equation 32, using phase in radians.

$$t_d = \frac{1}{2\pi}\frac{d\varphi}{df} \tag{32}$$

Calculating time delay in this manner, the delay may be seen to have a linear relationship with the flame offset. The steady flame offset is plotted against time delay for a single mean flow rate in Figure 3.20. As with cutoff frequency timescales, the time delay has values in milliseconds, which coincides with convective time scales for this rig. The plotted data may be fit with a linear regression, the slope of which represents the convective velocity associated with this delay, which in this case is computed as 6.31 meters per second. This velocity represents the mean convective velocity experienced by convected structures, and intuitively falls somewhere between the mean velocity at the hotwire measurement port, and the mean velocity at the centerbody (the narrowest downstream flow passage).

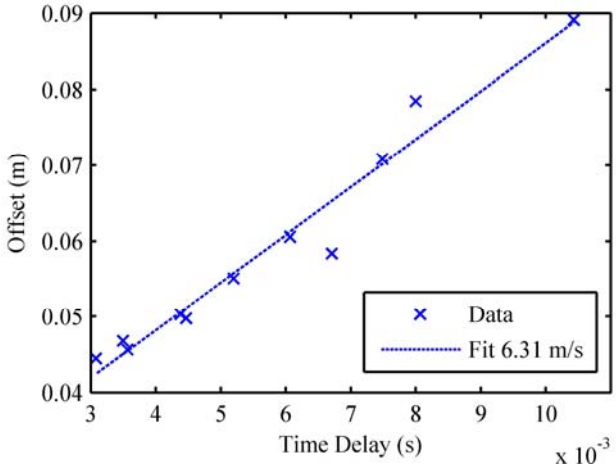

Figure 3.20 - Relationship between offset and phase based time delay. Dashed line represents a best fit based on convection at a constant mean velocity.

While the linear relationship between delay and offset is quite evident from Figure 3.20 for a single flow rate, it remains true that time delay is related to flame and combustor geometry for all flow rates. Similarly to bandwidth, the possibility of nondimensionalization of the flame transfer function discussed above confirms this behavior. In this case, we observe that the slope of the phase with respect to Strouhal number is a constant. That is:

$$\frac{d\varphi}{dSt} = C \tag{33}$$

Substituting the definitions of Strouhal number and time delay, we may see that:

$$\frac{d\varphi}{dSt} = 2\pi \frac{t_d \bar{u}}{x_o} = C \tag{34}$$

In words, time delay divided by the characteristic time associated with flow convection between the measurement location and the center of the flame should result in a constant value. So as flow rate varies, the time delay will vary as a function of both the changing flame size and the mean flow velocity. We may rearrange this as Equation 35.

$$t_d = \frac{x_o}{2\pi\bar{u}} \frac{d\varphi}{dSt} = \frac{\bar{\rho}\bar{A}x_o}{2\pi\dot{m}} \frac{d\varphi}{dSt} \tag{35}$$

This resembles the inverse of Equation 31 with the exception of the 2π factor. By considering the actual measured values of time delay from the transfer function data, we may see the result of these competing effects. In these results, shown in Figure 3.21, it is evident that increasing the mass flow rate for a fixed equivalence ratio results in a net decrease in the delay. This is consistent with Equation 35, considering the already noted observation that the mean velocity must increase at a greater rate relative to mass flow rate than the offset, shown via Equation 31.

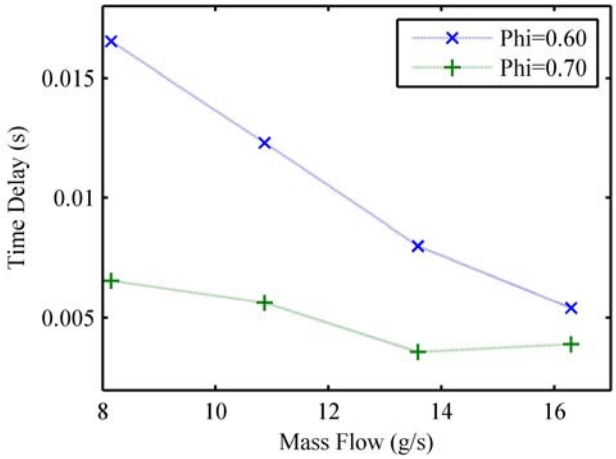

Figure 3.21 - Generalization of relationship between time delay and mean mass flow rate for two equivalence ratios.

3.4.3 Characterization of Flame Transfer Function Low Frequency Gain

The low frequency gain was measured by fixing the excitation frequency at 50 Hz, and varying the equivalence ratio and flow rate. Measurements of the input and output otherwise were made in similar fashion to the overall transfer function, but with the addition of calibration of the hotwire and PMT signals. The calibrated units pertinent to this measurement are kW/(m/s), reflecting the response of the heat release rate in kW to the velocity in m/s. The frequency of 50Hz was chosen as providing a low enough frequency to avoid cutoff frequency effects, but yet a high enough frequency to provide a response unobscured by the DC content. The amplitude of excitation was varied with flow rate such that the response remained linear, as described in Section 2.7. The results in Figure 3.22 show the variation of low frequency gain with operating condition. It is evident that the low frequency gain consistently increases with increasing equivalence ratio. The maximum measured gain was around 15dB with the lowest around 5dB, resulting in a range of 10dB. Remembering that the magnitude reduction due to the low pass filter behavior was 20dB or greater, this change in gain is substantial. The variation observed with flow rate was at most 3dB, much less than the variation observed with equivalence ratio.

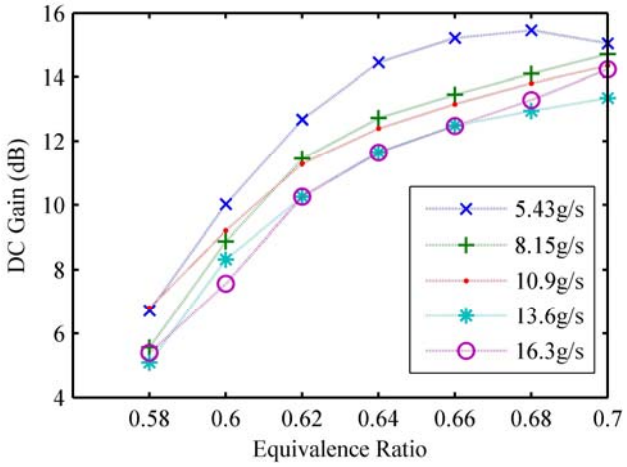

Figure 3.22 - Low frequency gain map for natural gas as a function of operating condition and equivalence ratio.

Additionally, comparison is possible with a theoretical analysis of the low frequency gain, which was performed by Martin [33]. Martin conducted sensitivity analysis of a

simple well stirred reactor model to oscillations in the inlet mass flow, which resulted in gain predictions (in comparable units with the measurements made here) between 0dB and 10dB over the range of operating conditions measured in this study This is on the same order of magnitude as the results measured here. His analysis suggested a similar trend with increasing gain corresponding to increasing equivalence ratio. Additionally, Martin's analysis suggested that the aforementioned equivalence ratio trend was the dominant one, with only a very slight increase in gain with decreasing flow rate predicted. This trend further matches that evident in the measured data here.

3.4.4 Implications of the Flame Transfer Function Characteristics

The bandwidth, DC gain and phase behavior are the most important characteristics in determining system stability on the basis of the closed-loop system model. Recall that the stable/unstable prediction is made according to the Bode criterion. Application of this criterion requires identification of phase crossings of 360° or multiples thereof (including 0°), and requirement that gains at those phase crossings to be greater than unity. While it is impossible to actually assess the system stability in the absence of the acoustic transfer function, since the acoustics are assumed to be constant with respect to operating condition, we may make some inferences about the stability behavior of the system based on changes in the flame transfer function with respect to operating condition.

The simplest effect to consider is that of the low frequency gain. Increases in gain should always lead to an increased possibility for instability, subject to the presence of suitable phase crossings. Since the second test of the Bode criterion requires a unity or greater gain at a phase crossing, increasing the gain represents a wide increase in the potential for amplification to occur. As seen in Figure 3.22, gain increases with increasing equivalence ratio. Increasing the overall flow rate would be expected to result in a very slight reduction in the gain, though only the most borderline of cases would be affected by this variation. Thus the primary impact on stability due to changes in gain is that higher equivalence ratios are more likely to meet the amplification criterion, and thus more likely to be unstable if suitable phase crossings are present.

Similarly to the gain behavior, changes in the transfer function bandwidth impact stability by raising or lowering the gain. In the case of bandwidth however, the effect is not uniform with respect to frequency. Increasing bandwidth effectively raises the gain at higher frequencies by extending the frequency range at which a response occurs. In this way, increasing bandwidth would be expected to lead to a higher incidence of instability for phase crossings that occur near to the cutoff frequency. For the data described above, bandwidth is increased with both increasing equivalence ratio and increasing flow rate. Both of these trends would be expected to increase the possibility of instability for the combustor by extending the range of frequencies over which a potentially amplifying gain is expected. Nominally, we may say that both the magnitude and the bandwidth effects result in the same predicted instability trend, specifically that the potential for instability should be increased with both increasing flow rate and equivalence ratio.

The effect of phase is somewhat more complicated to dissect. Increases in both mass flow rate and equivalence ratio were observed to result in decreases in the amount of delay. Decreasing delay has the effect of reducing the rate of the linear phase roll off in the transfer function, moving phase crossings to higher frequencies. So, both increases in equivalence ratio and mass flow rate have the effect of shifting potentially unstable frequencies higher. This makes further inference of unstable behavior difficult. Ignoring changes in bandwidth and gain, shifts of the phase crossings to lower frequency would cause phase shifts to occur prior to the cutoff frequency of the flame transfer function. However, for the case of the velocity perturbations as measured here, increase in delay coincides with decreases in both low frequency gain and bandwidth, making it difficult to assess the total effect of this change. Consideration of the effect of phase changes on the system stability seems to be impossible in a general sense, requiring knowledge of the acoustic transfer function to understand the total system behavior.

3.5 Further Analysis of Characteristic Lengths Used in the Strouhal Number and Development of a Prototype Flame Transfer Function

Having reached the limit of general analysis of the flame transfer function characteristics, it becomes useful to focus efforts on obtaining a suitable prototype flame transfer function for use in the closed-loop stability prediction efforts. As shown previously in

Section 3.4, the flame transfer function may be nondimensionalized in a satisfying manner using a Strouhal number based on the physical offset from the corrected hotwire measurement location to the center of flame heat release rate. This was seen to provide a useful prototype for the flame transfer function, but there are a few remaining points about the nondimensionalization that bear mentioning.

The nondimensionalization based solely on the physical distance between the corrected hotwire measurement location and the flame center appears successful, and as will be discussed in subsequent sections, provides reasonably successful predictions of the combustor instability. However, it was observed that by using different baselines for the offset value a "tighter" collapse of the transfer function may be achieved independently for the magnitude and the phase. While the magnitude nondimensionalization results are best using the distance stated (Figure 3.17), if the offset is shifted to a different baseline value, corresponding to the dump plane, the phase is observed to collapse better, at the expense of the magnitude response collapse, as seen in Figure 3.23. This offset has a physical representation in the combustor, but it is unclear whether this coincidence with the combustor rapid expansion is physical or surreptitious.

In general, the slight difference between baselines for the magnitude and phase suggests that the underlying timescales associated with these phenomena may be different. In this case, the phase timescale appears to be slightly shorter than that of the magnitude response. Resolution of this slight timescale difference lies outside the scope of this study and is left as a potential area for future investigation.

In addition, it was found that the volume may be used in the Strouhal number by considering a Strouhal number length scale of the effective radius of the flame cross section. This results in a scaling using some approximation of residence time of recirculating flow in the reaction region as the time scale. Such a realization of Strouhal number may be related to well-stirred reactor modeling efforts performed by Martin [33]. This realization is arrived at by approximating the volume of the flame as a toroidal shape with a cross section radius of r_{eff}, as in Equation 36.

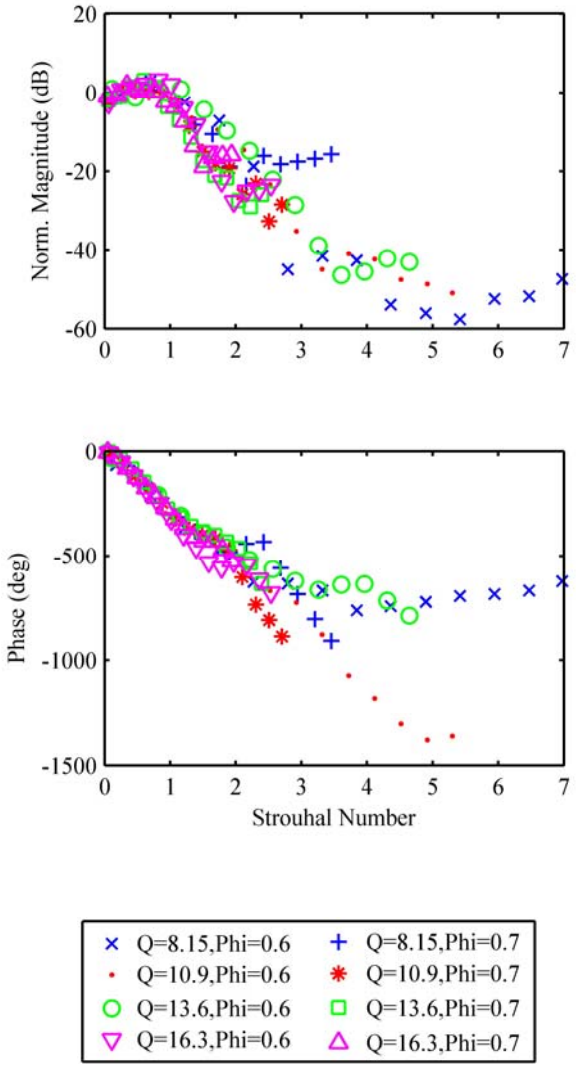

Figure 3.23 - Alternate frequency nondimensionalization of the flame transfer function using the distance between the dump plane and the center of flame heat release rate as the characteristic length in Strouhal number.

$$St = \frac{fr_{eff}}{\bar{u}} = \frac{f\sqrt{V}}{\bar{u}\pi\sqrt{R}} = f\tau_{res} \qquad (36)$$

Using Strouhal number calculated in this manner results in the nondimensionalization shown in Figure 3.24. As with the other realizations of Strouhal number, this provides a satisfactory collapse of the flame transfer function.

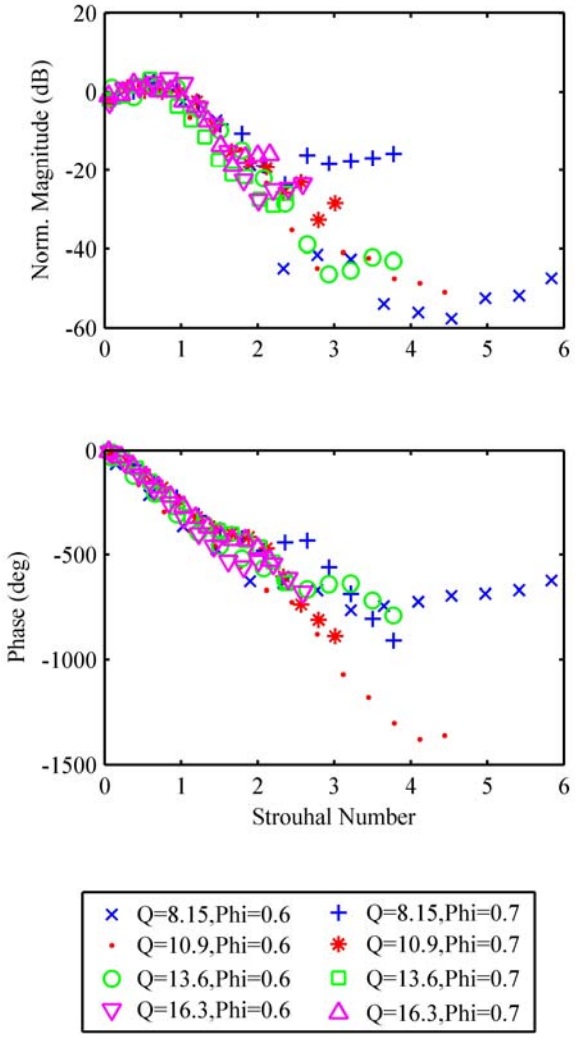

Figure 3.24 – Frequency nondimensionalization of the flame transfer function using an effective cross sectional radius of the flame reaction region based on the square root of flame volume as a characteristic length in the Strouhal Number.

The goal of the flame transfer function analysis appearing in this study is ultimately to provide a suitable prototype flame transfer function for use in the closed-loop model. While it seems reasonable to use either of the relatively successful nondimensional forms for Strouhal number, in order to remain consistent with methods in use in literature, the offset distance between the measurement location and the center of flame heat release rate will be used.

By averaging together all of the non-dimensional flame transfer functions measured, we can arrive at a single prototype for the flame transfer function, which can then be used in closed-loop models. This prototype is shown in Figure 3.25. This prototype transfer function experiences its 8dB bandwidth at a Strouhal number of 2.62, and has a phase slope of negative 125 degrees per unit Strouhal number.

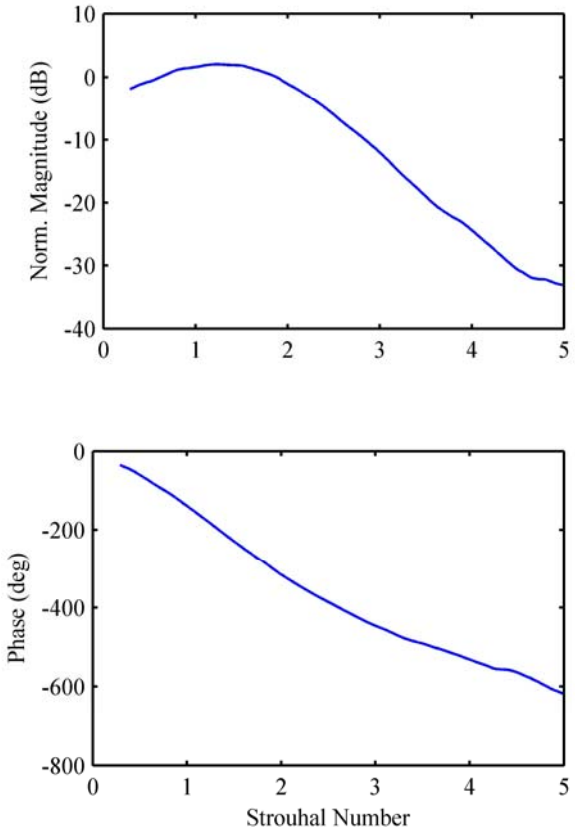

Figure 3.25 - Prototype nondimensional flame transfer function for use in the closed-loop modeling studies. Uses measurement location offset as the characteristic length scale.

This average transfer function was redimensionalized and compared with the actual flame transfer function to test its efficacy as a prototype. The results of this comparison are shown in Figure 3.26. The most significant errors are present in the phase redimensionalization and occur at the leanest equivalence ratio cases. The magnitude, including the gain, is fit relatively well. Thus, this prototype transfer function is suitable

and may be applied in combination with the acoustic transfer function in the closed-loop system model.

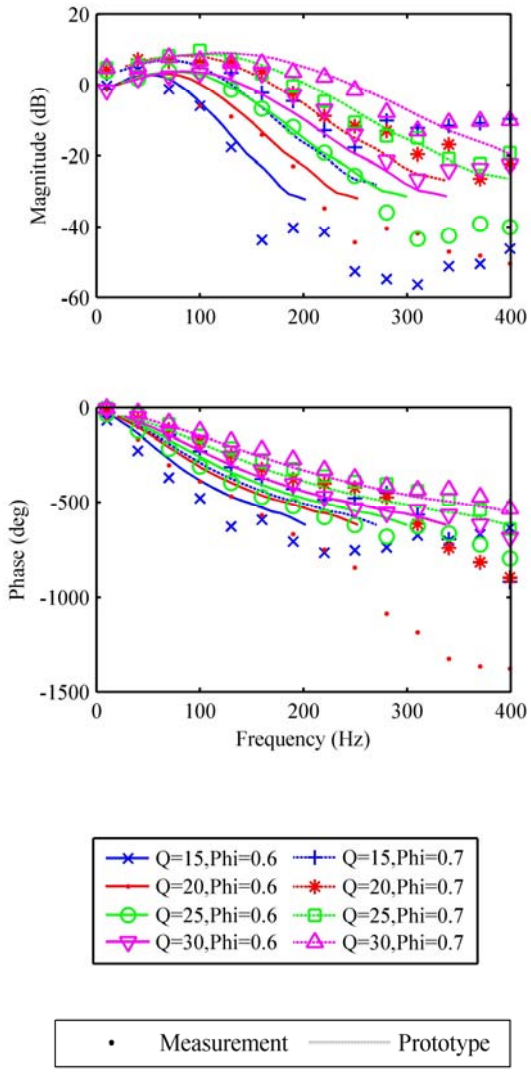

Figure 3.26 - Comparison of measured flame transfer function and calculated equivalent using the prototype flame transfer function. Lines are prototype, markers are measurements.

3.6 Acoustic Transfer Function

The acoustic transfer function in the combustor was measured according to a technique thoroughly tested and validated by Black [3] and described previously in Section 2.8. The acoustic transfer function measured according to this technique is presented here in

Figure 3.27. The coherence of this measurement is only strong between around 50Hz and 200Hz, as is evident from both the smoothness of the transfer function itself, and the actual plot of the coherence in Figure 3.28. This indicates that the velocity and heat release rate are not strongly correlated below 50Hz and above 200Hz, and thus, measurements of the transfer function at these frequencies are not completely reliable. The actual instabilities observed in the combustor all occurred within this range, so no practical limitations are imposed by this. Additionally, it is likely that the reason for the strong coherence in this frequency range is due to the more significant gain associated with the input and response. This would likely be true over the pertinent unstable range even in combustors with a different acoustic transfer function, maintaining the usefulness of this technique.

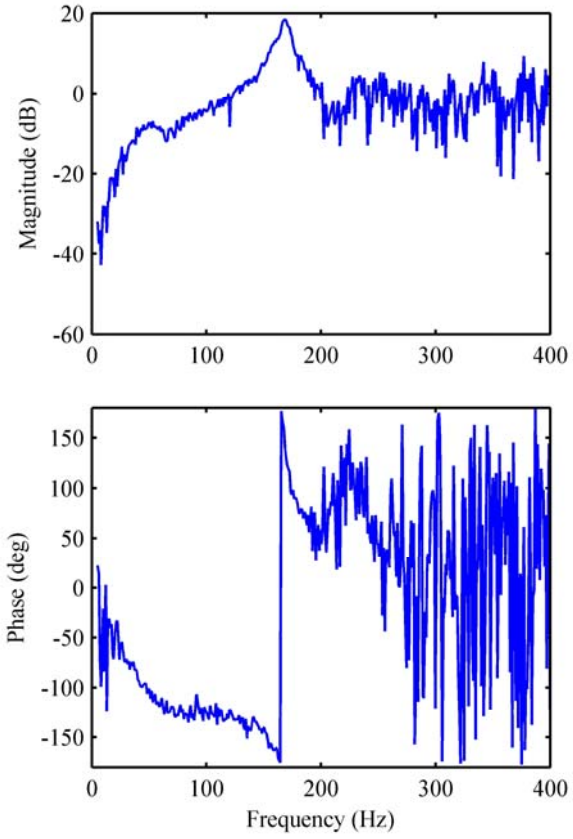

Figure 3.27 – Acoustic transfer function measured in the self-excited combustor.

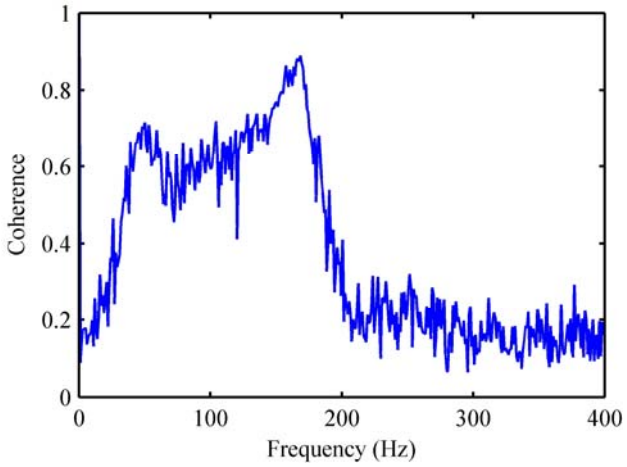

Figure 3.28 - Coherence of the acoustic transfer function as a function of frequency.

As with the flame transfer function, we may make some inferences about influence on unstable behavior from the character of the acoustic transfer function. The acoustic transfer function exhibits low magnitude at low frequencies, rising to a peak around 160 Hz. This peak corresponds with a calculation of the ¾ wave longitudinal mode in the combustor based on its full length in the self-excited configuration (approximately 1.58 m). The magnitude at low frequencies is in fact below the 0dB required for instability, while the peak reaches 20dB. This is significant in that it indicates that low frequency instability will rely on amplification through the flame transfer function, while the acoustic transfer function provides sufficient gain on its own at the 160 Hz peak. Further, the gain of the 160 Hz peak may overcome reduced gain in the flame transfer function at this frequency. Additionally, the acoustic transfer function will apply a phase shift of about -100° over a wide frequency band, experiencing a rapid shift of an additional -180° over the 160 Hz resonance. This rapid phase shift makes intercepts of a 360° phase crossing in the combined transfer function over that region more likely. As it coincides with a region likely to have high gain due to the corresponding amplitude peak, this frequency range is a strong candidate for potential instability.

3.7 Unstable Characterization of the Self-Excited Combustor

Now that the acoustic and flame prototype transfer functions are known, everything necessary to make predictions of unstable operating condition is known. Let us then

consider the actual unstable behavior of the combustor, with which we will compare the predictions. The unstable combustor behavior was characterized using the acoustic pressure signal measured with a microphone located at the hotwire measurement location, as described in Section 2.9. The combustor was observed to have an increase in sound pressure level from a peak of 122 dBSPL to a peak of 139 dBSPL (or higher) in becoming unstable, representing a factor of 6 increase in the amplitude.

Though the actual behavior of the combustor depends heavily operating condition, we may observe a few generalities based on experience obtained first-hand while making the measurements. In addition, these descriptions help provide a look at the unstable operation in a more familiar form. At suitable mean flow rates, the combustor appeared to exhibit two unstable modes as the equivalence ratio was increased. First the combustor went unstable in a "high" frequency mode. As the equivalence ratio continued to be increased, the overall sound level decreased, and reached a new tonality, still different from the stable operation. With further equivalence ratio increase, this mode grew into a very high amplitude instability at a lower frequency. A quantification of this qualitative description for the amplitude is shown for a flow rate of 13.6 g/s in Figure 3.29.

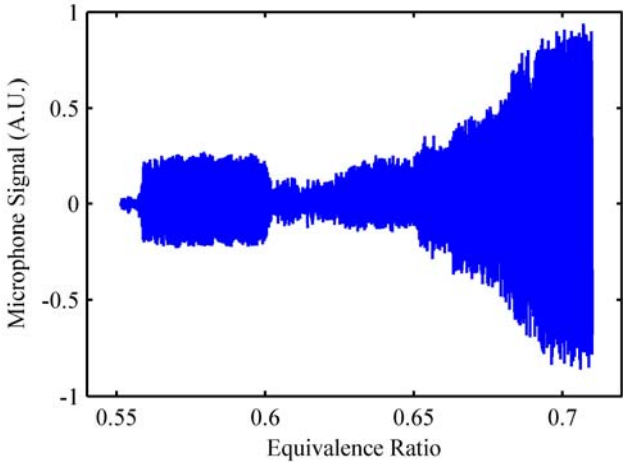

Figure 3.29 - Dynamic pressure measurement as a function of equivalence ratio, measured in a sweep by increasing equivalence ratio as a function of time.

We may also consider the characteristics of these instabilities by looking at the power spectrum at a variety of equivalence ratios for a fixed flow rate of 16.3 g/s. These results are shown in Figure 3.30. As discussed, at lean equivalence ratios, the combustor operates in a stable mode. As the equivalence ratio is increased, the combustor becomes unstable around 160 Hz. With further increases in equivalence ratio, this mode shifts slightly to higher frequency, and a lower frequency mode begins to develop around 100 Hz. The 100 Hz peak then shifts to higher frequency, becomes the dominant peak, and experiences significant broadening, along with the rise of a relatively significant harmonic. In addition to these peak trends, increasing equivalence ratio sees a substantial rise in the baseline broad band sound pressure level in the combustor.

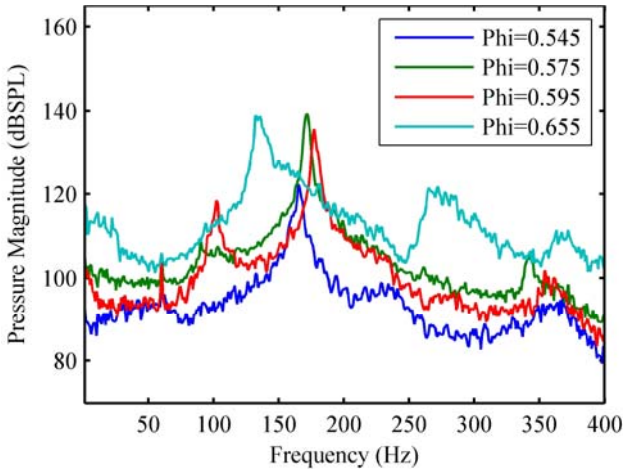

Figure 3.30 - Sample microphone power spectra for several equivalence ratios at a mass flow rate of 16.3 g/s.

While this discussion provides a brief snapshot of instability, complete quantification of the combustor behavior was performed, resulting in a series of waterfall plots showing the evolution of the combustor power spectrum as a function of equivalence ratio for all operating conditions. Two limits of instability were used over the course of instability prediction and comparison, a level of 120dBSPL and a level of 129dBSPL. These thresholds were determined empirically. Both levels will be marked, with thick and thin lines respectively, on the forthcoming waterfall plots of the combustor sound pressure level. To begin in Figure 3.31, at the lowest flow rates, it is clear that instability is only marginally achieved, and only the high frequency (~160 Hz) mode is excited.

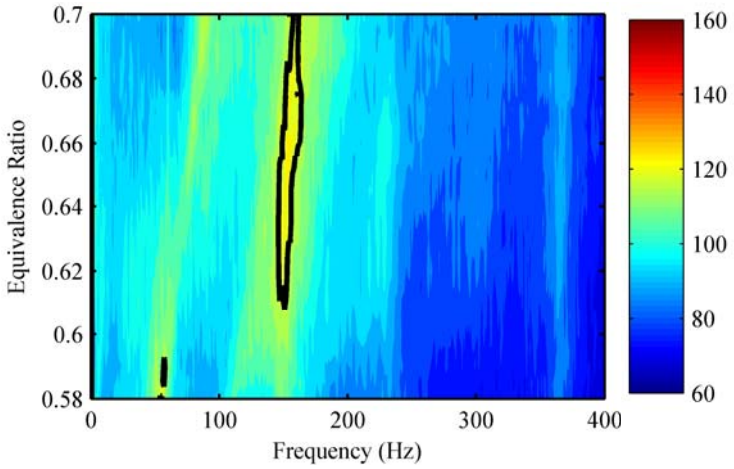

Figure 3.31 - Waterfall plot for self-excited natural gas combustion at a flow rate of 5.43 g/s. Marked amplitudes are 120 dBSPL and 129 dBSPL.

Increasing flow rate, seen in Figure 3.32, shows that the while the unstable amplitude is somewhat higher, the high frequency mode remains the one primarily excited, with a slight rise of a lower frequency mode at the highest equivalence ratios considered. Frequencies consistently increase with increasing equivalence ratio.

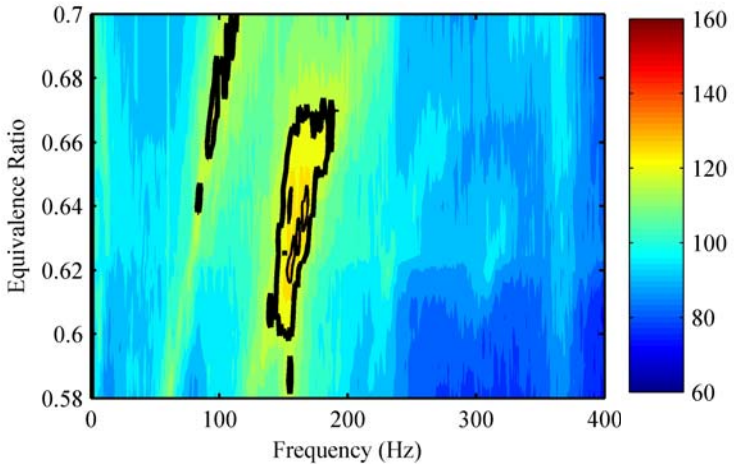

Figure 3.32 - Waterfall plot for self-excited natural gas combustion at a flow rate of 8.15 g/s. Marked amplitudes are 120 dBSPL and 129 dBSPL.

As the mean flow rate is further increased, in Figure 3.33, the overall amplitude of the instabilities increases, as does the background excitation. At this flow rate, the trend in combustor behavior described previously is clearly evident. A high frequency mode is

present at lean equivalence ratio which shifts to a lower frequency mode as equivalence ratio increases. Also of note is the visible presence of harmonics, notably those of the low frequency (~100 Hz) instability. Additionally, trends in the frequencies on the instabilities become clearer. Both modes of instability continue to exhibit a trend of increasing frequency with increasing equivalence ratio. However, the high frequency mode exhibits less of a change in frequency with equivalence ratio than does the low frequency mode.

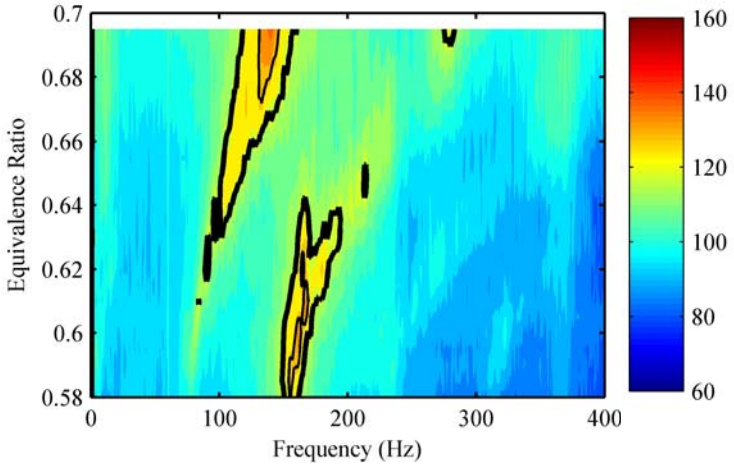

Figure 3.33 - Waterfall plot for self-excited natural gas combustion at a flow rate of 10.9 g/s. Marked amplitudes are 120 dBSPL and 129 dBSPL.

Further increase of the mean flow rate, depicted in Figure 3.34, exhibits a repeat of the behavior already described. Overall magnitudes, as well as the background noise levels, increase. Two modes of unstable excitation are observed, with harmonics evident. Frequencies increase for both modes, though less for the high frequency mode. Additionally, a behavior has become more evident, especially in the low frequency mode, namely the increased broadening of the peak with a continued increase in equivalence ratio.

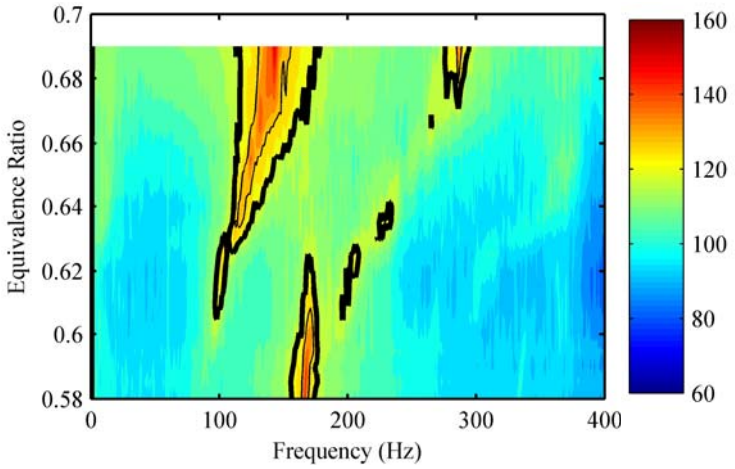

Figure 3.34 - Waterfall plot for self-excited natural gas combustion at a flow rate of 13.6 g/s. Marked amplitudes are 120 dBSPL and 129 dBSPL.

At the final flow rate considered (Figure 3.35), the behaviors continue to be the same as those already described. The most significant new point to emphasize is the quite low upper bound on the measurements. This bound was encountered due to an inability of the acquisition hardware to continue to perform under the vibration encountered due to the ambient noise levels caused by the combustor operating in this high level self-excited mode.

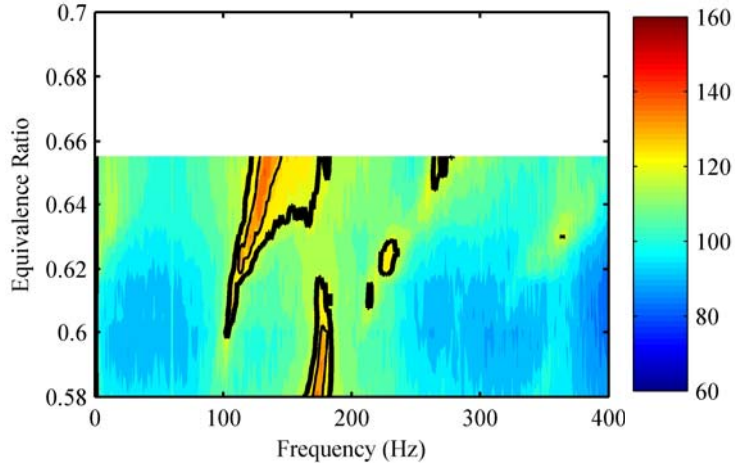

Figure 3.35 - Waterfall plot for self-excited natural gas combustion at a flow rate of 16.3 g/s. Marked amplitudes are 120 dBSPL and 129 dBSPL.

One trend which is difficult to observe from these plots is that the frequencies of instability exhibit a slight shift to higher frequency with increases in the flow rate. This can be seen most apparently by considering the point at which the unstable mode is first observed for a given flow rate as one moves from plot to plot.

While these waterfall plots provide a picture of the unstable frequency as well as amplitude, it is also useful to consider the unstable operation as it occurs relative to both operating parameters simultaneously, as in Figure 3.36. This plot represents the maximum pressure amplitude at any frequency, at the specified operating condition. The same instability boundary limits of 120dBSPL and 129dBSPL are marked as before. The most significant new observation from this plot is that with increasing flow rate, instabilities are encountered at leaner equivalence ratios. This trend (that instabilities are more likely with higher equivalence ratio and mass flow rate) agrees with what we would expect based on the behavior of the flame transfer function bandwidth and gain. The leftmost unstable region is most associated with the high frequency mode, while the region in the upper right corner is associated with the low frequency mode.

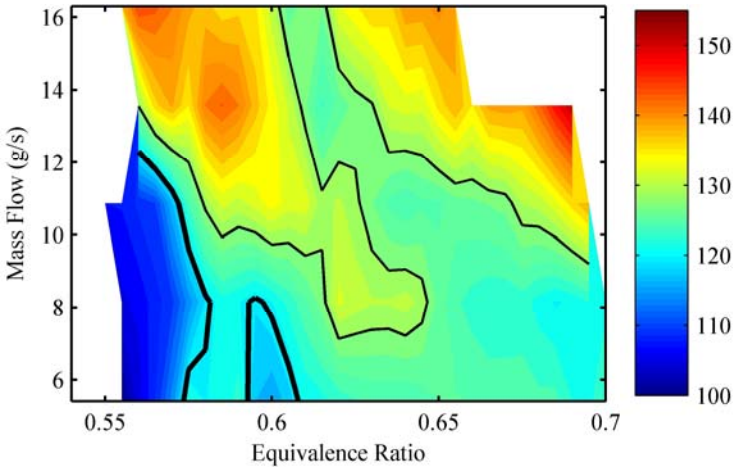

Figure 3.36 - Unstable operating map for natural gas in the self excited combustor. Marked amplitudes are 120 dBSPL and 129 dBSPL.

3.8 Combined Flame and Acoustic System Transfer Function

With knowledge of the actual combustor behavior, we may now begin to look at the instability predictions resulting from the closed-loop system model, as depicted in Figure

3.37. Recall from Section 2.11 that this realization focuses on analysis of the open-loop transfer function of the feedback loop, which in this case is the product of the flame and acoustic transfer functions. This transfer function will be tested with respect to the Bode criterion for stability. Thus, frequencies where the phase is a multiple of 360° will be identified. Those frequencies will then be tested for magnitudes representing amplification (greater than 0dB).

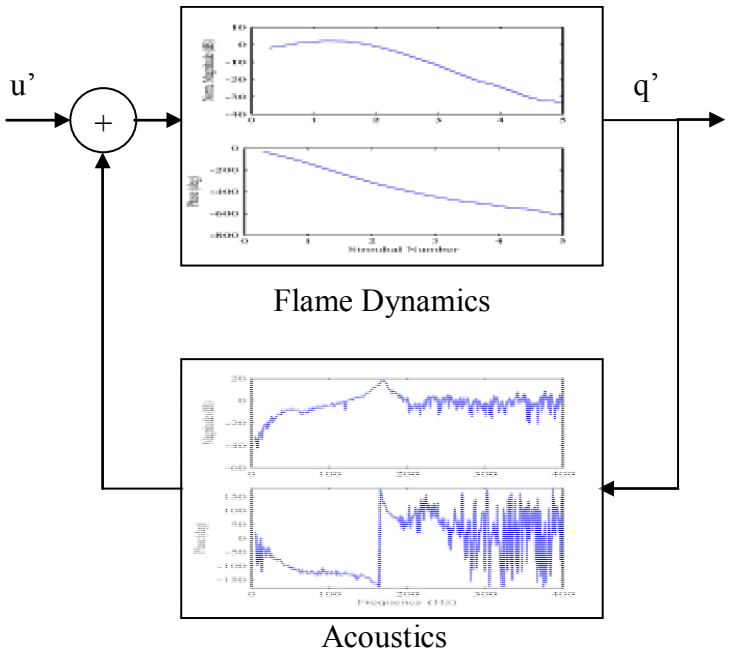

Figure 3.37 - Closed-loop model used for prediction of instabilities.

The actual combined transfer function for this system is depicted for a reduced set of operating conditions in Figure 3.38. Additionally, the frequencies shown for this transfer function are limited due to the loss of coherence in the acoustic transfer function beyond 200 Hz. This does not have an effect on the ability to predict instabilities in the actual combustor since, as seen in the preceding section, all instabilities were observed below this limit. In Figure 3.38, changes in mass flow rate are depicted with a changing marker, while changes in equivalence ratio are noted by color.

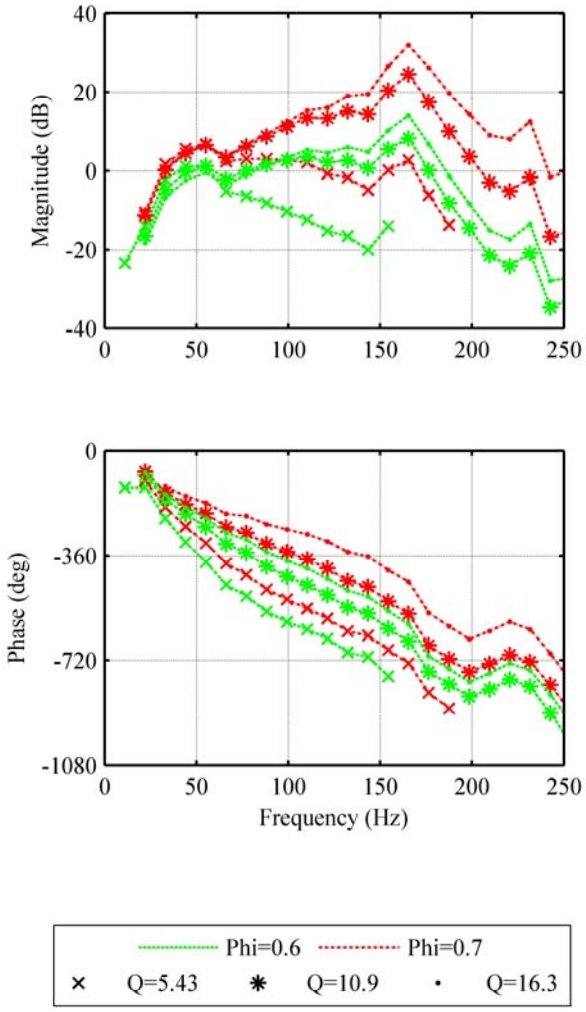

Figure 3.38 - Combined open-loop system transfer function used for prediction of instabilities in the self-excited combustor. Changes in marker are changes in flow rate, while changes in color are changes in equivalence ratio.

In the open-loop system transfer function, several features of interest are visible. The peak around 160 Hz in the acoustic transfer function is still present resulting in high gain near that frequency. The effect of the flame transfer function's low-pass filter characteristic is clearly visible, with the gain remaining nearly constant (within 10dB) at low frequency, but exhibiting substantial variation (40dB) at higher frequencies. Increasing the flow rate and the equivalence ratio thus both raise the gain at higher frequencies due to their increases in the flame bandwidth, allowing the gain to remain

high over a wider band. The phase remains predominantly linear with one major exception, that of the rapid roll off around 160 Hz caused by the acoustic resonance. This rapid phase shift causes a higher probability of a phase crossing occurring at this point.

The gain shows some interesting behavior relative to the potential for predicted unstable operation. At the highest condition in both mass flow rate and equivalence ratio, frequencies between around 40 Hz and 250 Hz show a uniform amplifying gain, so any phase crossing could be expected to exhibit instability. Decreases in the equivalence ratio from this maximum condition have a greater effect on the potential for instability in the gain than do changes in the mass flow rate. Decreases in both operating parameters, however, still provide amplifying gain both in a low frequency band and around the 160 Hz resonant peak.

From the open loop system transfer function, it is apparent that there are two primary phase crossings of interest to the instability predictions, those at -360° and -720°. The actual position of these phase crossings is dominated by the change in flame transfer function time delay discussed in Section 3.4.2. As the time delay increases, the phase crossings occur sooner (i.e. at lower frequency). So increases in equivalence ratio and mass flow rate are seen to increase the frequencies at which phase crossings occur, as seen in Figure 3.39. For most flow rates, it is apparent that the frequency variation of the -720° crossing with equivalence ratio is less than that of the -360° crossing. Agreeing with observation, this is likely due to the rapid phase shift due to the acoustic resonance which occurs near the second crossing.

Qualitative interpretation of the predicted unstable map of the combustor based on this open-loop system transfer function agrees well with the unstable behavior of the actual combustor. Phase crossings are observed to result in increases in frequency with increasing equivalence ratio and mass flow rate. This effect is more significant for the low frequency peak mode of instability (associated with the -360° crossing) than the high frequency, exactly as observed in the unstable combustor measurements. Additionally, a mechanism for shift between the high frequency and low frequency modes is apparent. The resonant acoustic peak does provide a significant gain in the transfer function, but

increases in the mass flow rate and equivalence ratio reduce the delay to such an extent as to move the second phase crossing to higher frequencies, outside of the influence of this significant peak. However these same changes result in increases in the gain in a broad band frequency range, allowing the first phase crossing to result in a single potential instability even though its gain is lower than that at the resonant peak. At low mass flow rates and equivalence ratios, the potential unstable gains are isolated, and would be expected to result in spotty predictions of instability, if any at all, also observed in the unstable mapping measurements.

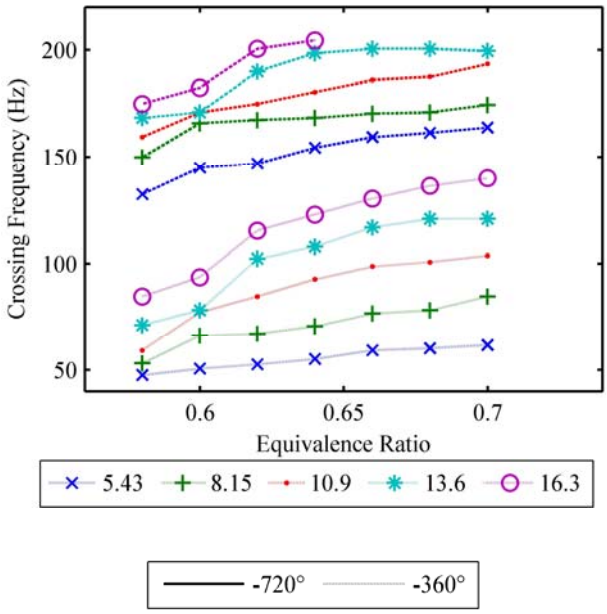

Figure 3.39 - Change in phase crossings as a function of operating condition. Thick line represents -720° phase crossings, while thin line represents -360° phase crossings.

3.9 Predictions of Instabilities Based on Closed-Loop Models

While qualitative explanations provide similar expectations for instability occurrence to those measured, a true quantitative prediction of instabilities is necessary to asses the efficacy of the closed-loop modeling technique. It is most useful to compare these predictions with the measurements of unstable operating condition using the waterfall plots at fixed mass flow rates, as described in Section 3.7. First, however, a word of

explanation is necessary on the methodology used in calculating the predictions of instability shown here.

As mentioned in Section 2.11, the phase crossings were identified using a 40° (+/- 20°) band around the true phase crossing to prevent experimental scatter from causing potential instability points to be missed. This results in the possibility for a number of instabilities to be predicted at each operating condition. These multiple predictions of instability are shown in the plots below. Since this resulted in many potential unstable frequencies at each equivalence ratio, a reduced set of predictions was also determined by using a second level of filtering. The many predicted instabilities were reduced to a single prediction per equivalence ratio by selecting the potential unstable frequency at each operating condition whose system transfer function gain was highest. Since nonlinearities in a practical system may prevent multiple modes of instability from occurring, this filtering is intended to add a physical correction for the linear nature of the predictions. These results are also shown in comparison with the unstable combustor measurements.

One final note is necessary on the comparison of predictions and measurements of unstable combustion in the self-excited combustor. For all conditions, two threshold levels of instability are depicted for the experimental instability measurements, one at a level of 120dBSPL (red) and one at a level of 129dBSPL (yellow). These levels were selected empirically for these measurements, as they result in the most visually appealing depiction of the unstable characterization. Predicted instabilities are shown in the following figures as large black dots.

Results of the comparison between prediction and experiment are shown for the lowest mass flow rate (5.43 g/s) in Figure 3.40, including all potential instabilities identified. For this operating condition, unstable operation was only observed at the 160 Hz acoustic peak in the actual combustor. However, predictions primarily identify the low frequency mode. When the predictions are limited to only the frequency with the highest gain margin (Figure 3.41), the low frequency mode is exclusively identified. Considering the open loop system transfer function for this flow rate, it is evident that the low flame

transfer function bandwidths associated with the reduced flow rate prevent the 160 Hz resonant peak from reaching an amplifying gain for most equivalence ratios. While it is true that the high frequency mode is underpredicted, and never becomes the dominant mode, its frequency is accurately predicted, evidenced by a cluster of points in Figure 3.40.

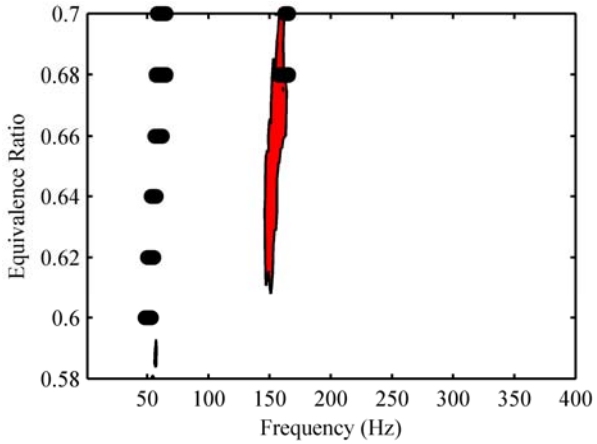

Figure 3.40 - All predicted unstable points for the 5.43 g/s mass flow rate. Black dots represent predictions, while colored regions are thresholded measurements.

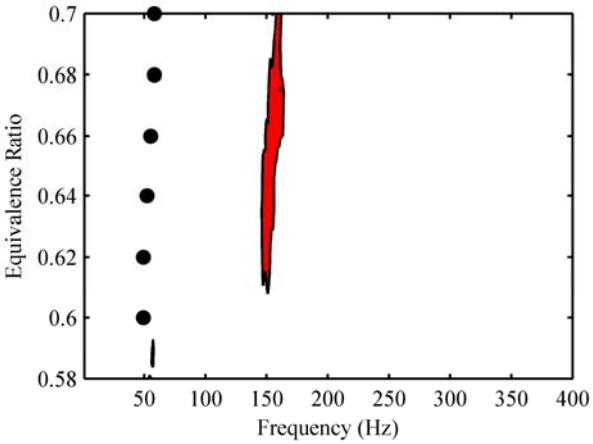

Figure 3.41 - Predictions of instability for 5.43 g/s mass flow rate downselected to only the prediction with the highest gain margin. Black dots represent predictions, while colored regions are thresholded measurements.

As the mean mass flow rate is increased, the predictions become somewhat more successful. In Figure 3.42, all predicted potential instabilities are shown. In the practical

combustor, two modes of instability are observed, one around the acoustic resonance and a second less substantial mode at lower frequency. The frequencies of both modes are identified by the predictions at equivalence ratios where they overlap, with the most deviation occurring for the low frequency mode. Considering only the highest magnitude predicted points (Figure 3.43) results in elimination of the low frequency mode altogether, suggesting overprediction of the high frequency mode for this mean flow rate. It is still of note that the potential for instabilities was predicted for the low frequency mode, though their gain prevents them from dominating.

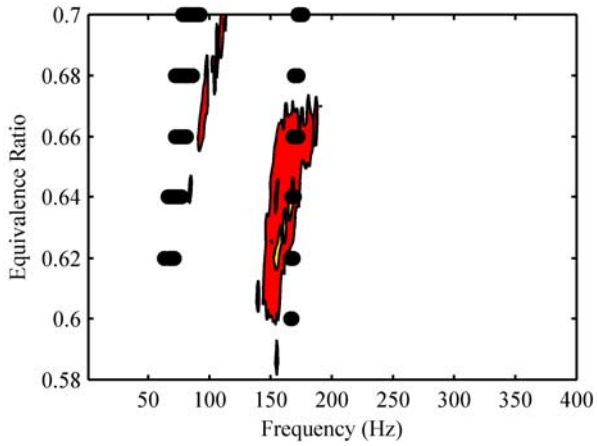

Figure 3.42 - All predicted unstable points for the 8.15 g/s mass flow rate. Black dots represent predictions, while colored regions are thresholded measurements.

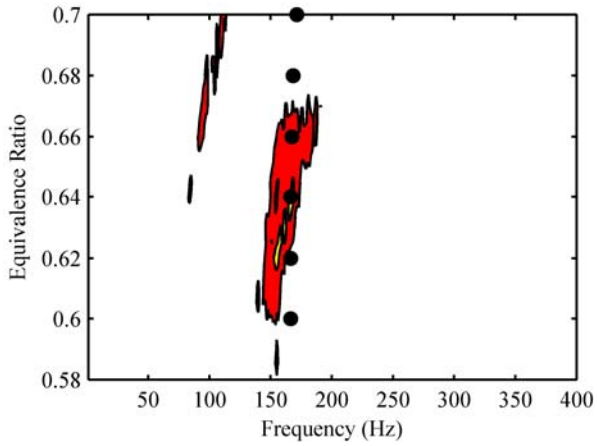

Figure 3.43 - Predictions of instability for 8.15 g/s mass flow rate downselected to only the prediction with the highest gain margin. Black dots represent predictions, while colored regions are thresholded measurements.

The results continue to improve advancing to a mean flow rate of 10.9 g/s, as shown in Figure 3.44. Two modes are observed experimentally, with a shift occurring around an equivalence ratio of Φ=0.64. Using the magnitude limitation on predictions, as shown in Figure 3.45, the shift between modes is observed, but occurs at slightly higher equivalence ratios relative to the measurements. Frequencies are slightly underpredicted for the low frequency mode. As expected due to the linearity of these predictions, the slight appearance of harmonics of the low frequency mode is not predicted. While the shift in dominant mode is missed, the occurrence of the shift is still predicted, suggesting that the error is in the relative magnitudes of the modes.

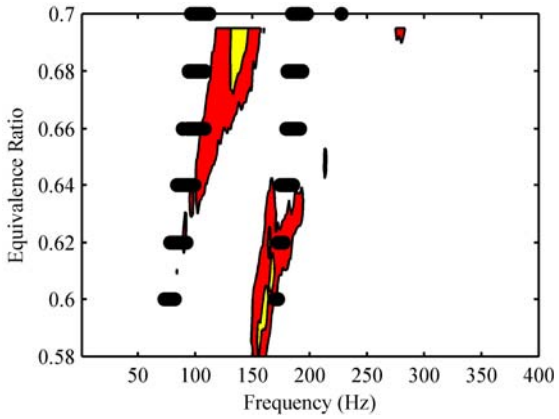

Figure 3.44 - All predicted unstable points for the 10.9 g/s mass flow rate. Black dots represent predictions, while colored regions are thresholded measurements.

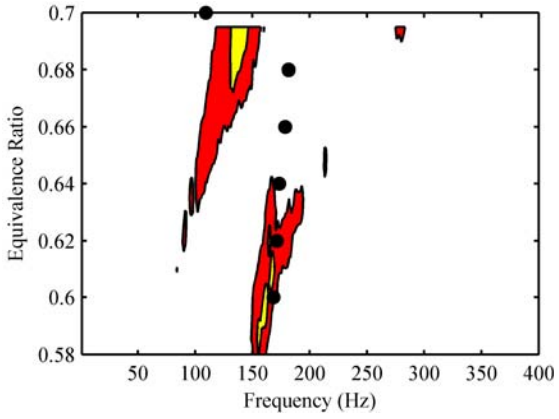

Figure 3.45 - Predictions of instability for 10.9 g/s mass flow rate downselected to only the prediction with the highest gain margin. Black dots represent predictions, while colored regions are thresholded measurements.

At higher flow rates, the experimentally measured unstable operation remains similar. As shown in Figure 3.46, frequencies predicted for the observed modes are a better match with the measurements. The potential existence of both modes is predicted, and when we attempt to observe the shift in dominant mode using the magnitude selection criterion, as shown in Figure 3.47, we observe that the shift is predicted closely. Harmonics of the low frequency mode are visible in the experimental measurements, but as expected, are not predicted.

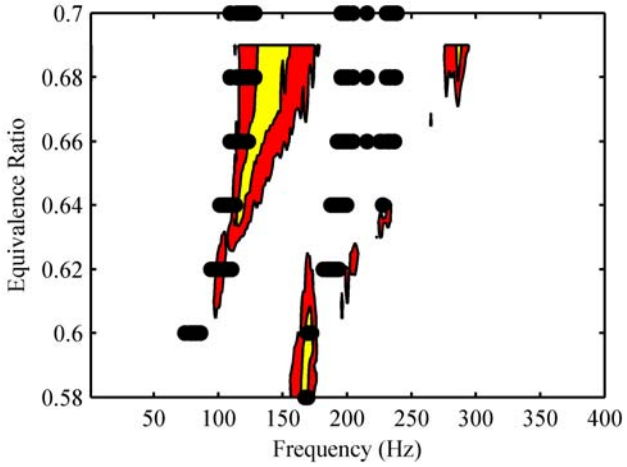

Figure 3.46 - All predicted unstable points for the 13.6 g/s mass flow rate. Black dots represent predictions, while colored regions are thresholded measurements.

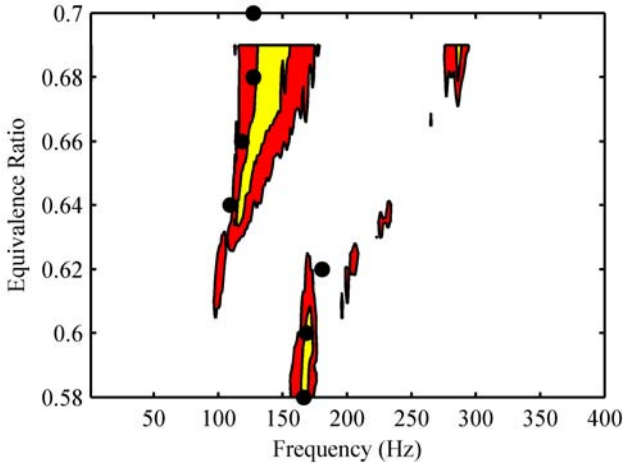

Figure 3.47 - Predictions of instability for 13.6 g/s mass flow rate downselected to only the prediction with the highest gain margin. Black dots represent predictions, while colored regions are thresholded measurements.

The instability predictions for the final flow condition of 16.3 g/s are shown in Figure 3.48. As with the previous cases, frequencies are matched relatively well, even as they shift with increases in equivalence ratio. The most telling result for this flow condition is that of the gain margin limited predictions, found in Figure 3.49. The crossover between the high and low frequency modes of instability is again predicted quite well.

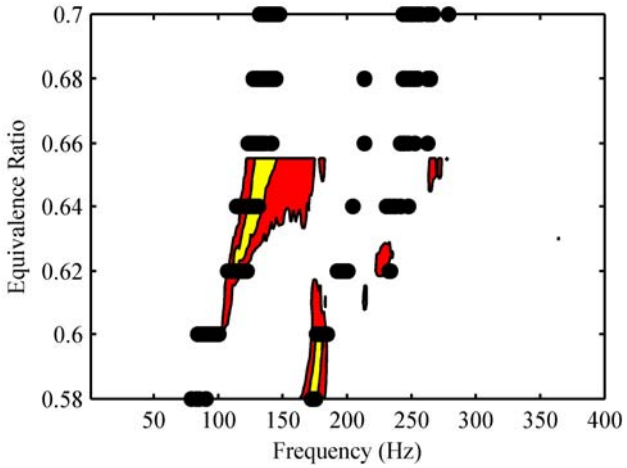

Figure 3.48 - All predicted unstable points for the 16.3 g/s mass flow rate. Black dots represent predictions, while colored regions are thresholded measurements.

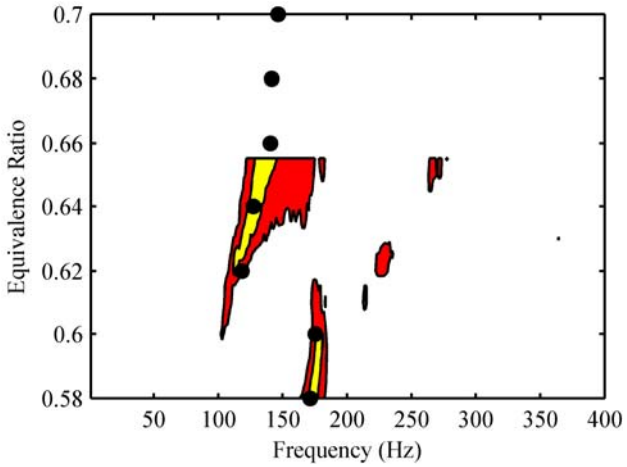

Figure 3.49 - Predictions of instability for 16.3 g/s mass flow rate downselected to only the prediction with the highest gain margin. Black dots represent predictions, while colored regions are thresholded measurements.

It may also be useful to consider a map of the maximum gain margin of any predicted unstable operating condition, as shown in Figure 3.50, and the number of predicted unstable frequencies for a given operating condition, found in Figure 3.51. Each of these plots could in a sense be viewed as some measure of the likelihood of instability occurring at these operating conditions. Both of these plots appear similar. Further, they reveal a similar trend to that observed in the experimental instability map. Instability is more likely with both increasing equivalence ratio and mass flow rate, and increases in flow rate result in a higher propensity for instability at leaner equivalence ratios.

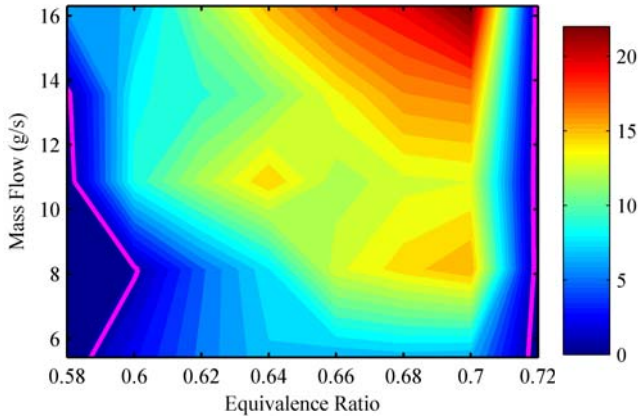

Figure 3.50 - Map of gain margin as a function of mass flow rate and equivalence ratio. Units on color axis are dB in the open loop system model magnitude. The pink line represents 0dB, the explicit limit for instability.

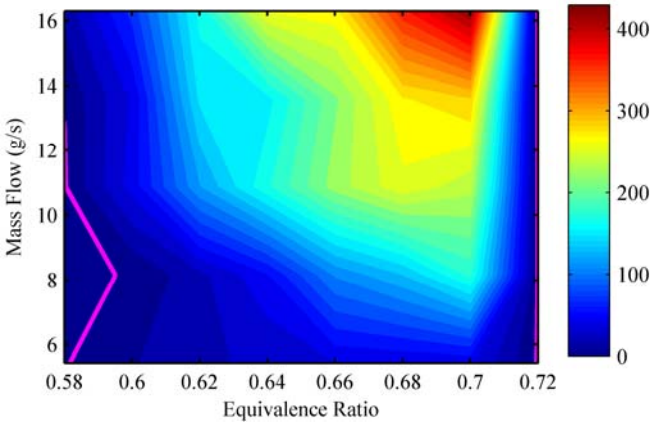

Figure 3.51 - Map of number of unstable points predicted at each operating condition. Color axis unit is number of points with amplifying gain. Pink line represents a level of 1, the theoretical border of instability.

On the whole, the predictions of the occurrence of instability based on the linear closed-loop system model were relatively successful. The frequencies at which instability occurred, as determined by the phase crossings (and thus time delay) were predicted very successfully. This is an especially significant result. It is common in literature for changes in frequency observed in instabilities to be attributed to non-linearities. As these measurements show, for the combustor used in this study, frequency shifts relative to operating condition could be explained simply by the moving phase crossings associated with changes in time delay. In addition, the correct prediction of the low frequency unstable mode is significant in that it is not associated with an acoustic resonance in the combustor. While this behavior would typically be explained as a non-linear phenomenon, it becomes evident from the analysis shown here that its occurrence was predicted sufficiently by linear modeling.

While frequencies were predicted quite well, predictions of the actual occurrence of instabilities were less successful. This could be due to a combination of factors, including slight errors in the gain, or transfer function shape. The efficacy of the predications improved with increasing mean mass flow rate, resulting in extremely accurate predictions of the instability frequency and the crossover between unstable modes at high flow rates.

Predictions of thermoacoustic instabilities using closed-loop system models appear to be a useful tool for design level avoidance of instabilities. The analysis herein was performed using a prototype flame transfer function, knowledge of the flame size, and knowledge of the combustor acoustic transfer function. According to the work by Black [3], it was shown that the acoustic transfer function may be successfully modeled using linear finite element models, which are possible based only on proposed combustor geometry. With further generalization of the nondimensional flame transfer function, it should be possible to limit the design stage requirements for prediction of thermoacoustic instabilities to knowledge of the combustor geometry and the flame size. This would provide an invaluable tool, allowing dynamic behavior to be analyzed and predicted prior to fabrication.

Chapter 4 - Conclusions and Recommendations

This study was an attempt to make progress toward design stage predictive capability for thermoacoustic combustion instabilities. This goal is necessary in opening the door to better solutions to the problem of combustion dynamics. The study was broken up into two phases, each addressing a different part of the problem. First, novel measurements of the flame dynamics were made, including characteristics based on the spatial distribution of the flame, for its response to velocity perturbations. These measurements make a contribution to reduced-order modeling of flame dynamics. Second, an instability prediction technique based on closed-loop linear system models, using experimentally derived flame and acoustic transfer functions was verified against measurements of unstable combustion in a self-excited combustor. This technique shows potential as a design tool for avoiding thermoacoustic instabilities in practical systems. Both of these efforts were successful in contributing to the body of knowledge on thermoacoustic combustion instabilities.

4.1 Summary of Phase 1

Novel measurements of the flame dynamics were made, by including the flame reaction volume and the offset to the center of flame heat release rate as indicators of the spatially distributed flame structure. These measurements were made using a phase averaged, line-of-sight imaging technique. The response of the offset and volume was observed to be nearly identical to the already well known dynamics of the flame heat release rate. These measurements showed that the spatial measurements respond with the same the low-pass filter characteristic as the heat release rate, exhibiting a similar bandwidth, phase roll off rate and magnitude reduction over a variety of equivalence ratios.

The implications of this result are threefold. Firstly, since the flame heat release transfer function is directly proportional to the response of the flame volume to velocity excitations, the flame heat release rate dynamics may be said to be the direct result of fluid mechanical interactions. Observations from flame images, as well as the observed transfer function time delay imply that this behavior is related to flame interaction with convective flow structures. The dynamics of the spatial response may be considered

somewhat analogous to the behavior modeled using flame sheets, predicting the heat release rate simply as a constant multiple of a geometric characteristic of the flame, in this case the volume. Secondly, as a result of the fluid mechanical coupling observed in the heat release rate response, predictions of the flame dynamics must make modeling of flame-fluid interactions their primary focus in order to accurately model the response. Finally, the success of the phase-averaged spatial measurements provides support for use of time averaged turbulence approximations when modeling the flow field to which the flame is subject.

As mentioned the spatial response of the flame appears to have a relationship to the motion of coherent structures through the flame. The linear phase, indicating time delay timescales comparable to flow convection through the flame strongly supports this assertion. In addition, the bandwidth behavior may be explained by decreases in the length scale of these structures associated with increases in frequency, which would result in a reduced impact a fixed size of flame. Finally, the relationship to coherent structure interaction is supported by the Strouhal number based nondimensionalization of the flame transfer function, which was successful using a convective offset based timescale.

4.2 Summary of Phase 2

Phase 2 of this study was a novel attempt to make and validate experimentally based predictions of combustion instabilities in a self-excited combustor using a linear closed-loop system model of the feedback loop. Measurements of the flame transfer function resulted in a suitable nondimensional prototype of the flame transfer function which was used to recreate the flame transfer function at any operating condition. The acoustic transfer function was measured and provided suitable coherence in the frequency range of interest. The flame and acoustic transfer functions were combined resulting in the open-loop system transfer function, which was used to make predictions of unstable operating condition by applying the Bode criterion. Use of this model relied only on advance knowledge of the flame size as a function of operating condition, knowledge of the low frequency gain as a function of operating condition, and knowledge of the combustor

acoustics. It is thought that this model may provide a simple tool that may be applied in the design stages to avoid the occurrence of thermoacoustic instabilities.

Accurate prediction of the system time delay proved most important in finding potential instabilities, due to its impact on the frequencies at which phase crossings occurred. Accurate knowledge of the phase alone thus allows some insight into the frequencies at which instabilities might be an issue. As delay decreases with increasing flame size, it is also possible to predict how these frequencies will change with changes in operating condition. The knowledge of these frequencies of interest over the desired operating range of a potential design could be used to help guide modifications to the design to help avoid instabilities.

Based on the measurements made in this study, high equivalence ratio and high mass flow rate in combination appear to make instability a near inevitability. These conditions result in a uniformly high gain (due primarily to extended bandwidth) in the flame transfer function, so any phase crossing would be expected to result in instability. This is reflected by the measurements made in the self-excited combustor. However, the final determination for these cases still depends on the acoustic transfer function, whose gain (or lack thereof) may be enough to trump any propensity of the flame itself to lead to instabilities. So the acoustic transfer function of the combustor really represents the final word as to stability. This is further evidenced by the fact that it is possible to operate the combustor in a mode that experiences no instabilities simply by changing the combustion section length.

Knowledge of combustor acoustics and behavior of flame size and gain with respect to operating condition is sufficient to make predictions of unstable operating conditions. These predictions have experimental support in that they have been validated against measurements made in an actual self-excited combustor. The real power of these predictions lies in their use at the design stage for new combustors under development. The predictions were most accurate in identifying significant frequencies for potential instability, as well as how these potential frequencies changed with respect to operating condition. Thus, given combustor geometry, predictions are possible for how changes in

operating condition would be expected to lead to instabilities, and how changes in the geometry (changing the acoustic transfer function) may alleviate these.

4.3 Topics for Further Study

The developments of understanding of the spatial nature of flame dynamics, and the use of linear feedback system models for predictions of instabilities are significant in their own right. However, additional areas for study remain as a result of this progress, for which further future research is necessary. This future work will serve to build upon, and further generalize, the work detailed here. The following recommendations are made as areas for potential future study:

1. A more complete mapping of the size/shape of the flame is necessary to create a universal basis on which the flame transfer function characteristics of bandwidth and time delay can be based. This mapping may include the effects of swirl, preheated reactants and elevated combustor pressure just to name a few. Extension of the flame size mapping to include these effects would provide a wider ability for prediction of self-excited operation, which could then be tested using the rig in its unstable configuration. This would help to provide a wider validation of the efficacy of the closed-loop system stability predictions, and to extend the validation of these predictions to operating conditions closer to those found in gas turbine combustors.

2. The flame heat release rate dynamics have been shown to be related to fluctuations in the size of the flame. Qualitative observations, as well as inferences based on literature, have linked these fluctuations to interaction between the flame and coherent flow structures which pass through it, and that the sizing of these structures intuitively leads to behaviors similar to those observed in the flame transfer function. Actual measurement and modeling of forced vortex shedding, structure and breakdown in the reaction region would provide insight into the role played by these structures in determination of the flame dynamics.

Additionally, it was observed that there are very slight differences in scaling for the Strouhal number for the flame transfer function magnitude and phase. It would be useful to investigate this difference by introducing variations in the geometric configuration of the combustor to determine if these different scaling values are indeed tied to geometric constraints or are coincidental. Further, by deliberately inducing vortices in the flow at a known location, more precise physical measurement of the convective length scales ought to be possible. Both of these endeavors would serve to generalize predictive capability for the flame dynamics, ensuring that the same Strouhal number scaling may be used independent of combustor geometry.

Following this same line of thought, the flames considered in this study were primarily attached at the quarl and centerbody stabilization zone. Lifted flames would be expected to result in a similar response, albeit with a longer time delay. That is, the flame response observed in this study was linked to interaction with convective structures. A lifted flame would be expected to be interact similarly with these same structures, but the structures would experience greater convection times in reaching the center of flame heat release rate due to the increased offset distance through the longer region upstream of the reactions. As such, a lifted flame would be expected to serve as an excellent test configuration to further generalize the scaling laws at play in the flame transfer function nondimensionalization.

3. The spatial dynamics of the flame transfer function were linked to the heat release rate dynamics by using phase-averaged, deconvoluted, line-of-sight dynamic measurements of the reaction region. Further validation of these measurements would be possible by employing more advanced diagnostic techniques which were not available for this study. High speed photography would eliminate the need for phase averaging, allowing instantaneous measurements of the reaction region to be made, allowing a

higher resolution of flame interaction with passing structures, and allowing coherence between the input and output of the transfer function to be calculated. Application of planar laser-induced fluorescence (PLIF) measurements to image the flame in cross section may also provide further insight into the spatially resolved dynamics, eliminating the need for deconvolution processing. These measurements may serve as a further confirmation of the relationship between the flame heat release rate and spatial response transfer functions.

4. As described in the background section, several investigators have observed a capacity for passive control of combustion instabilities through control strategies which break up coherent structures in the flow. Measurement of the flame transfer function under these control strategies should reveal changes in the transfer function characteristics that would change the nature of the closed-loop feedback model of instability occurrence. Analysis of the changes in flame transfer function characteristics caused by these passive control techniques would help to provide insight into why they are successful at eliminating instability, and to provide a framework with which to project the success of other passive control techniques. Additionally, such measurements would test the versatility of the system model in making stability predictions by testing its ability to handle a wider variety of system configurations.

5. Measurements made in this study only considered the effect of velocity coupling with the flame heat release rate. Equivalence ratio coupling remains an important coupling mechanism however, observed in many actual unstable combustors. Prior work by the author suggests that flame transfer functions for equivalence ratio oscillations do not obey the same relationship with flame size as do those of velocity oscillations. Measurements of the spatially resolved flame transfer functions with respect to equivalence ratio oscillations would reveal the mechanism by which this coupling occurs, and allow comparison with that of the velocity

oscillations. It would also be useful in generating a potential prototype for the equivalence ratio oscillation based flame transfer function, which could be used to also allow predictions of thermoacoustic instability driven by equivalence ratio oscillations to be made.

In addition, development of a combustor for laboratory use which is deliberately susceptible to equivalence ratio oscillations is not a simple task. Performing such a design may be made easier if based on advance predictions of the occurrence of instabilities made using a closed-loop system model. Design of such a combustor using the closed-loop system model technique would not only allow validation of the closed-loop model for use with equivalence ratio oscillations, but serve as a test ground for a design stage process in which closed-loop models may be used for prediction of thermoacoustic instabilities. These measurements would provide both the knowledge necessary to make equivalence ratio oscillation coupling predictions, but also extend the capability of closed-loop system models as a general design tool for thermoacoustic instability avoidance in the design of new combustion systems.

Appendix A - References

[1] Balachandran, R., Ayoola, B.O., Kaminski, C.F., Dowling, A.P. and Mastorakos, E., 2005, "Experimental investigation of the nonlinear response of turbulent premixed flames to imposed inlet velocity oscillations," Combustion and Flame, **143**, pp 37-55

[2] Bellows, B.D., Bobba, M.K., Seitzman, J.M. and Lieuwen, T., 2006, "Nonlinear flame transfer function characteristics in a swirl-stabilized combustor," Proceedings of GT2006 ASME Turbo Expo 2006: Power for Land, Sea and Air, GT 2006-91119, 11p

[3] Black, P., 2007, "Acoustic Transfer Functions Derived from Finite Element Modeling for Thermoacoustic Stability Predictions of Gas Turbine Engines," Masters thesis, Department of Mechanical Engineering, Virginia Tech, Blacksburg, VA

[4] Broda, J.C., Seo, S., Santoro, R.J., Shirhattikar, G. and Yang, V., 1998, "An experimental study of combustion dynamics of a premixed swirl injector," Twenty-Seventh Symposiun (International) on Combustion/The Combustion Institute, pp 1849-1856

[5] Culick, F.E.C., 1987, "A note on Rayleigh's criterion," Combustion Science and Technology, **56** (4-6), pp 159-166.

[6] Dasch, C.J., 1991, "One-dimensional tomography: a comparison of Abel, onion-peeling, and filtered backprojection methods," Applied Optics, **31**(8), pp 1146-1152

[7] Docquier, N. and Candel, S., 2002, "Combustion control and sensors: a review," Progress in Energy and Combustion Science, **28**, pp 107-150

[8] Dowling, A., 1999, "A kinematic model of a ducted flame," Journal of Fluid Mechanics, **394**, pp 51-72

[9] Ducruix, S., Schuller, T., Durox, D. and Candel, S., 2003, "Combustion Dynamics and Instabilities: Elementary Coupling and Driving Mechanisms," Journal of Propulsion and Power, **19**(5), pp 722-734

[10] Durox, D., Schuller, T., Candel, S. and Ferguson, D., 2005, "Combustion dynamics of inverted conical flames," Proceedings of the Combustion Institute, **30**(2), pp 1718-1724

[11] Fleifil, M., Annaswamy, A.M., Hathout, J.P. and Ghoniem, A.F., 1999, "Reduced-order dynamic models for control of reactive fluid-flows," Proceedings of the IEEE Conference on Decision and Control, **3**, pp 2857-2862

[12] Fleifil, M., Hathout, J.P., Annaswamy, A.M. and Ghoniem, A.F., 2000, "Reduced order modeling of heat release dynamics and active control of time-delay instability," Aerospace Sciences Meeting and Exhibit, 38th, Reno, NV, AIAA-2000-708

[13] Ghoniem, A.F., Park, S., Wachsman, A., Annaswamy, A., Wee, D., Murat A.H. and Candel, S., 2005, "Mechanism of combustion dynamics in a backward-facing step stabilized premixed flame," Proceedings of the Combustion Institute, **30**(2), pp 1783-1790

[14] Ghoniem, A.F., Annaswamy, A., Park, S. and Sobhani, Z., 2005, Stability and emissions control using air injection and H2 addition in premixed combustion," Proceedings of the Combustion Institute, **30**, pp 1765–1773

[15] Gonzalez-Juez, E.D., Lee, J.G. and Santavicca, D.A., 2005, "A Study of Combustion Instabilities Driven by Flame-Vortex Interactions." 41st AIAA/ASME/SAE/ASEE Joint Propulsion Conference & Exhibit, AIAA 2005-4330.

[16] Gutmark, E.J., Schadow, K.C., Nina, M.N.R. and Pita, G.P.A., 1995, "Suppression of combustion instability by geometrical design of the bluff-body stabilizer," Journal of Propulsion and Power, **11**(3), pp 456-463

[17] Haber, L. and Vandsburger, U., 2003, "A Global Reaction Model for OH* Chemiluminscence Applied to a Laminar Flat-Flame Burner," Combustion Science and Technology, **175**, pp 1859-1891

[18] Hendricks, A., 2003, "Determination of Flame Dynamics for Unsteady Combustion Systems using Tunable Diode Laser Absorption Spectroscopy," Masters thesis, Department of Mechanical Engineering, Virginia Tech, Blacksburg, VA.

[19] Hill, P.G., and Peterson, C.R., 1992, *Mechanics and Thermodynamics of Propulsion: Second Edition*, Addison-Wesley Publishing Company, Reading, MA.

[20] Jahnke, C.C. and Culick, F.E.C., 1994, "Application of Dynamical Systems Theory to Nonlinear Combustion Instabilities," Journal of Propulsion and Power, **10**(4), pp 508-517

[21] Janus, M.C., Richards, G.A., Yip, M.J. and Robey, E.H., 1997, "Effects of ambient conditions and fuel composition on combustion stability," ASME Paper, 97-GT-266, 11 p

[22] Khanna, V., Vandsburger, U., Saunders, W.R. and Baumann, W.T., 2002, "Dynamic analysis of swirl stabilized turbulent gaseous flames," American Society of Mechanical Engineers, International Gas Turbine Institute, Turbo Expo (Publication) IGTI, **1**, GT-2002-30061, pp 285-297

[23] Koyama, M., Zimmer, L., Fujiwara, H. and Tachibana, S., 2006, "Effects of swirl combination and mixing tube geometry on combustion instabilities in a premixed combustor," Proceedings of the ASME Turbo Expo: Power for Land, Sea, and Air Conference, **1**, GT2006-90891, pp 663-671

[24] Kulsheimer, C. and Buchner, H., 2002, "Combustion dynamics of turbulent swirling flames," Combustion and Flame, **131**(1-2), pp 70-84.

[25] Lee, J.G., Kim, K. and Santavicca, D.A., 2000, "Measurement of equivalence ratio fluctuation and its effect on heat release during unstable combustion," Symposium (International) on Combustion, **28**(1), pp 415-421

[26] Lee, J.G. and Santavicca, D.A., 2003, "Experimental Diagnostics for the Study of Combustion Instabilities in Lean Premixed Combustors," Journal of Propulsion and Power, **19**(5), pp 735-750

[27] Lieuwen, T., Torres, H., Johnson, C., and Zinn, B.T., 2001, "A Mechanism of Combustion Instability in Lean Premixed Gas Turbine Combustors," Journal of Engineering for Gas Turbines and Power, **123**, pp 182-189

[28] Lieuwen, T., 2003, "Modeling Premixed Combustion-Acoustic Wave Interactions: A Review," Journal of Propulsion and Power, **19**(5), pp 765-781

[29] Lieuwen, T.C. and Yang, V., Editors, 2005, *Combustion Instabilities in Gas Turbine Engines: Operational Experience, Fundamental Mechanisms, and Modeling*, American Institute of Aeronautics and Astronautics, Inc., Reston, VA.

[30] Lieuwen, T., McDonell, V., Petersen, E. and Santavicca, D., 2006, "Fuel Flexibility Influences On Premixed Combustor Blowout, Flashback, Autoignition and Stability," Proceedings of GT2006 ASME Turbo Expo 2006: Power for Land, Sea and Air, GT2006-90770, 15 p

[31] Linck, M.B., Gupta, A.K., Bourhis, G. and Yu, K., 2006, "Combustion Characteristics of Pressurized Swirling Spray Flame and Unsteady Two-Phase Exhaust Jet," Aerospace Sciences Meeting and Exhibit, 44th, Reno, NV, AIAA 2006-377, 15p

[32] Lohrmann, M. and Buchner, H., 2005, "Prediction of stability limits for LP and LPP gas turbine combustors," Combustion Science and Technology, **177**(12), pp 2243-2273

[33] Martin, C., 2006, "Systematic Prediction and Parametric Characterization of Thermoacoustic instabilities in premixed gas turbine combustors," Masters thesis, Department of Mechanical Engineering, Virginia Tech, Blacksburg, VA.

[34] Mongia, R., Dibble, R. and Lovett, J., 1998, "Measurement of air-fuel ratio fluctuations caused by combustor driven oscillations," ASME Paper, 98-GT-304, pp 7.

[35] Mordaunt, C., Brassard, C., Lee, S.-Y. and Santoro, R.J., 2001, "Combustion instability studies in a high-pressure lean-premixed model combustor under liquid fuel operation," Proceedings of the International Joint Power Generation Conference, **1**, pp 249-256

[36] Park, S., Annaswamy, A., and Ghoniem, A., 2001, "Heat Release Dynamics Modeling of Kinetically Controlled Burning," Combustion and Flame, **128**, pp 217-231

[37] Park, S., Annaswamy, A. and Ghoniem, A., 2002, "A model-based self-tuning controller for kinetically controlled combustion instability," Proceedings of the American Control Conference, **2**, pp 1597-1602

[38] Paschereit, C.O., Schuermans, B., Polifke, W. and Mattson, O., 2002, "Measurement of Transfer Matrices and Source Terms of Premixed Flames," Journal of Engineering for Gas Turbines and Power, **124**, pp 239-247

[39] Preetham and Lieuwen, T., 2004, "Nonlinear flame-flow transfer function calculations: Flow disturbance celerity effects," 40th AIAA/ASME/SAE/ASEE Joint Propulsion Conference and Exhibit, AIAA 2004-4035, 17p

[40] Preetham and Lieuwen, T., 2005, "Nonlinear flame-flow transfer function calculations: Flow disturbance celerity effects part 2," 43rd AIAA/ASME/SAE/ASEE Joint Propulsion Conference and Exhibit, AIAA 2005-0543, 19p

[41] Rayleigh, J., 1945, *The Theory of Sound: Second Edition*, Dover Publications, New York.

[42] Sanders, D., O'Brien, W. and Schetz, J., 2006, "An Investigation of Controlled Oscillations in a Plasma Torch for Combustion Enhancement," 14th AIAA/AHI Space Planes and Hypersonic Systems and Technologies Conference, AIAA-2006-7968, 16p.

[43] Schadow, K.C., Gutmark, E., Wilson, K.J. and Smith, R.A., 1990, "Multistep dump combustor design to reduce combustion instabilities," Journal of Propulsion and Power, **6**(4), pp 407-411

[44] Schildmacher, K.-U., Koch, R., and Bauer, H.-J., 2006, "Experimental characterization of premixed flame instabilities of a model gas turbine burner," Flow, Turbulence and Combustion, **76**(2), pp 177-197

[45] Sivasegaram, S. and Whitelaw, J. H., 1987, "Oscillations in confined disk-stabilized flames," Combustion and Flame, **68**(2), pp 121-129

[46] Speth, R.L., Altay, H.M. and Ghoniem, A.F., 2007, "Dynamics and stability limits of syngas combustion in a backward-facing step combustor," Proceedings of GT2007 ASME Turbo Expo 2007: Power for Land, Sea and Air, GT2007-28130, Montreal, Canada

[47] Sutton, G. and Biblarz, O., 2001, *Rocket Propulsion Elements: Seventh Edition*, John Wiley & Sons, Inc., New York.

[48] Tuncer, O., Acharya, S. and Uhm, J., 2007, "Dynamics NOx and flashback characteristics of confined pre-mixed hydrogen enriched methane flames," Proceedings of GT2007 ASME Turbo Expo 2007: Power for Land, Sea and Air, GT2007-28158, Montreal, Canada

[49] Tyndal, J., 1897, *Sound*. D. Appleton & Co., New York.

[50] Weigand, P., Meier, W., Duan, X., and Aigner, M., 2006, "Laser based investigations of thermo-acoustic instabilities in a lean premixed gas turbine model combustor." Proceedings of the ASME Turbo Expo, **1**, pp 237-245

[51] Van Kampen, J.F., Huls, R.A., Kok, J.B.W. and Van Der Meer, T.H., 2003, "One-dimensional acoustic modeling of thermoacoustic instabilities," Proceedings of the Tenth International Congress on Sound and Vibration, pp 735-742

[52] Varatharajan, B., McManus, K., Lacy, B. and Lipinski, J., 2005, "Hydrogen Combustion for Gas-Turbine Combustor Applications – Kinetics and Analysis," 4th Joint Meeting of the US Sections of the Combustion Institute

[53] Venkataraman, K.K., Preston, L.H., Simons, D.W., Lee, B.J., Lee, J.G. and Santavicca, D.A., 1999, "Mechanism of combustion instability in a lean premixed dump combustor," Journal of Propulsion and Power, **15**(6), pp 909-918

[54] You, D., Huang, Y. and Yang, V., 2005, “A generalized model of acoustic response of turbulent premixed flame and its application to gas-turbine combustion instability analysis,” Combustion Science and Technology, **177**, pp 1109-1150